Department of Biocybernetics and Biomedical Engineering
AGH-University of Science and Technology, Kraków Poland

THE DISSERTION IS SUBMITTED FOR DEGREE OF
DOCTOR OF ENGINEERING

Evaluation of new cardiological treatment methods by multimodality imaging

mgr inż. Elżbieta Pociask

Supervisor:
Prof. dr hab. inż. Piotr Augustyniak

Kraków, 2019

Akademia Górniczo-Hutnicza im. Stanisława Staszica w Krakowie

Wydział Elektrotechniki, Automatyki, Informatyki i Inżynierii Biomedycznej

Katedra Biocybernetyki i Inżynierii Biomedycznej

ROZPRAWA DOKTORSKA

Ocena nowych metod leczenia chorób naczyń wieńcowych serca przy wykorzystaniu dostępnych modalności obrazowania

mgr inż. Elżbieta Pociask

Promotor:
Prof. dr hab. inż. Piotr Augustyniak

Kraków, 2019

Pragnę szczególnie podziękować Panu
Profesorowi Piotrowi Augustyniak
za przekazaną mi przez te lata wiedzę, pomoc i naukową opiekę.

Również podziękowania kieruję do
Pana dr Nico Bruining, za współpracę i pomoc udzieloną mi podczas narodzin
tematyki mojej pracy doktorskiej.

Dziękuję Panu dr Tomaszowi Roleder
za udostępnienie obrazów
oraz uzyskanie niezbędnych danych i informacji.

Pracę dedykuję śp. Dziadkowi,
oraz cudownej Rodzinie
w podziękowaniu za miłość,
nieocenione wsparcie i wyrozumiałość.

Contents

Abstract

Cardiovascular diseases are the main threat to life in Poland, and thus are the most frequent cause of mortality. Despite of promotion of healthy lifestyle, we can observe systematic increase in deaths caused by cardiovascular diseases from 45.8% in 2013 to 51.1% in 2050. That is why it is so important to develop tools which will improve and could speed up the diagnostic process, cardiological intervention and finally to choose the correct treatment method. Fast cardiological intervention prevents extensive damage of the myocardium, thus increasing the comfort of a patient's life after a heart attack.

Coronary angiography is used to detect coronary artery stenosis in daily clinical practice. It allows to present the complete coronary artery tree including the tortuosity of the vessel. However, its major limitation is that it visualizes the lumen contour only, which could hide possible problems within an atherosclerotic disease and hence leaves too much room for interpretation in planning and execution of the intervention.

These limitations were a main trigger to develop intravascular imaging methods such as optical coherence tomography (OCT) or near-infrared spectroscopy (NIRS). Along with the new techniques for acquiring medical images, a room for biomedical engineers has been created – a room for developing and improving image processing algorithms, that will enable to computer-assisted quantitative and qualitative assessment of coronary vessels and atherosclerotic plaque.

The main aim of this work was to develop image processing algorithms applied to OCT and NIRS images, enabling cardiologists to detect and interpret atherosclerotic lesions by automatic lumen detection and exploration of lipid pool in the coronary vessels' wall.

Developed algorithms have been validated and the comparative analysis of results has proven that their quality is competitive to commercially available systems. The outcomes were satisfactory enough to estimate that the new methods could be used in core laboratories for research and treatment.

Streszczenie

Choroby układu sercowo-naczyniowego stanowią jedną z głównych przyczyn śmierci w Polsce. Mimo społecznych programów promujących zdrowy styl życia, przewiduje się systematyczny wzrost śmierci wśród populacji polskiej z 45.8% w 2013 roku do 51,1% w 2050. Dlatego bardzo ważny wydaje się nacisk na tworzenie oraz rozwijanie nowych narzędzi umożliwiających przyspieszenie diagnozy, interwencji kardiologicznej, a także dobór odpowiedniej metody leczenia. Szybka interwencja kardiologiczna, zapobiega rozległym uszkodzeniom mięśnia sercowego, zwiększając tym komfort życia pacjenta po zawale.

Koronarografia stosowana jest w codziennej praktyce klinicznej w celu detekcji niedrożności naczyń wieńcowych serca. Poprzez podanie kontrastu umożliwia zwizualizowanie w pełni konturów naczynia jednak bez wglądu do wnętrza naczynia, co często bywa kluczowe przy ocenie zaawansowania choroby miażdżycowej. Te ograniczenia przyczyniły się w ostatnich latach do rozwoju wewnątrznaczyniowych technik obrazowania takich jak optyczna tomografia komputerowa (OCT), czy spektroskopia bliskiej podczerwieni (NIRS). Wraz z nowymi technikami pozyskiwania obrazów medycznych, powstała przestrzeń dla inżynierów biomedycznych – przestrzeń na rozwijanie oraz ulepszanie algorytmów przetwarzania obrazów, które pozwolą na wspomaganie komputerowe ilościowej i jakościowej oceny naczyń wieńcowych serca i blaszki miażdżycowej.

Celem niniejszej pracy było utworzenie algorytmów do przetwarzania obrazów OCT i NIRS, umożliwiających kardiologom wykrywanie i interpretację zmian miażdżycowych poprzez automatyczną detekcję światła naczynia oraz wykrywanie złóż lipidowych w ścianach naczyń wieńcowych.

Opracowane algorytmy zostały przetestowane, a otrzymane rezultaty - porównane z wynikami otrzymanymi z komercyjnych systemów. Uzyskane rezultaty okazały się zadowalające, a zaproponowane algorytmy mogą być wykorzystywane w laboratoriach przetwarzania obrazów w celach naukowych, badawczych i rozwojowych.

Abbreviations and acronyms

2D	Two-dimensional
3D	Three-dimensional
ACS	Acute coronary syndrome
AMI	Acute myocardial infraction
BMS	Bare metal stent
BVS	Bioresorbable vascular scaffold
CABG	Coronary artery bypass graft
CAD	Coronary artery disease
CSA	Cross-sectional area
CVD	Cardiovascular disease
DES	Drug-eluting stent
ECG	Electrocardiography
FEM	Fixational Eye Movements
FD	Fourier-Domain
FIT	Fibrous intimal thickening
Fr	French catheter scale
ICC	Intra-class correlation coefficient
IVUS	Intravascular ultrasound
IV-OCT	Intravascular optical coherence tomography
LA	Lumen area
LAD	Left anterior descending coronary artery

LCBI	Lipid core burden index
LCP	Lipid core plaque
LCX	Left circumflex coronary artery
LD	Lumen diameter
LM	Left main
M	Month
MACE	Major adverse cardiac events
MI	Myocardial infraction
MLA	Minimal lumen area
MLD	Minimal lumen diameter
NIRS	Near-infrared spectroscopy
NSTEMI	Non-ST-segment elevation myocardial infraction
OCT	Optical coherence tomography
OFDI	Optical frequency domain imaging
PB	Plaque burden
PCI	Percutaneous coronary intervention
PLLA	Poly-L-Lactid Acid
QCA	Quantitative coronary angiography
RCA	Right coronary artery
ROC	Receiver-operator characteristic
ROI	Region of Interest
SA	Scaffold area

SD Scaffold diameter

STEMI ST-segment elevation myocardial infraction

TCFA Thin-cap fibro-atheroma

TD Time-Domain

CHAPTER 1

1. Introduction

The importance of the heart is obvious. The heart is the life-giving, ever-beating muscle in the human chest. It is the center of the cardiovascular system and works beat by beat, second by second for 24 hours a day and never resting, except for a fraction of a second between beats.

It was assessed that human heart would contract approximately 3 billion times during a 75-year lifespan. Each of the major pumping chambers of the heart ejects approximately 70 mL of blood per contraction in a resting adult. This would be equal to 5.25 liters of fluid per minute and approximately 14 000 liters per day. Over one year, that would equal 10 000 000 liters of blood sent through 60 000 miles of vessels – it is enough to go around the world more than twice [2, 3]. Knowing that it is the one of the most vital organs keeping us alive it is important to treat it like our greatest treasure.

However, our life styles, eating habits, lack of activity can dramatically affect the overall health of our heart.

1.1. Motivation

Cardiovascular diseases are the main threat to life in Poland, and thus are the most frequent cause of mortality. According to statistic (GUS) [4] cardiovascular diseases more often affect women, also mortality due to these diseases is definitely higher than men.

Among of the cardiovascular diseases (CVD), the cause of the largest number of deaths is Coronary Artery Disease (CAD), which was responsible for 23% of cardiac deaths (41 thousand deads), including myocardial infraction, 9% of deaths (15 thousand dead) in 2013 year [4].

The second, most important group of causes of death in cardiovascular disease is cerebrovascular disease, which concerned 18% of cardiac deaths, it was almost 33 thousand deads in 2013 in Poland.

The mortality varies with age. In 2013, almost 83% of all deaths as a result of CVD concerned people aged over 65 years. The atherosclerosis and heart failure were the main causes of cardiac deaths, 23% and 22%, respectively.

Premature deaths - death under the age of 65 due to cardiovascular disease, in the last years are more or less at the same level. In 2013, for every 100,000 deaths, nearly 92 were caused by diseases of the cardiovascular system.

When we look closer to causes of cardiac events contributing in mortality under the age of 65, we notice that CAD is a cause of 30% of all cardiac deaths.

According to the GUS report [4], the number of deaths in Poland is expected to increase to around the year 2043, after which there will be slight decrease and in 2050 and it will amount to 428.3 thousand, which means an increase by almost 41 thousand deaths compared to 2013. Estimated forecasts are collected in Table 1-1 We can observe systematic increase in deaths caused by cardiovascular diseases from 45.8% in 2013 to 51.1% in 2050.

Table 1-1 Estimation of the number of deaths due to CVD based on the prognosis

Year	2013	2015	2020	2025	2030	2035	2040	2045	2050
[thousands]									
Deaths - generally	387.0	368.8	394.7	397.7	406.2	425.7	440.0	440.9	428.3
Deaths caused by cardiovascular diseases:	177.4	180.1	188.5	194.1	201.1	212.0	220.8	223.3	218.9
0-64 age	30.2	27.1	22.7	18.4	15.6	15.1	13.8	11.7	9.1
> 65 age	147.2	153.0	165.8	175.7	185.4	196.8	206.9	211.6	209.9
[%]									
Deaths caused by cardiovascular diseases:	45.8	48.8	47.8	48.8	49.5	49.8	50.2	50.6	51.1
0-64 age	17.0	15.0	12.0	9.5	7.8	7.2	6.3	5.2	4.1
> 65 age	83.0	85.0	88.0	90.5	92.2	92.8	93.7	94.8	98.9

The analysis above shows that cardiovascular diseases remain the main cause of mortality. That is why it is so important to develop tools which will improve and could speed up the diagnostic process and then cardiological intervention and treatment. We have to keep in mind that the faster the cardiological intervention, the more comfortable the patients' life after myocardial infraction.

1.2. Thesis and main goal

A review of the current state of the knowledge in the field of the processing and recognition of coronary vessels images and available tools to diagnosis of atherosclerotic plaque, allows to set the basic scope of thesis:

Using the developed image processing algorithms, enables to computer-assisted quantitative and qualitative evaluation of arteries' lumen and lipid plaque by different Intracoronary Imaging Methods, aiding experts in detection and interpretation of atherosclerosis patterns and cardiac diagnostics.

Wykorzystanie opracowanych algorytmów przetwarzania obrazu, umożliwia wspomaganie komputerowe ilościowej i jakościowej oceny światła i blaszki lipidowej tętnic za pomocą różnych metod obrazowania wewnątrznaczyniowego, ułatwiając ekspertom wykrywanie i interpretację wzorów miażdżycy, a tym samym diagnostykę kardiologiczną.

Using simple image processing methods, it is possible to detect the lumen of coronary arteries, detect and analyze the lipid plaque in the coronary vessel walls, that facilitate cardiac diagnosis. The thesis assumes that the use of appropriate algorithms for multimodality imaging processing will enable the detection and analysis of individual pathological structures. The results of the analysis of the percent artery stenosis and the quantitative analysis of the lipid pool will allow experts to make a preliminary diagnosis of whether the observed change is a vulnerable plaque with a high risk of rupture or a soft plaque, which determine the way of treatment (medicines or stent implantation). The main purpose of the conducted research, was to proof the truth of the thesis. Specifically:

1. To familirize with diagnostic methods used in interventional cardiology and determining the scientific problem, which is the scope of this thesis.
2. To analyze the state of knowledge in the field of processing and analyzing cardiac images.
3. To get an access to database of intracoronary images containing both modalities OCT and NIRS images.

4. To use perception parameters to improve algorithms to finding pathological changes in OCT images.
5. To develop themethodology for the pre-processing of OCT images.
6. To segment a lumen area from OCT cross-sectional images:
    a. To analyze of the research problem and existing segmentation methods.
    b. To perform automatic detection and contour drawing of lumen area.
7. To develop the methodology for the pre-processing NIRS images.
8. To develop the methodology for detection of artifacts.
9. To segment a lipid core plaque from NIRS images.
10. To develop diagnosis-specific methods of automatic inference of possible medical outcome.

1.3. The structure of the thesis

This thesis is organized in 5 chapters. Chapter 1 presents the motivation of work and the scope of the thesis. Chapter 2 defines the researh area. It describes the heart anatomy and physiology of the vascular systems. It evaluates coronary disfunctions – coronary artery disease. It provides an overview of the various invasive imaging techniques that can be employed for the evaluation of coronary atherosclerosis. It also introduces basic medical image processing methods which are applied in further part of the thesis. It includes the review of the state of the art in the area of algorithms of OCT and NIRS image processing with focusing on showing the room for advances in biomedical engineering. Achieving the main scope of the doctoral thesis required the realization of particular aims. To keep the thesis readable each modality is described in a separate chapter. Chapter 3 is devoted to OCT image processing, algorithms, conducted statistical analysis and presentation of results. Chapter 4 is focused on another intracoronary imaging modality, the NIRS. It provides details on every step of algorithm to fully automated lipid pool detection, presents validation of developed algorithms and the results. The last chapter is a summary, which contains a description of the original elements of the doctoral thesis, proving the thesis and presents development prospects together with the possibilities of further research.

CHAPTER 2

2. Analysis of the research problem

2.1. Heart anatomy

The human heart is located in the thoracic cavity, medially between the lungs in the mediastinum. It is about the size of a fist and its weight is about 250-300 g.The shape of the heart is similar to pyramids. It has a base, connected to the large vessels of the systemic circuit and pulmonary circuit, directed upwards, backwards and to the right, and the tip of the heart, the apex facing downwards and to the left [2, 3] [5].

The human heart consists of four chambers. The left side and the right side each have one atrium and one ventricle. Each of the atria: the right atrium and the left atrium, acts as a receiving chamber and contracts to push blood into the lower chambers, the right ventricle and the left ventricle. The ventricles serve as the primary pumping chambers of the heart, propelling blood to the lungs or to the rest of the body (*Figure 2-1*) [2] [3] [5].

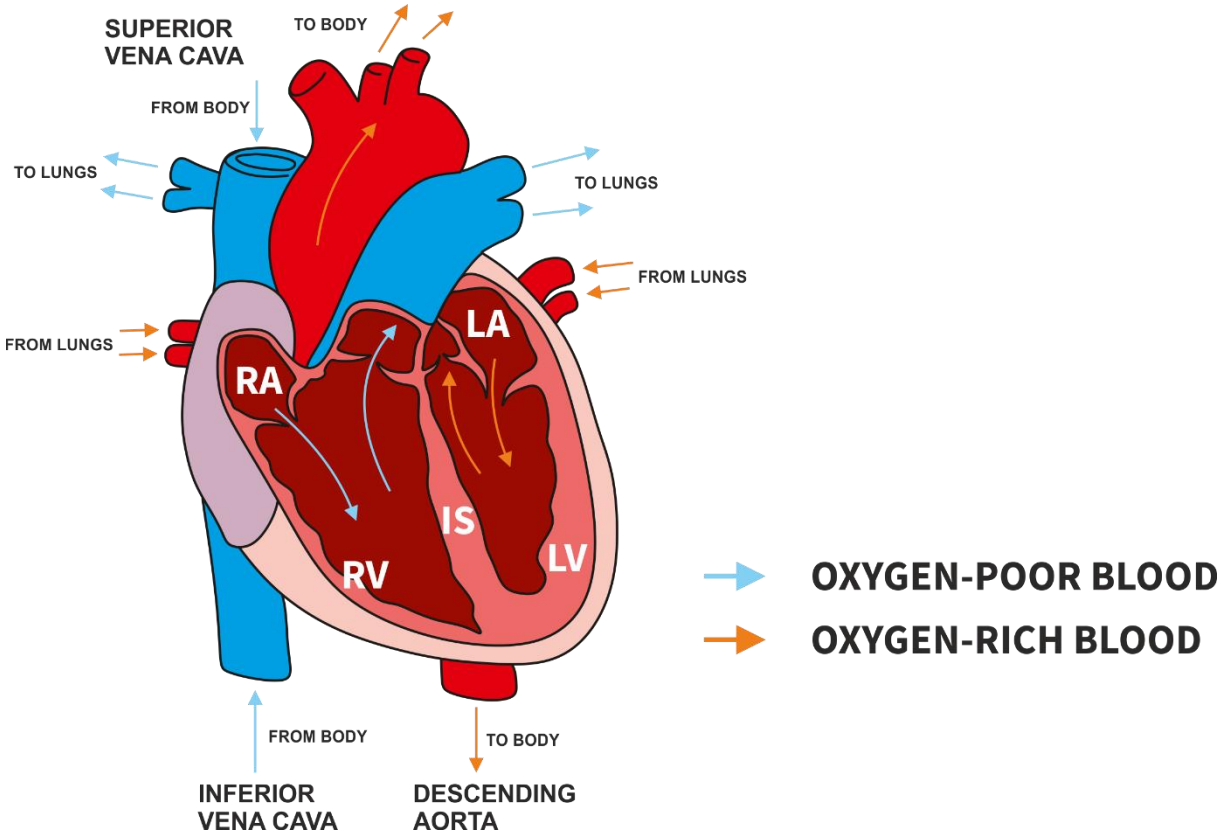

Figure 2-1 The heart is consist of four chambers: the right and left ventricles (RV and LV) and right and left atria (RA and LA). The ventricles are separated by the interventricular septum (IS).

Physiology of the vascular system

There are two distinct but linked circuits in the human circulation called the pulmonary and systemic circuits. The pulmonary circuit transports blood to and from the lungs, where it picks up oxygen and delivers carbon dioxide for exhalation. The systemic circuit transports oxygenated blood to virtually all of the tissues of the body and returns relatively deoxygenated blood and carbon dioxide to the heart to be sent back to the pulmonary circulation. Blood flows from the right atrium to the right ventricle, where it is pumped into the pulmonary circuit. The blood in the pulmonary artery branches is low in oxygen but relatively high in carbon dioxide. Gas exchange occurs in the pulmonary capillaries and blood high in oxygen and low in carbon dioxide is returned to the left atrium. Next the blood enters the left ventricle, which pumps it into the systemic circuit. In the systemic capillaries, the oxygen and nutrients go out of the capillaries. The deoxygenated blood returns to the right atrium and the cycle is repeated. [2, 3] [5] [6].

Coronary heart vessels

Coronary arteries supply blood to the myocardium and other components of the heart. There are three dilations in the wall of the aorta. Two of these, the left posterior aortic sinus and anterior aortic sinus, give rise to the left and right coronary arteries, respectively. The third sinus, the right posterior aortic sinus, typically does not give rise to a vessel.

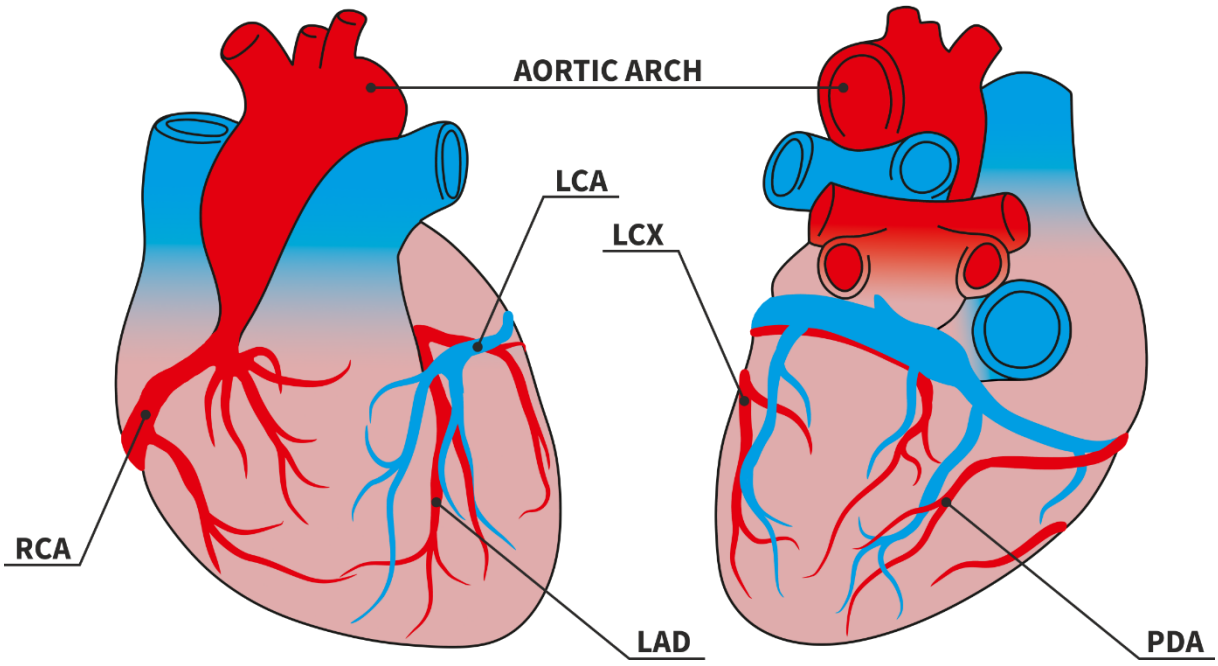

Figure 2-2 Coronary arteries and cardiac veins. Left, Anterior view. Right, Posterior view.

The left coronary artery distributes blood to the left side of the heart, the left atrium and ventricle, and the interventricular septum. The circumflex artery arises from the left coronary artery and follows the coronary sulcus to the left.. The larger anterior interventricular artery, also known as the left anterior descending artery (LAD), is the second major branch arising from the left coronary artery. It follows the anterior interventricular sulcus around the pulmonary trunk. Along the way it gives rise to numerous smaller branches that interconnect with the branches of the posterior interventricular artery, forming anastomoses. An anastomosis is an area where vessels unite to form interconnections that normally allow blood to circulate to a region even if there may be partial blockage in another branch. The anastomoses in the heart are very small. Therefore, this ability is somewhat restricted in the heart so a coronary artery blockage often results in death of the cells supplied by the particular vessel.

The right coronary artery proceeds along the coronary sulcus and distributes blood to the right atrium, portions of both ventricles, and the heart conduction system. Normally, one or more marginal arteries arise from the right coronary artery inferior to the right atrium. The marginal arteries supply blood to the superficial portions of the right ventricle. On the posterior surface of the heart, the right coronary artery gives rise to the posterior interventricular artery, also known as the posterior descending artery. It runs along the posterior portion of the interventricular sulcus toward the apex of the heart, giving rise to branches that supply the interventricular septum and portions of both Figure 2-2 [2] [3] [5].

2.2. Coronary Artery Diseases

Coronary Artery Diseases (CAD) include myocardial ischemia associated with coronary artery lesions. The most common (> 98% of cases) cause of CAD is coronary atherosclerosis.

Coronary atherosclerosis is a chronic inflammatory disease of the arteries, characterized by the formation of characteristic changes - plaques in the vessel wall - consisting of lipids, cholesterol and fatty acids, white blood cells, primarily macrophages, calcifications and fibrosis [5] [7]. This process, over time, may give different symptoms depending on plaque composition (Figure 2-3). A gradual narrowing of the vessel by growth of a fibrous or calcific plaque will cause chest pain upon exertion, due to cardiac ischemia. It is a condition called stable CAD. Sudden onset of chest pain, or chest pain at rest, is a symptom of unstable CAD or acute coronary syndromes (ACS), which is associated with thrombus formation on plaques, mostly due to rupture of a lipid-core lesion [8] [9] [10] [11] [12]. The most severe form of this disease may lead to a myocardial infraction (MI) of heart attack [13].

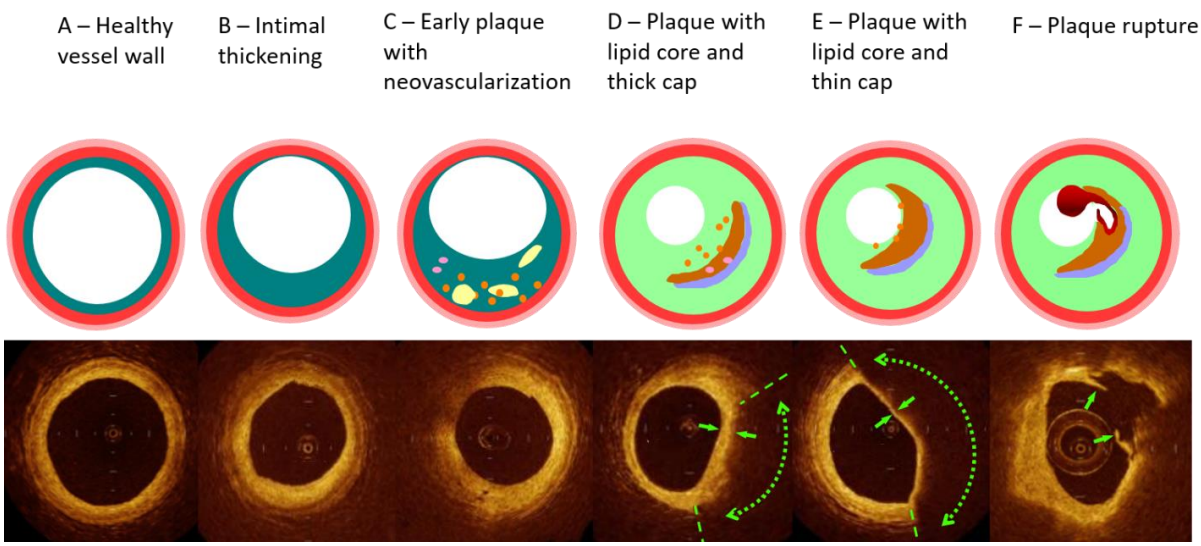

Figure 2-3 Plaque distinction according to AHA classification. In the top we have scheme of plaque progression, in the bottom there are referring cross-sectional views from intravascular imaging – optical coherence tomography. The green arrows in panel D and E sho cap thickness. In the panel F green arrows show interrupted cap – resulting plaque rupture.

Myocardial infarction is a result of a lack of blood flow (ischemia) and of oxygen (hypoxia) to a region of the heart, ensue death of the cardiac muscle cells. An MI often occurs when a coronary artery is blocked by accumulation of atherosclerotic plaque or it can also occur when a portion of an unstable atherosclerotic plaque travels through the coronary arterial system and stucks in one of the smaller vessels. The resulting blockage restricts the flow of blood and oxygen to the myocardium and causes death of the tissue.

The distribution of atherosclerotic lesions in the arteries is very heterogeneous. The lesions appear the fastest or are more complex in the proximal artery segments, in the bifurcation and in the artery arch. Laminar blood flow protects against atherosclerosis. The turbulent flow of blood in the vessel, typical for atherosclerotic plaques occurrence, leads to an increase in shear stress, which activates specific mechanisms to promote the development of atherosclerotic lesions and weakening of physiological protective mechanisms.

A mature atherosclerotic plaque is made up of a cap from the lumen side of the vessel, usually containing relatively lot of collagen and smooth muscle cells, and a lipid core of various sizes (Figure 2-4).

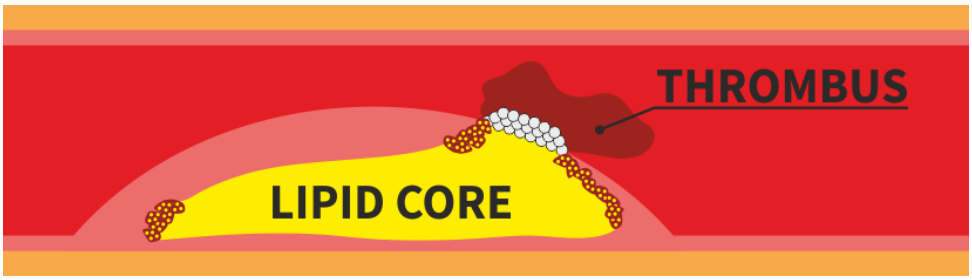

Figure 2-4 Atherosclerotic plaque

As the plaque grows we can observe the remodeling of vessel wall. There are two kind of remodeling: positive remodeling when the growing plaque "pushes" the arterial wall outward, then its outer diameter increases and the inside diameter of the vessel remains unchanged; negative remodeling when the inflammatory process occurs within the plaque causing stenosis of the artery lumen. The narrowing of the artery lumen usually occurs when the size of the plaque in the wall exceeds 40% of the cross section of the vessel.

2.3. Coronary Imaging in the diagnosis of Coronary Disease

The various nature of progression of coronary artery disease indicates the direction of development of new coronary imaging techniques. Usually the coronary disease has a long asymptomatic latent period, could be focal or diffuse. The expectations of clinicians from image interpretation experts are enormous but quite well defined. Clinicians need assistance in the identification of patients who are at very high risk of developing acute coronary events [14]. In previously asymptomatic individuals, sudden coronary death or acute myocardial infraction occurs as the first manifestation of coronary atherosclerosis.

Therefore, the challenge is how to detect and treat the same lesions before adverse events (like plaque rupture and thrombosis) and a need for accurate prediction defines a role of imaging in asymptomatic individuals at high risk.

Percutaneous coronary intervention (PCI) is the most common method of revascularization either in stable CAD or ACS. This minimally invasive treatment is a cheap and fast remedy for CAD [15] [16].

Therapy of PCI is to puncture the peripheral artery, usually the femoral artery, less frequently the radial artery and insert the catheter into the narrowed artery. Next, the narrowed or occluded artery is reopen by using a balloon, which is followed by the implanted metal or bioresorbable stent, to support the vessel wall (Figure 2-5). Stents are specially manufactured expandable stainless steel tubes or bioresorbable scaffolds, mounted on a balloon catheter. When the stent

device is positioned within stenosis, the balloon is inflated which, in turn, expands the stent and the artery. The balloon is removed and the stent remains in place, supporting the inner artery walls in the more open, dilated position.

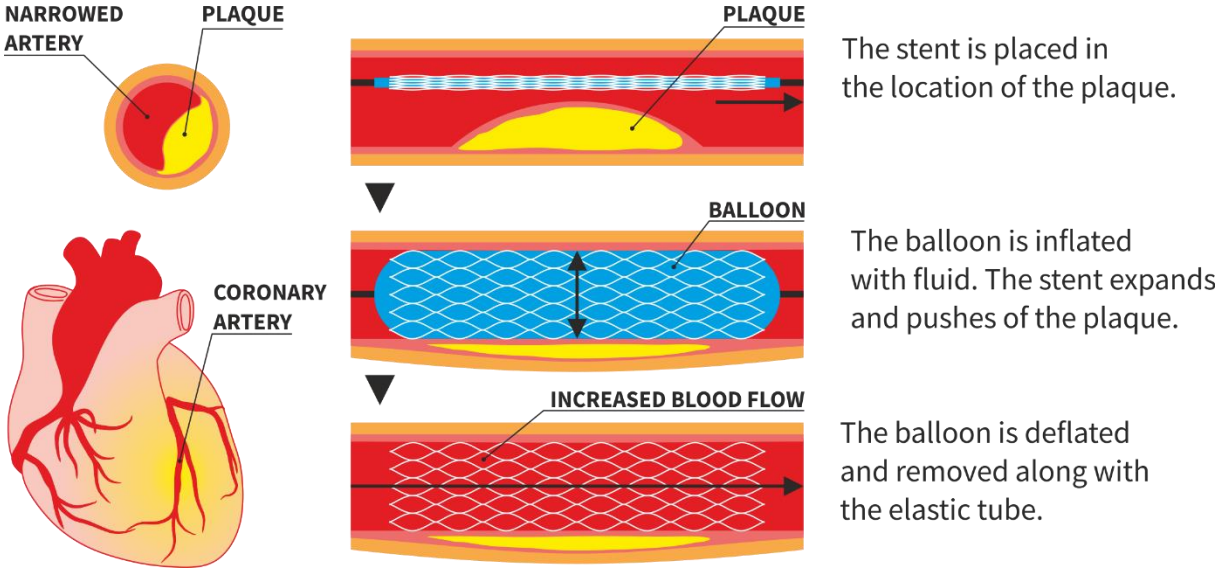

Figure 2-5 Angioplasty with stent implantation procedure

The guidance of PCI depends on imaging technologies and all procedures (balloon and stent implantation) use X-ray angiography to size and position the balloon and the stent. The diagram of stent implantation under the guidance of angiography is showed Figure 2-6.

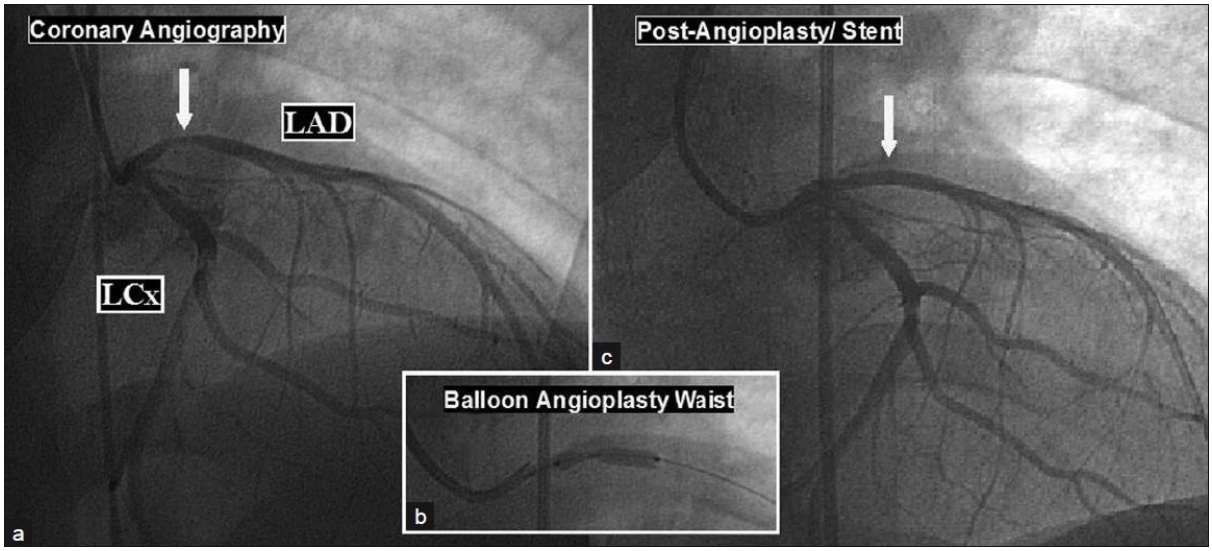

Figure 2-6 Figure shows coronary angiograms: (a) Coronary angiogram with a 70% proximal left anterior descending artery (LAD) lesion and LCX: left circumflex artery; (b) Angioplasty shows the waist; (c) LAD after stent implantation[17].

The sections below describe the possibilities offered by new modalities of coronary imaging in an effort to optimize risk stratification for coronary artery disease.

2.3.1. Drawbacks of angiography

Coronary angiography is still the gold standard in daily clinical practice, however it does not provide all information needed to fully assess the condition of the diseased artery. Coronary angiography presents the complete coronary artery tree including the tortuosity of the vessel, however, its major limitations are possible foreshortening [18] of coronary lesions and the fact that it visualizes the lumen contour only, which could hide possible problems within diffuse lesions[19] and hence leaves too much room for interpretation in planning and execution of the intervention. What are the consequences? - Inaccurate stent sizing, positioning, or expansion resulting stent malpposition, dissections, over- and under- expansion may lead to delayed healing, restenosis or acute stent failure [20] [21] [22] [23].

Coronary angiography is not a sufficient method to provide in-depth knowledge of coronary artery disease and to show in detail plaque progression or regression unlike the cross-sectional based intracoronary imaging modalities as Intravascular Ultrasound (IVUS) [24] [25] or Optical Coherence Tomography (OCT) [26] [27] [28]. Thus intracoronary imaging methods are crucial additional imaging tools making them complementary methods to angiography [29].

2.3.2. Intravascular optical coherence tomography (IVOCT)

Optical Coherence Tomography is an imaging modality based on characteristic of the the near-infrared (nIR) light, with central wavelength of the light ranges from 1250 to 1350 nm. The cross-sectional images are generated by measuring an interference signal, backscattered from the analyzed tissue with the light backscattered from the reference mirror (Figure 2-7).

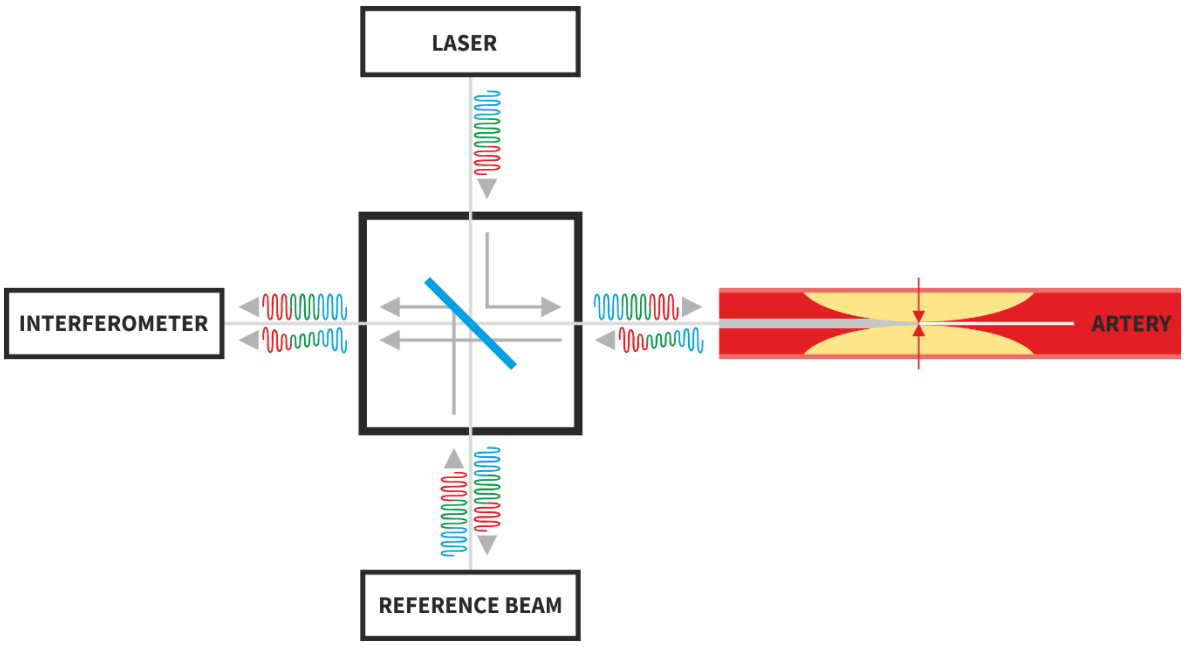

Figure 2-7 The principle of Optical Coherence Tomography.

When collecting images, the OCT probe is continuously pulled back from the coronary artery, and thus performs a scan of the segment of interest. The frequency of the interference signal corresponds to the depth of the analyzed tissue. The main obstacle to the adoption of OCT imaging in clinical practice is that the OCT cannot operate through a blood field, as it requires clearing or flushing blood from the lumen.

There are two approaches to analyze the interference signal of nIR: a time-domain (TD) and a frequency-domain (FD). TD analysis measures an alteration of the interference signal derived by one wavelength of nIR light at a time. Conversely, FD analysis using Fourier transformation measures the interference signal of whole spectrum of nIR light at a single time point. Introduction of FD analysis was a key milestone toward clinical viability of the intravascular OCT as it significantly decreased the time of OCT imaging and eliminated the need to temporarily occlude the investigated segment in order to clear it from the blood. Therefore, current systems of the intravascular OCT imaging employ only FD analysis. The use of light enables the OCT to provide high-resolution images (10-20 μm) of the vessel wall as compared to images obtained by IVUS (100 μm). The nIR light has limited penetration into the vessel wall and obtains signal only from 1 to 3mm in depth. Such a low penetration of the light beam hampers a full assessment of the plaque.

The OCT probe is composed of a signal generator (light source) -"swept laser", a detector and a reference fixed mirror. The nIR light travels from the light source to the probe via an optical fiber, and the probe directs the light outwards and perpendicular to the catheter. The probe rotates with the frequency of 100 frames/s, which allows an acquisition of 50.000 axial lines of the signal per second.

A single pullback is performed with the speed of 20 mm/s and lasts 2.7 seconds. It allows imaging up to 72 mm of the vessel during the single run of the probe. Such a fast pullback of the OCT probe significantly reduces a bias caused by the cardiac movement. Images are displayed in 2 ways: longitudinal view (L-Mode) and "B-Mode" cross-sectional view (Figure 2-8).

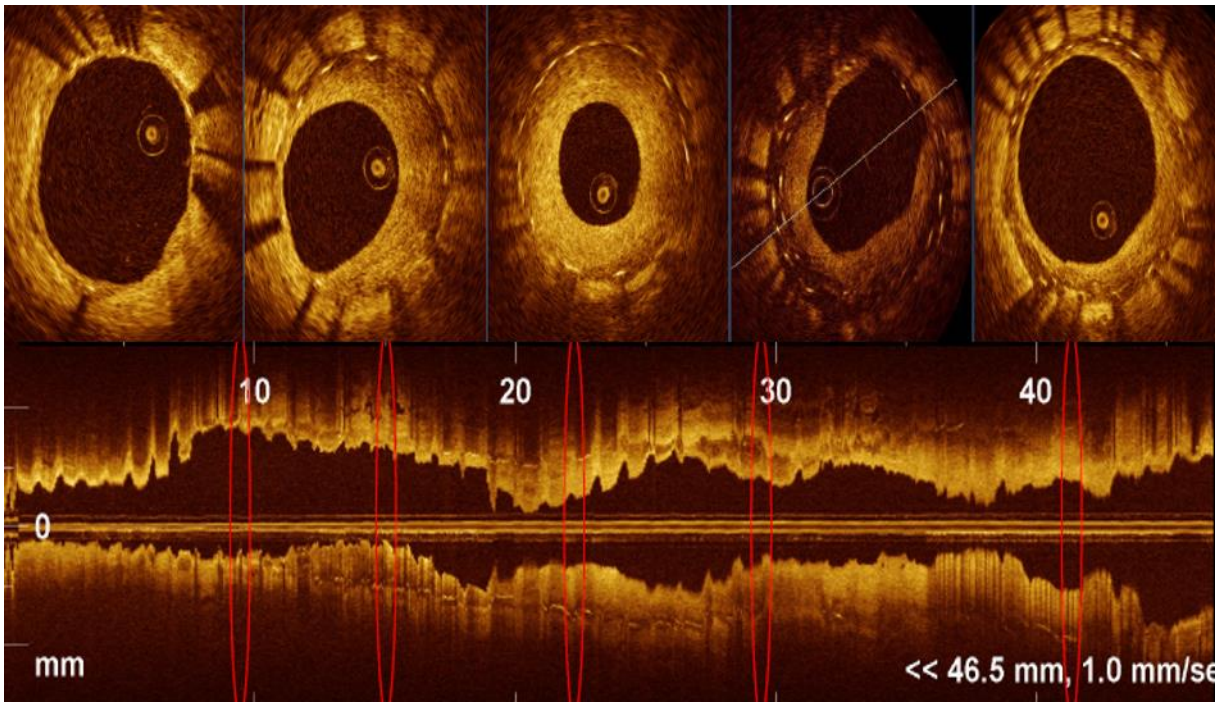

Figure 2-8 OCT images artery lumen with metal stent implanted. In the top there is longitudinal view and below it there are cross-sectional views of OCT.

Intravascular OCT in daily clinical practice is used as a diagnostic tool to assess and detect Stable Coronary Artery Disease and Acute Coronary Syndromes. However the most important current application of OCT is guidance of stenting procedures to plan the whole procedure, started from lesion preparation, through stent selection, stent optimization, taking into account edge dissections, stent malapposition and stent expansion.

2.3.3. Near Infrared Spectroscopy (NIRS)

Near Infrared Spectroscopy (NIRS) is a method within the field of analytical chemistry for the identification of unknown organic molecules or mixed samples. The transmission and absorption of nIR light by the organic molecules in the artery wall and plaque produces a unique chemical signature. A NIRS-IVUS imaging system is a system with integrated near infrared spectroscopy lipid core plaque detection and enhanced IVUS imaging technologies. The catheter provides simultaneous, co-registered acquisition of NIRS lipid core plaque (LCP) detection and grayscale IVUS. By obtaining view of plaque composition both in terms of its

via a monorail imaging catheter system similar in design and profile to a standard mechanical IVUS catheter. The catheter can be inserted via a 6 Fr (French scale is used to measure the size of catheter – is three times the diameter in mm) guide and over a 0.014” guidewire. The IVUS data are acquired via rotating transducer operating at 40 MHz. Scanning with automated rotational pullback is performed at a speed of 0.5 mm/s. The system performs approximately

32,000 chemical measurements per 100 mm of artery scanned through the blood. Each measurement interrogates 1-2 mm of tissue at a depth of about 1 mm. After near-infrared light emission, the detector measures the amount of near-infrared light reflected at different wavelengths to determine the tissue composition.

A predictive algorithm calculates the probability that a LCP is present at each interrogated location in the artery and after pullback, NIRS lipid core data are immediately and automatically displayed in a two-dimensional map of the vessel (Figure 2-9).

Figure 2-9 Panel A shows exemplary chemogram and panel B shows corresponding block chemogram. Panel C shows cross-sectional IVUS image with corresponding NIRS data.

The x-axis of the chemogram represents mm of pullback in the artery and the y-axis represents degrees of rotation: a colour scale from red to yellow indicates increasing. The 'block chemogram' (Figure 2-9) provides a semi-quantitative summary metric of the results for each 2 mm section of artery. The numerical value of each block in the block chemogram represents the 90th percentile of all pixel values in the corresponding 2 mm chemogram segment. The block chemogram is mapped to the same colour scale as the chemogram, and the display is grouped into four discrete colours to aid in visual interpretation. The colors are assigned to the probability that the LCP is present in a given 2 mm block in the following way: red: $p<0.57$; orange: $0.57\leq p\leq 0.84$; tan: $0.84\leq p\leq 0.98$; yellow: $p>0.98$ [30]. Additionally, the NIRS data are mapped and paired with corresponding IVUS frames, as a ring around IVUS image (Figure 2-9).

2.4. Image processing

2.4.1. Introduction to Image Processing

Image processing is a series of mathematical operations on an image, in order to get an enhanced image or to extract some needed information from it. It is a type of signal processing where input is an image and output could be an image or features associated with that image [31] [32].

Image processing basically includes:

- Importing the image via image acquisition tools.
- Image representation and modeling.
- Image enhancement.
- Image restoration.
- Image reconstruction.
- Image compression.

Image processing also includes image analysis. Among the issues of image analysis we can listed:

- Image pre-processing (filtration, histogram analyses, thresholding).
- Extraction of features.
- Segmentation.
- Automated analysis of image (features analyses).
- Generation of an altered image or report that is based on image analysis.

Image analysis is itself an extensive field of science and technology. It covers many specialized areas, such as biomedical image analysis.

2.4.2. Image definition

In the continuous case, a natural image is represented by a two-dimensional function *(x, y)→f(x, y)*. The value of *f* at the spatial coordinates *(x, y)* is positive and it is determined by the source of the image. If the image is generated from a physical process, its intensity values are proportional to energy radiated by a physical source.

In case of X-ray, the images are formed via transmission of the illumination through a medium and it is presented:

$$L_{min} \leq l = f(x, y) \leq L_{max} \qquad (2\text{-}1)$$

where $l = f(x, y)$ is the gray-level at coordinates (x, y).

It is common to shift the gray-scale (or intensity scale) from the interval $[Lmin, Lmax]$ to the interval $[0, L - 1]$. Then $l = 0$ is considered black and $l = L - 1$ is considered white on the gray scale. The intermediate values are shades varying from black to white.

When x, y and the intensity values of f are finite, discrete quantities, such image is called a digital image. A digital image is composed of a finite number of elements, called pixels, each of which has a particular location and value [31] [33] [34].

In order to become suitable for digital processing, an image function $f[x, y]$ must be digitized (Figure 2-10). Digitization is the conversion of a continuous-tone and spatially continuous brightness distribution $f[x, y]$ to an discrete array of integers $f_q[n, m]$ by two operations (Figure 2-11):

- **sampling** — a function of continuous coordinates $f[x, y]$ is evaluated on a discrete matrix of samples indexed by $[n, m]$.
- **quantization** — the continuously varying brightness f at each sample is converted to a one of set of integers f_q by some nonlinear thresholding process. The digital image is a matrix of picture elements, or pixels.. Each matrix element is an integer which encodes the multivalue at ech pixel.The integer value is called the gray value or digital count of the pixel.

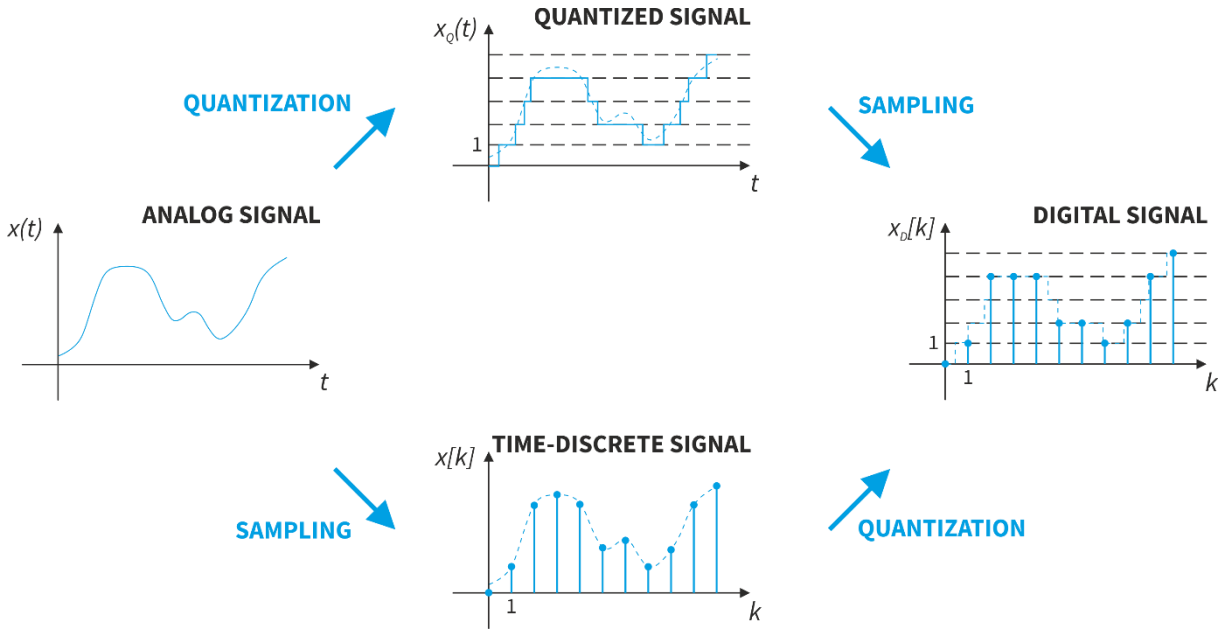

Figure 2-10 Example of sampling and quantization of signal.

The sampling rate determines the spatial resolution of the digitized image, while the quantization level determines the number of grey levels in the digitized image.

The number of quantization levels should be high enough for human perception of fine shading details in the image. The occurrence of false contours is the main problem in image which has been quantized with insufficient brightness levels.

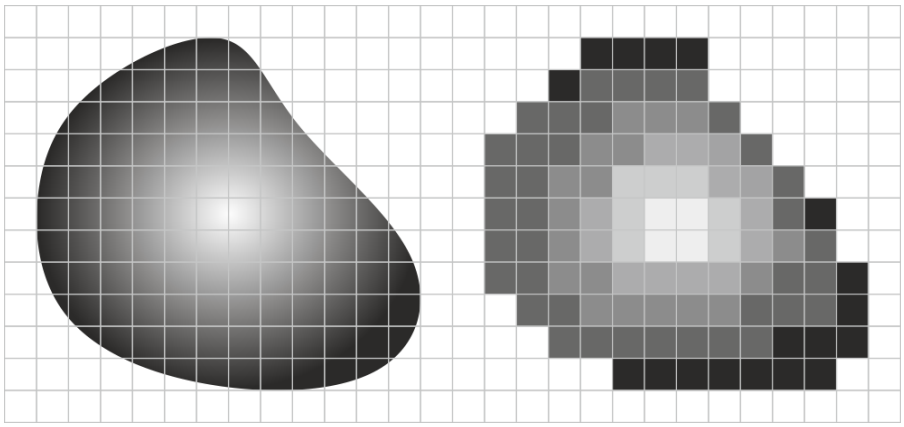

Figure 2-11 Continous image (left side) projected onto a sensor array. Right side - result of sampling and quantization.

After converting image information into an array of integers, the image can be manipulated, processed, and displayed by computer.

Digital images can have different representations (Figure 2-12):

- **Monochromatic image** (or gray – level image) – sample values correspond to the gray levels (or intensities) of individual image points. It is the most common type of medical images. Internal organs are presented on a grayscale image.

  $$f: P \rightarrow \{0,1,\ldots\ldots,L-1\} \qquad (2\text{-}2)$$

  Where,

  L is number of quantization levels

- **Binary image** (or bi-level images) - the samples may have one of only two values: 0 or 1. The use of a binary image simplifies the processing of images, recognizing and analyzing objects.

  $$f: P \rightarrow \{0,1\} \qquad (2\text{-}3)$$

- **RGB image** – The value of each pixel is represented by three numbers, which are components of individual basic colors (red, green and blue). The desired color is obtained by combining the base colors in the appropriate proportions.

  $$f: P \rightarrow [0, L_1) \times [0, L_2) \times [0, L_3) \qquad (2\text{-}4)$$

  Where,

P is a finite set of pixels

$[0, L_i) = \{0, 1, 2, \ldots, L_i - 1\}$ - is a representation of quantization and $L_1 + L_2 + L_3 = 256$

Figure 2-12 OCT cross-sectional view in RGB, in Gray-scale and as a binary image.

2.4.3. Point operations

Point operations are a set of very simple and useful transformations of images [35] [36] [37]. The characteristic for these operations is that the value of the output image $g\ (x, y)$ depends only on the value of the same pixel in input image $f(x, y)$. Thus, point operations do not carry any new information about the image, only make that further computer image analysis could be easier and more efficient.

Examples of these operations include:

- Contrast stretching.
- Segmentation.
- Histogram equalization.
- Binarization.

Image histogram

Image histograms are used very often in image processing. The histogram of the image $f[x, y]$ plots the population of pixels with each gray level f from range [0, 255]. Because all pixels in the image are attributed with the gray value, the sum of populations of the histogram must equal the total number of image pixels N for an 8-bit images:

$$\sum_{f=0}^{f=255} H(f) = N \qquad (2\text{-}5)$$

The histogram is the probability distribution function of gray-levels in the image. The discrete probability distribution function $p\ [f]$ must be equal:

$$\sum_{f=0}^{f=255} p(f) = 1 \qquad (2\text{-}6)$$

Therefore the probability distribution and histogram are related by the expression:

$$p|f| = \frac{1}{N} * H|f| \qquad (2\text{-}7)$$

The histogram often contains valuable global information about the image. The shape of the histogram allows to assess the quality of the monochrome image contrast. An image with high - contrast (we can easily see the image details in fragments of all gray level), has a histogram of values in the entire range [0, 255]. Low-contrast image contains pixel in a few gray levels over a narrow range, so the histogram is concentrated within small rage of gray levels. Low-contrast image means a low image quality rating, details are hard to distinguish from the background.

Taking into account above considerations, we can use image histograms for automated assessment of image contrast.

Histogram equalization

Punctual operations can be used to improve the image quality by expanding the range of values. Histogram equalization is used to enhance the contrast by spreading the histogram. The idea of histogram equalization is to distribute pixels uniformly over the whole intensity range. In the final histogram, zero values are put between non-zero histogram values. The increase of dynamic range produces an increase of contrast (Figure 2-13).

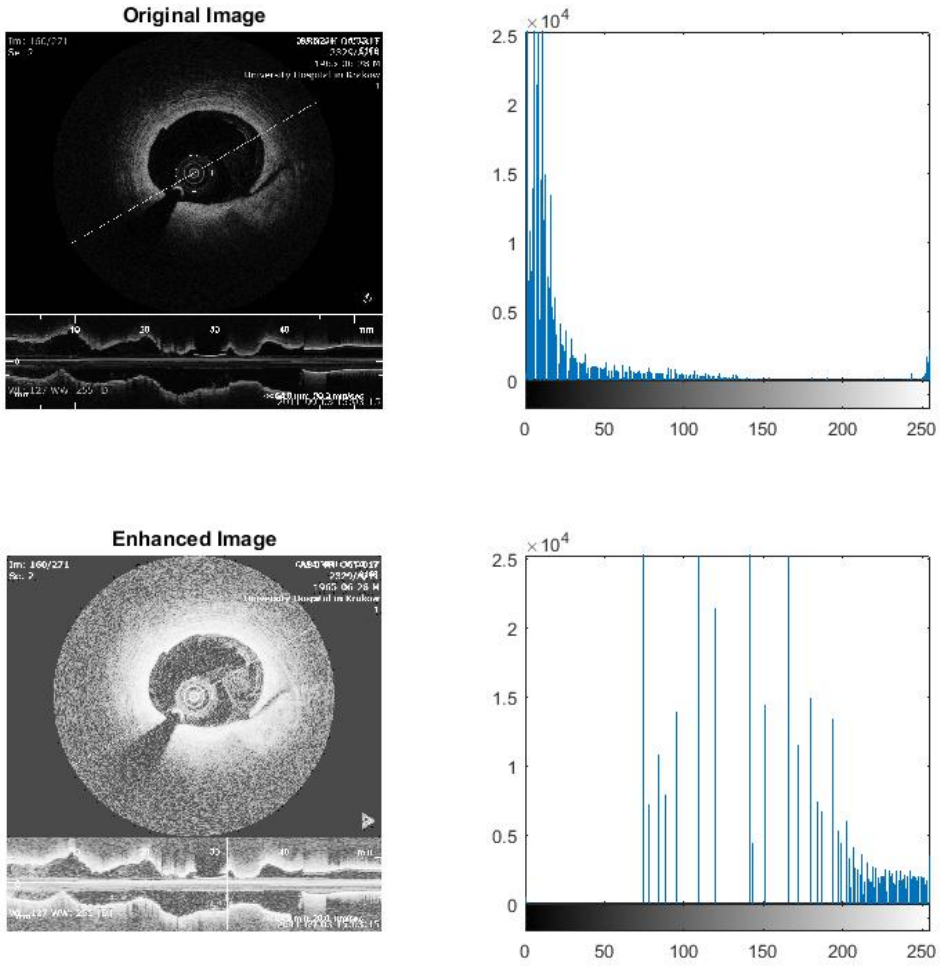

Figure 2-13 Figure shows result after histogram equalization.

Image binarization

Obviously, histograms may be used to distinguish among objects in the image that differ in gray level. This is the simplest example of segmentation. Consider the bimodal histogram that often indicates the presence of a brighter object on a darker background. A gray value f_T may be determined form the histogram and used as a threshold to segment the "foreground" object. The threshold lookup table maps all pixels with gray levels greater than f_T to white and all others to black (Figure 2-14). In that way we receive binary image (Figure 2-12).

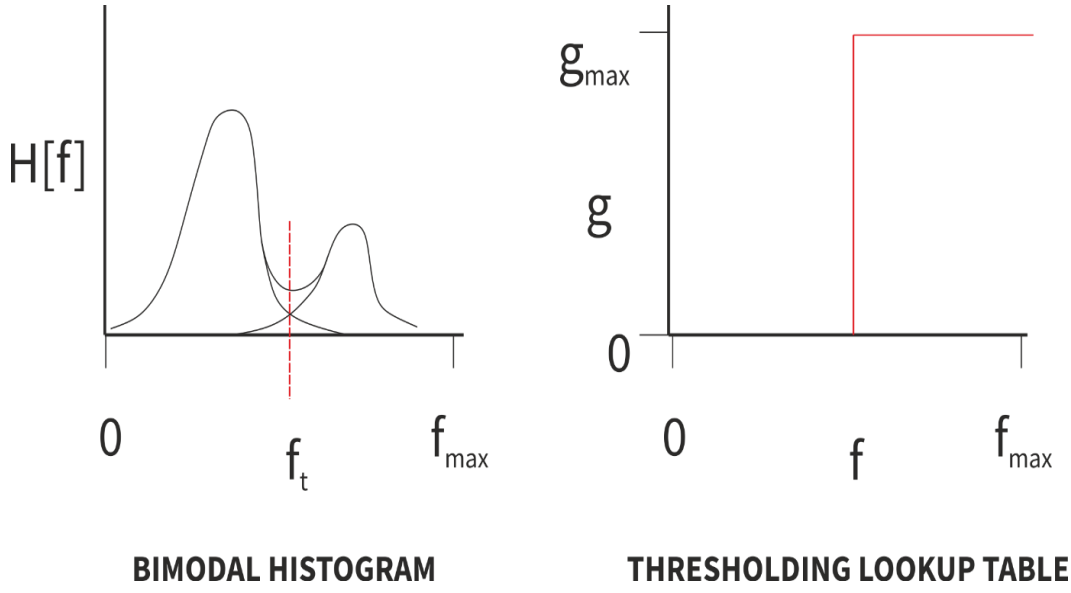

Figure 2-14 Bimodal histogram, showing the intermixing of the "tails" of the clusters for the two objects classes, which produce false identifications in the image created by the thresholding lookup table.

2.4.4. Image filtering

The quality of medical image depends on contrast, resolution, noise (random variations in intensity values) and artefacts. The contrast as we consider above could be corrected using histogram equalization. Another image quality's limitation is resolution of medical equipment. The higher resolution the more details are visible on an image, especially borders, the blur effect is lower (Figure 2-15).

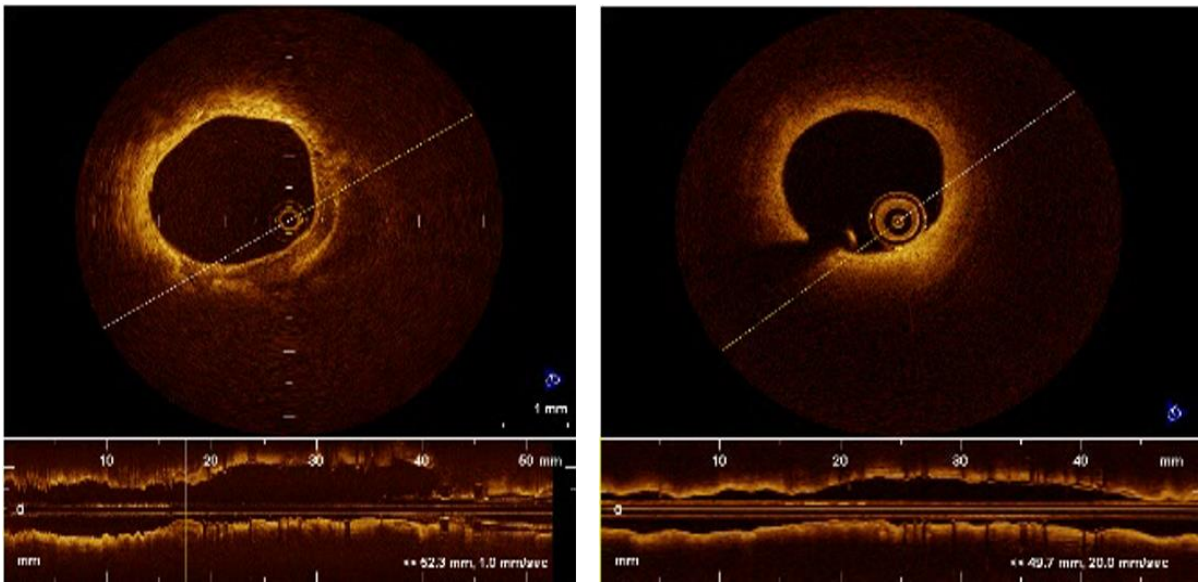

Figure 2-15 There is a cross sectional view of Time Domain OCT on the left side which resolution is lower than acquired by Fourier Domain OCT equipment (right side) .

Another obstacle during image processing are background noise and artifacts which interfere with the correct interpretation of the medical image Figure 2-16 and thus affects the diagnosis.

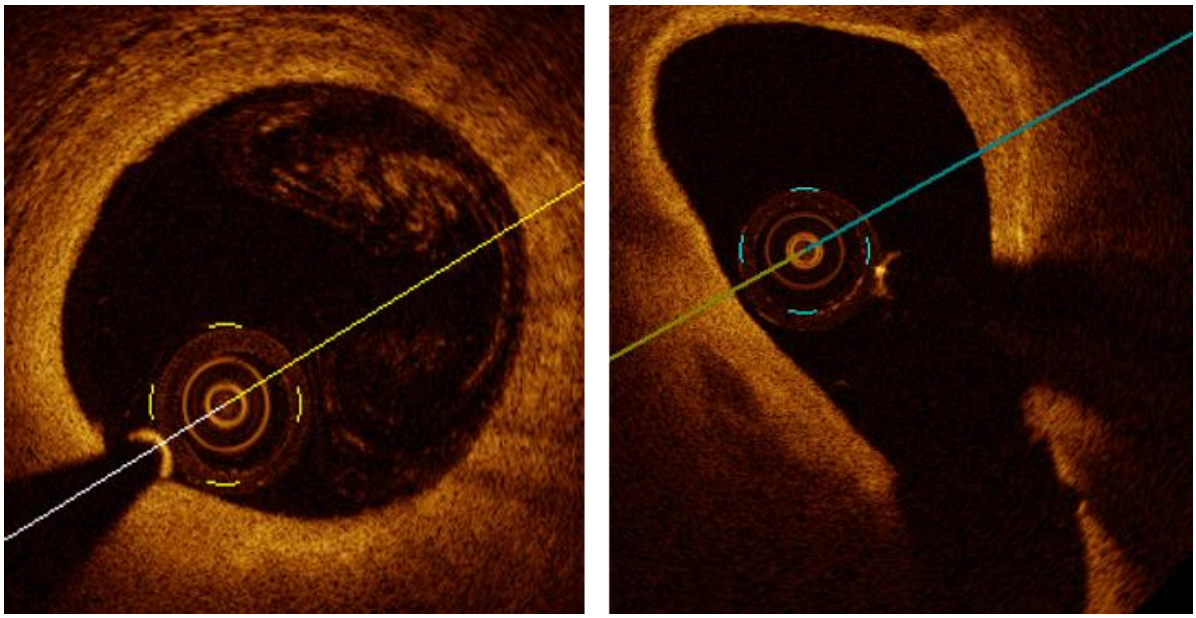

Figure 2-16 Example of background noise on OCT images (left side) caused by not well blood diluted and artifacts from marker (white, blue or yellow line shows direction of probe).

Filtering is a technique for emphasizing certain features or removing other features on image. Image processing operations implemented with filtering include smoothing, sharpening, and edge enhancement [38] [39] [40].

In many common image processing operations, the output pixel is a weighted combination of the gray values of pixels in the neighborhood and filtering is an example of so called neighborhood operation. In algorithms belonging to this category, the value of any given pixel in the output image is determined by applying some processing based on values of the pixels in the neighborhood of the pixel under consideration. A pixel's neighborhood is some set of pixels, defined by their locations relative to that pixel.

Linear filtering

Linear filtering is filtering in which the value of an output pixel is a linear combination of the values of the pixels in the input pixel's neighborhood [41] [38]. A linear filter is implemented using the weighted sum of the pixels in successive windows. The linear filter is spatially invariant and can be implemented using a convolution mask. The convolution mask determines the size of the analyzed neighborhood and it is usually square. It is also characterized by its coefficients determining further calculations of individual neighborhood. The filtering process consists in multiplying the values of individual elements of the image and the mask, and then summing them together and normalizing.

Linear filters include a high- pass filter and a low-pass filter.

Low - pass filter (smoothing)

A low-pass filter is a filter that passes low-frequency signals and attenuates signals with frequencies higher than the cut-off frequency. The actual amount of attenuation for each frequency varies depending on specific filter design. Smoothing is a lowpass operation in the frequency domain [41] [38]. There are standard form of lowpass filters: Ideal, Butterworth and Gaussian lowpass filter.

High – pass filters (sharpening)

It is a filter that passes high frequencies well, but attenuates frequencies lower than the cut-off frequency. Sharpening is a highpass operation in the Laplace filter, the Wiener adaptive filter, Roberts -, Prewitt - and Sobel – gradients [38].

Non-linear filtering

Any filter that is not a weighted sum of pixels is a nonlinear filter. Non-linear filters can be spatially invariant, meaning that the same calculation is performed regardless of the position in the image, or spatially varying.

Probably the most useful nonlinear filter is the **median filter.** The gray value of the output pixel is the median of the gray values in a neighborhood, which is obtained by sorting the gray values in numerical order and selecting the middle value.

The median filter requires sorting of the gray values, which could not be computed as a convolution. Its computation requires more time than a mean filter but it tends to preserve the edge structure [38] [42].

2.4.5. Basic morphological operations

Morphological image processing is a type of processing in which the spatial form or structure of objects within an image are modified. Dilatation, erosion, and skeletonization are fundamental morphological operations. With dilatation, an object grows uniformly in spatial extent, unlike erosion, where an object shrinks uniformly. Skeletonization results in a stick figure representation of an object.

The basic concepts of morphological operations was defined by Minkowski [43] and developed by Matheron [44] and Serra [45]. Stenberg [46] was a pioneer in applying morphological methods to medical and industrial vision applications. In the following sections, morphological

techniques will be described for binary images, because those are used in further study i.e. to detect lumen of the vessel or lipid pools.

Erosion

Erosion is one of the basic operators in the area of mathematical morphology. The basic effect of the operator on a binary image is to erode away the boundaries of regions of foreground pixels (typically white pixels). Thus the areas of foreground pixels shrink in size, and holes within those areas become larger.

The erosion operator takes two pieces of data as inputs: the image and a set of coordinate points – structural element (kernel). This structural element determines the precise effect of the erosion on the input image. Usually such structural element is filled with values of 1 (Figure 2-17)

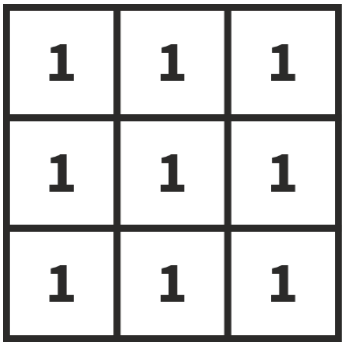

Figure 2-17 Example of structure element 3 x 3.

The erosion operation is used to remove small irregularities at the edges of objects, simplifying the structure of objects. Erosion also causes the complete removal of small elements, often irrelevant from a diagnostic point of view [41] [40] [38] [47] [39].

Dilation

The dilation is another operator in the area of mathematical morphology. The basic effect of the operator on the binary image is to gradually enlarge the boundaries of regions of foreground pixels(typically white pixels). Thus areas of foreground pixels grow in size while holes within those regions become smaller. As the same as in case of erosion, the dilation operator takes two pieces of data as inputs: the image and the structural element. This structural element has a central value equal to 0. Others values of structural element could be optional, but at least one value should be 1 (Figure 2-18).

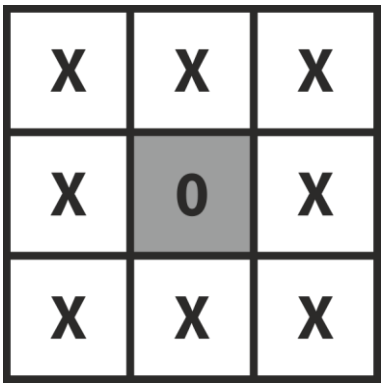

Figure 2-18 Example of structural element for dilation. X is a optional value.

The dilation operation is used in image processing to fill cavities and holes in the image. This operation, by adding pixels and enlarging the object, contributes to smoothing irregularities at the edges, and small objects located close together can be combined into one larger [41] [40] [47] [38] [39].

Opening and closing operations

Erosion and dilation are morphological operations that clearly change the surface of the analyzed area, which in the case of medical images is the main disadvantage of these methods. To eliminate it, two transformations have been introduced, which are a combination of erosion and dilatation. They are opening and closing.

A dilation followed by an erosion defines the morphological closing operation, while the opposite: erosion followed by dilation is an opening operations. The closing operation fills gaps in lines and remove isolated dark pixels, while opening removes thin lines and isolated bright pixels. These nonlinear operations are useful for object size classification and distance measurements [48] [38].

Skeletonization

Skeletonization is a process for reducing foreground regions in a binary image to a skeletal remnant that largely preserves the extent and connectivity of the original region while throwing away most of the original foreground pixels. The notion skeleton was introduced by Blum as a result of the Medial Axis Transform (MAT) [49] or Symmetry Axis Transform (SAT). The MAT determines the closest boundary points for each point being in an object. An inner point belongs to the skeleton if it has at least two closest boundary points.

A very illustrative definition of the skeleton is given by the prairie-fire analogy: the boundary of an object is set on fire and the skeleton is the loci where the fire fronts meet and quench each other. Another way to think about the skeleton is as the loci of centers of bi-tangent circles that fit entirely within the foreground region being considered. Figure 2-19 illustrates this for a rectangular shape.

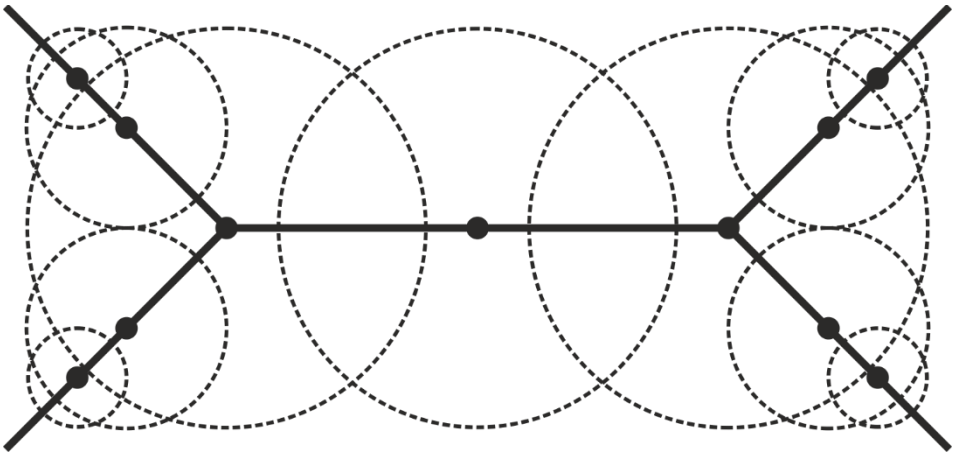

Figure 2-19 It is presented skeleton as the loci of centers of bi-tangent circles.

2.4.6. Edge detection

After the pre-processing of the medical image, the next step is the detection of edges preceding the segmentation of the interested objects. Edges are significant local changes in the image and are important features for analyzing images. Edges typically occur on the boundary between two different regions in an image. There is no universal algorithm to detect all edges for images from different medical imaging methods (Figure 2-20). The method of edge detection should be dependent on the nature of the image and the physical phenomena which generate the specific image.

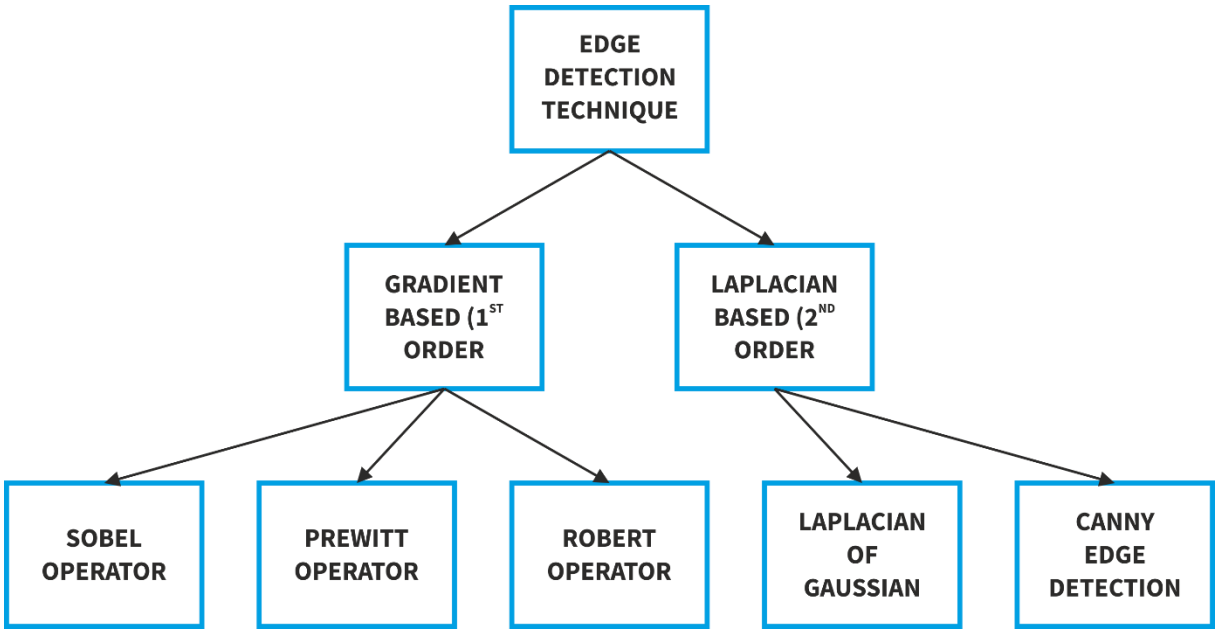

Figure 2-20 Various edge detection techniques.

An edge in an image is a significant local change in the image intensity, usually associated with a discontinuity in either the image intensity or the first derivative of the image intensity.

Edge detection is essentially the operation of detecting significant local changes in an image. In one dimension, a step edge is associated with a local peak in the first derivative.

The gradient is a measure of change in a function, and an image can be considered to be an array of samples of some continues function of image intensity. The gradient is the two-dimensional equivalent of the first derivative and is defined as the vector:

$$G|f(x,y) = \begin{bmatrix} G_x \\ G_y \end{bmatrix} = \begin{bmatrix} \frac{\partial f}{\partial x} \\ \frac{\partial f}{\partial y} \end{bmatrix} \qquad (2\text{-}8)$$

Robert, Prewitt, Sobel edge detection are gradient based edge detection methods used to find edge pixels in an image.

Sobel Operator

Sobel operator uses 3x3 convolution kernels. One kernel is the other rotated by 90 degrees. It is a row edge detector (Figure 2-21).

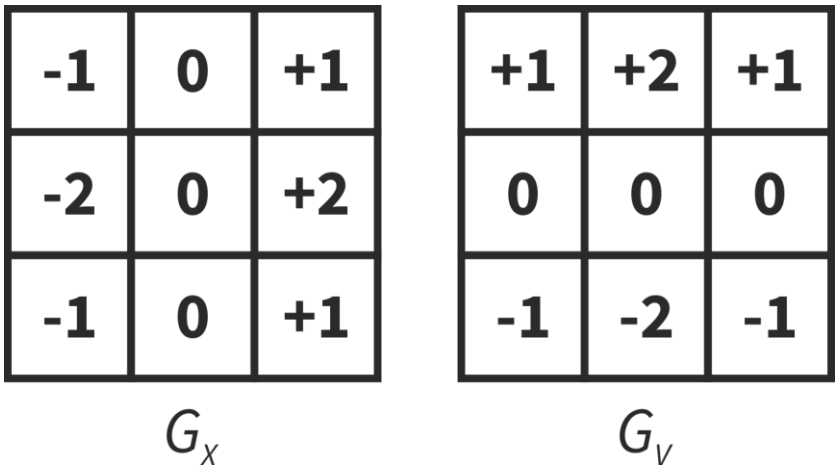

Figure 2-21 Sobel mask filter in X direction and Y direction.

The kernel can be applied separately to the input image for obtaining the gradient component in each orientation GX and GY. The magnitude is given by:

$$|G| = \sqrt{G_x^2 + G_y^2} \qquad (2\text{-}9)$$

Its approximation is:

$$|G| = |G_x| + |G_y| \qquad (2\text{-}10)$$

And the orientation of angle is given by:

$$\theta = arctan\left(\frac{G_x}{G_y}\right) \qquad (2\text{-}11)$$

Prewitt Operator

The prewitt edge detector estimates the magnitude and orientation of an edge. The pewitt operator is limited to 8 possible orientations. This gradient based edge detector is estimated in the 3x3 neighborhood for 8 directions (Figure 2-22). All the eight convolution masks are calculated. The convolution mask with the largest module is then selected.

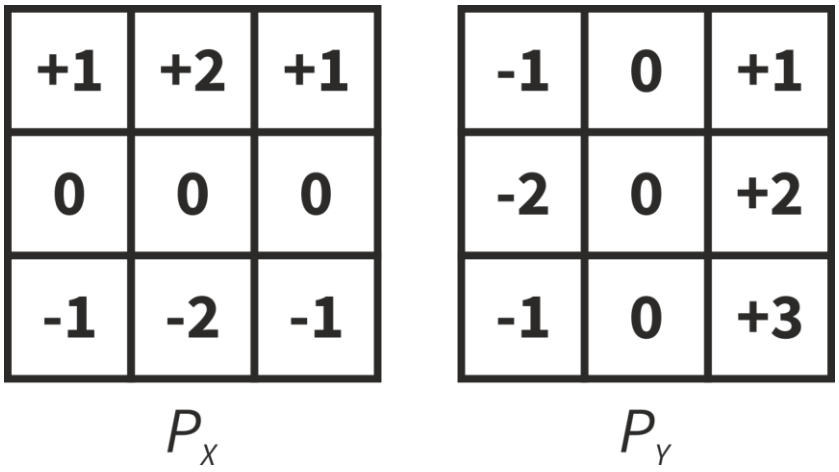

Figure 2-22 Mask filter of Prewitt operator.

Roberts's Operator

Robert's operator is a 2D spatial gradient measurement of an image. The pixel value represents the absolute magnitude of spatial gradient of the input at that point. The operator uses a 2x2 convolution kernel. The kernel corresponds to maximize edges running at 45 degree to each pixel grid. For each of the perpendicular orientations there is one corresponding kernel. The magnitude is given by the same formula as in case of Sobel operator but the orientation of the angle is given by:

$$\theta = arctan\left(\frac{G_x}{G_y}\right) - \frac{3\pi}{4} \qquad (2\text{-}12)$$

2.4.7. Summary of image pre-processing methods

Pre-processing methods are used for preparation of the image for further analysis. The main purpose of these methods is to remove unwanted noise and artifacts and to extract interesting objects in the image. The analysis of medical images and their recognition should be preceded by pre-processing as an important step of further research. Often the effectiveness of the disease identification and the accuracy of the diagnosed condition depend on it. The advancement of technical capabilities and the use of modern equipment still requires the development of image pre-processing algorithms to meet the growing expectations of physicians and biomedical engineers. Despite the involvement of many research groups, the analysis and recognition of medical images is still an inexhaustible topic that poses more and more new challenges for scientists.

2.5. Algorithms for OCT and NIRS images' analysis

The sections above have presented health problem focusing on cardiovascular diseases and briefly shown particular imaging techniques, which have been very widely studied and used in

clinical practice through the recent 30 years to detect and treat them. The direction of development of cardiovascular imaging techniques was determined by human curiosity – a need to get a more in-depth understanding about the atherosclerosis process – to uncover the source of heart disease. During these decades, newer and newer image techniques were developed and improved. The new generations brought better image resolution and shorter acquisition time, further given more anatomical, morphological and physiological information which could potentially help physicians in making therapeutical decisions or help to devise new treatments. The competition between different available cardiovascular imaging techniques became a trigger to develop the imaging methods to derive quantitative tools, promised to be able to identify coronary plaques and further optimize treatment.

In the present thesis, we focused on imaging techniques based on infrared light. A few questions came up with it: Why near infrared light? Why do we need NIRS in OCT era? And the next one, important for a biomedical engineer: what quantative tools can we use to obtain data which are necessary to assess cardiovascular pathology?

The history of near infrared begins in 1800 with Frederick William Herschel (Figure 2-23). He was trying filters to observe sun spots and when he used a red one, he noticed that a lot of heat was produced, which was of a higher temperature than the visible spectrum. After further studying, he concluded that there must be an invisible form of light beyond the visible spectrum and he found that this form of light was also reflected, refracted, absorbed and transmitted in a manner similar to visible light. Sir Herschel had discovered a form of light (or radiation) beyond red light.

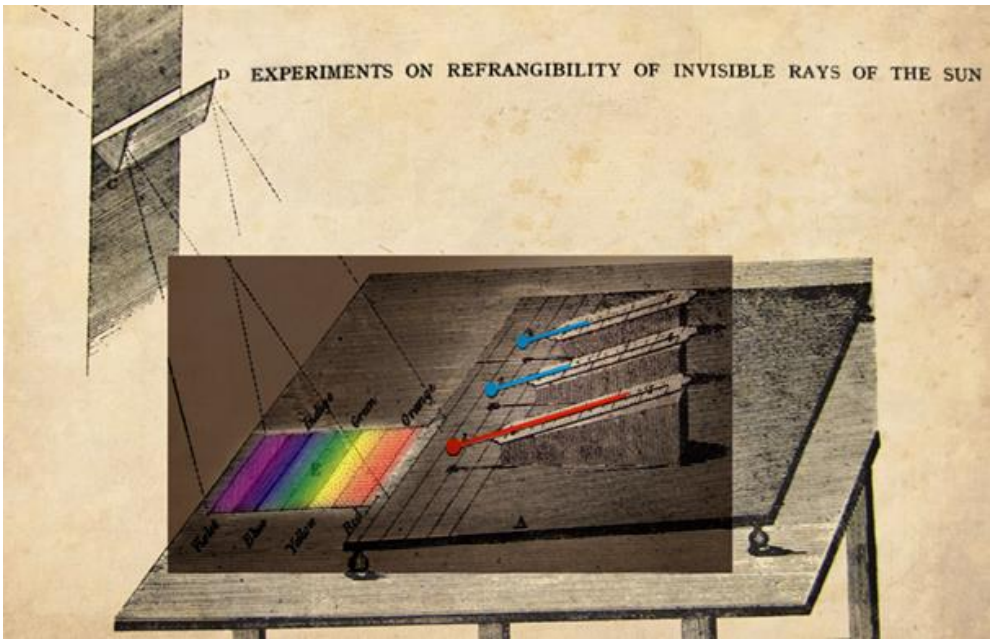

Figure 2-23 The Herschel experiment.[50]

Nowadays, the infrared light is applied in many medical technologies, mainly for the body tissues' analysis. Mr. Huang and his co-workers suggested using infrared light to imaging tissue both in ophthalmology and interventional cardiology. Furthermore, they reported the first clinical use of the 2 dimensional OCT in 1991 [49]. Study acknowledge about OCT axial resolution 10-15 □m, allowing detailed analysis of the vessel wall. In interventional cardiology, it brought hope to obtain in-depth knowledge of CAD because coronary angiography is not a sufficient method to show in detail the plaque composition [24] [25] [26] [50] [51] [52] [53] [54]. There are a lot of studies showing that based on detailed OCT imaging ability, providing the real-time information of the intracoronary pathology – the OCT has opened new avenues of opportunity to recognize and better understand the role of the atherosclerotic lesions and what more, the OCT is very helpful for guiding the PCI procedure to decrease the risk of possible failure [55] [56] [57] [58].

Nowadays, the OCT is considered as the most precise morphologic technique and is used in the increasing number of cases, either in daily clinical practice and research projects.

OCT as a research tool

Analysis of the OCT image for the research purposes is a significantly different process comparing to the routine clinical on-line use in cathlab [51]. Since the beginning of the OCT availability, the cornerstone of the OCT analysis has been lumen assessment and in the stent

coverage assessment. However, the number of suitable clinical situations and study endpoints where the OCT was successfully used is constantly rising. [52] [53] [54] [55].

The offline analysis of the OCT pullbacks is a strenuous and time-consuming work if performed in detailed manual analysis. The OCT analyses demands a skilled, experienced analysts and usually are performed in the OCT Corelab. Generally, for one pullback, the number of the cross-sections that have to be analyzed is usually more than a hundred, it depends on length of the lesion and thickness of the cross-section. The offline analysis includes two parts: quantitative and qualitative analysis. The qualitative part is based on identifying characteristic structures in the vessel wall, the quantitative part is mostly the result of manual tracing of the vessel lumen, stent and stent struts position. For now, no reliable software for the automatic segmentation of the OCT frames commercially exists.

Based on the backscattering and attenuation of light, the OCT data is displayed in a color-coded or gray scale intensity map, allowing for the identification of different plaque components. The type of tissue is determined by the qualitative analysis. The recognition of the plaque is crucial also for the on-line analysis in the cathlab, as the cardiologist can use this information for the optimal choice of intervention technique. Fibrous plaques are defined as homogeneous, signal-rich plaques. Fibrocalcific plaques are typically defined as low backscattering plaques with sharply delineated borders. Necrotic core is defined as a signal-poor region within an atherosclerotic plaque, with poorly delineated borders and little OCT signal backscattering. The fibrous cap is typically defined as a signal-rich layer overlying the signal poor region [56]. The thrombus is defined as masses protruding into the vessel lumen discontinuous from the surface of the vessel wall. Red thrombus consists mainly of red blood cells and is characterized as high-backscattering protrusions with signal-free shadowing. White thrombus consists of platelets and white blood cells and characterized by a signal-rich, low backscattering billowing projection protruding into the lumen [26]. Normal physiological vessel image is recognized according to the typical 3-layer structure of the wall. Another structures usually described in the analysis are protruded tissue or dissections (Figure 2-24).

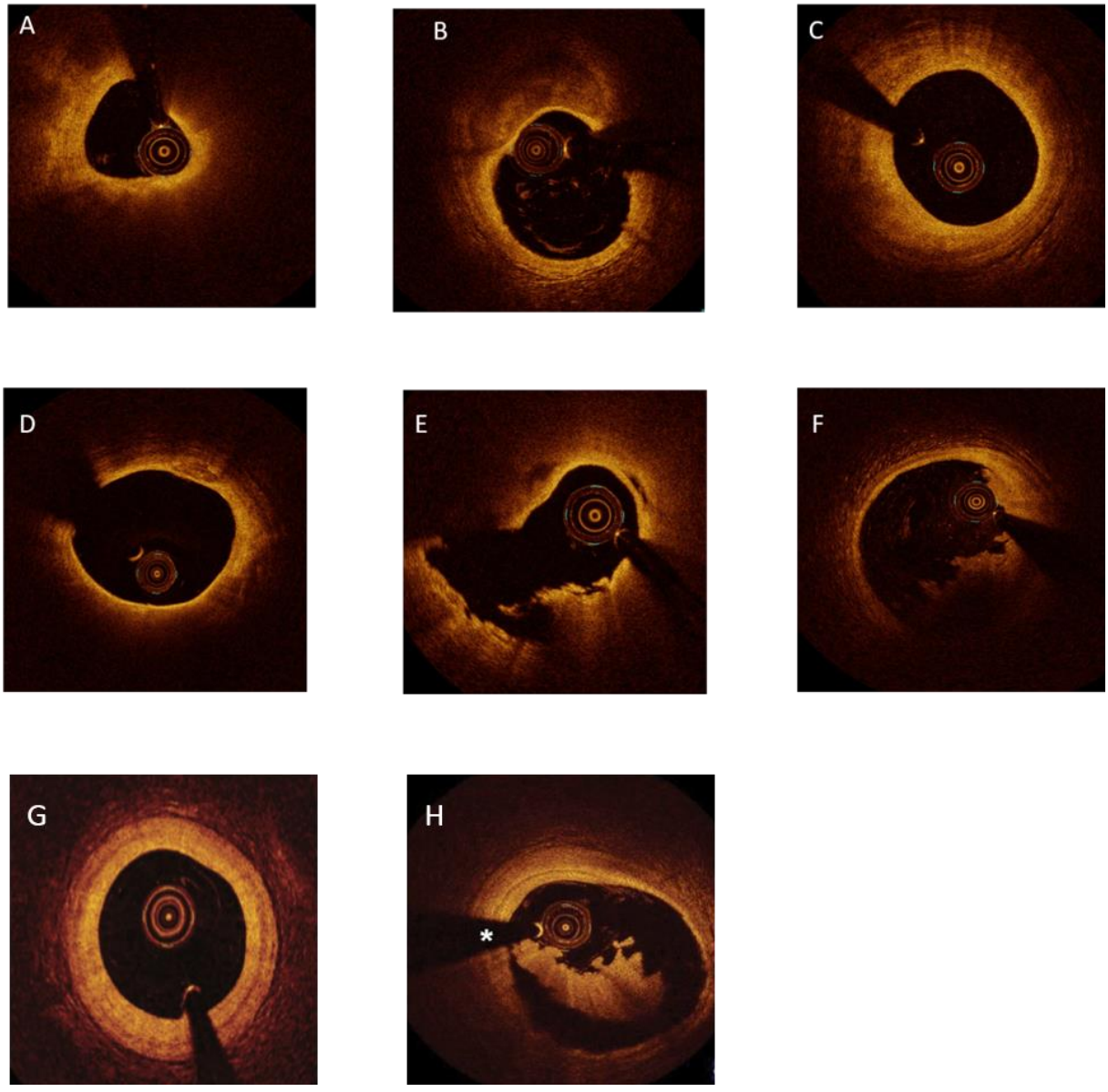

Figure 2-24 Different type of atherosclerotic plaque: A -lipid plaque , B – Calcification, C – fibrous plaque, D – lipid plaque with thin fibrous cap, E – Plaque rupture, F-red thrombous, G- normal vessel, H-white thrombus.

Strut level analysis is based on the lumen contour and stent struts position tracing. If a baseline examination is performed after the stent implantation, struts are described as apposed, malapposed or embedded according to their position towards the vessel wall. If formerly placed stent is analyzed during the follow-up period, it can be described as covered, covered-protruding (disturbing lumen contour, but covered), uncovered-apposed, and uncovered-malapposed [57]. Measurements of lumen area, stent area, minimal and maximal lumen/stent diameters, number of all kind of struts are qualified as quantitative analysis.

OCT as a daily tool

During the regular clinical examination in a cathlab, the acquired data is limited by the time of patient presence on the examination table. Any prolongation of the procedure is uncomfortable, painful for patient and exposes him for adverse effects. Therefore, the operator performs only a standard qualitative assessment of the OCT pullback as the diameter of the vessel, the location and length of stenosis, pathological structures or stent apposition without any detailed analysis of the stent struts.

The OCT imaging provide valuable information about the vessel wall structural pathology, minimal lumen diameter and area, and reference areas proximally and distally to the segment that is about to be stented. The most important information is a vessel wall response to the stent implantation. After the stent placement, the OCT image of the strut positions can make the operator to proceed with another intervention (e.g., postdilatation of the lesion, if the stent seems to be malapposed). The OCT resolution allows to assess the strut apposition or to analyze the acute damage after the stent implantation or even to detect a fracture of the stent in vivo [58] [57]. In the follow-up period after the stent implantation, the OCT is a gold standard for the strut tissue coverage assessment, including the in-stent restenosis or stent thrombosis [59] [60].

Decision making based on the OCT imaging (in fact, OCT guided procedure) is coming to be a daily practice in the cathlab, especially for the angiographically ambiguous lesions [61] [62]. The OCT could be used as a complementary method with the fractional flow reserve (FFR), to either IVUS or NIRS to guide decision making in complex clinical scenarios [63].

As the experience has been rising with the OCT systems, as well as the confidence in the method safety and feasibility, novel applications of the OCT imaging appear [52].

Why we need NIRS in OCT era?

From the time of the first stent implantation in human in 1986 [64], cardiologists were trying to find ways to investigate coronary vessels in vivo from inside. Over these decades a number of catherer-based technologies have been developed to enable direct assessment of the coronary wall in vivo to get new knowledge about the mechanism of disease progression and development of acute coronary syndromes. The vulnerable plaque has been acknowledged for a cause the phenomenon that a clinically silent atherosclerotic plaque suddenly and unpredictably trigger an acute myocardial infraction[9] [25]. Vulnerable plaques are difficult to diagnose as they are often clinically silent and do not cause flow limiting stenosis. Series of

histopathology studies have provided clinicians with a detailed description of morphological findings in culprit lesions associated with coronary thrombosis, myocardial infraction and death. These morphological findings include a thin fibrous cap (< 65 μm), large lipid pool, large necrotic core, fissuring of the cap, calcification, intraplaque vasa vasorum, presence of active macrophages and lymphocytes in or near the fibrous cap [65]. While the histopathology allows for such detailed description, the natural history in disease progression or regression of individual lesion, and the mechanism of plaque rupture and healing are poorly understood. The histology represents only single time snapshot within the disease process. Today most of these characteristic features of atherosclerosis lesion can be diagnosed with intravascular imaging modalities, which are potential to study the dynamic nature of coronary artery disease and the impact of therapeutic interventions in patients.

Atherosclerotic plaque with a large lipid core are a frequent cause of ACS [25] [66]. Near infrared spectroscopy has been introduced into coronary imaging as a modality focused on accurately detecting the lipid content of atherosclerotic plaque [30] [67]. The use of NIRS for characterization of atherosclerotic plaque was initiated in 1993 by Cassis and Lodder [68]. Every substance has a characteristic pattern of absorbance that is analogous to a specific nIR fingerprint. NIRS is able to present the chemical composition of the analyzed object. NIRS is unique for its ability to directly identify and assess the presence of lipid core plaques (LCP). A opposed to the OCT, the applied wavelength of nIR (range between 780 and 2500 μm) does not require blood removal from the vessel to perform analysis and additional contrast injection. Moreover, the intravascular NIRS is the only tool to assess tissue composition behind implanted stent struts [67]. Identification of LCP with NIRS hypothetically has the potential to optimize the length of vessel to stent and to lead to effective utilization of embolic protection devices in the native coronaries, identifying the exact location of lipid-core lesions at high risk of distal embolization [54].

The primary presentation of data is the chemogram of the examinated wall. It has a form of plot of nIR spectroscopy values obtained during a rotation and pullback of the imaging tip within the coronary artery. The color representation extends from the yellow standing for high probability to the red – for low probability. The lipid-core burden index (LCBI) score, summarizes the fraction of LCP in the scanned section on a scale from 0 to 1000.

From the analysis of strengths and weaknesses of each individual imaging modality, it appears that the combination of two or more imaging technologies could improve the LCP and vulnerable plaque detection.

Room for a biomedical engineer - Computer-assisted quantitative evaluation of arteries' lumen and lipid plaque by different Intracoronary Imaging Methods

Today intravascular imaging offers new levels of anatomical details and new dimensions of information for the diagnosis of coronary artery disease, paving the way to an improved understanding of the behavior of the atherosclerotic process and the effects of different treatment strategies. Growing number of OCT, NIRS, and intravascular studies entails the development of computer-assisted quantitative tool and algorithms for evaluation od diseased arteries.

Automatic lumen contour detection can be a very challenging step as OCT images typically contain various artifacts like guidewire shadowing, motion artifacts, bifurcations or non-diluted intraluminal blood. As the analysis of OCT images is a demanding process many automatic methods have been developed for lumen detection in the OCT [3] [69] [70] [71] [72] [73] [74] [75] [76] in recent years (Figure 2-25).

These methods usually employ multi-step image processing techniques including:

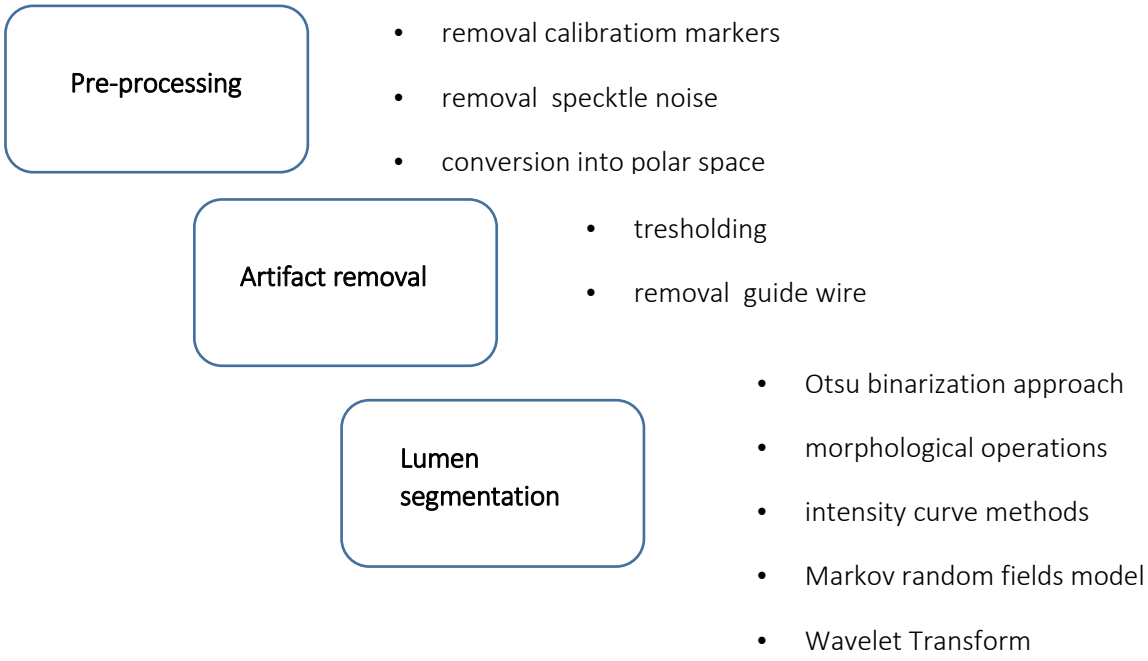

Figure 2-25 Review of used methods in image processing.

Different OCT technologies, various image textures, diffused and complex lesions, furthermore, not well diluted blood from vessels have a huge impact on the segmentation outcome as well as on the feature extraction in above described methods [3] [69] [73] [77]. Additionally, images with poor luminal or substantial luminal blood in contact with the arterial wall can be not well delineated by active contour methods [78].

Methods developed and proposed by other researcher teams tend to have a high accuracy, practicability, and a good computational cost but require high quality images including only one kind of individual artifacts. Due to these obstacles, there is still a room for a complex solution which is expected to improve the segmentation process for most cases. Most of the methods listed above can only be applied for the images of healthy vessels without bifurcations [70] or for good quality images without artifacts [69] [76].

In this thesis, we propose a solution which can be used to analyze poor quality images as well as images with diseased vessels and bifurcations in course of OCT pullbacks without excluding any frames. Developed algorithm was described in details in Chapter 3.

Unlike OCT image processing, NIRS images are not so widely described as researchers tools. There are commercially available algorithms to automated lipid pool detection but to our best knowledge there are no papers about the algorithms used for it. The main limitation of commercial solutions is that, they do not allow to calculate the LCBI values in fragments with artifacts possibly caused by the presence of calcifications or the guide-wire shadowing.

Our aim was to develop the algorithm to detect not only the lipid regions, which are clearly visible but also these hidden under artifacts.

The proposed algorithm for detection of lipid poles under the artifacts and for calculation of new medically important features as lipid arc or lipid length is discussed in Chapter 4.

The main topic of the doctoral thesis is the detection and analysis of lumen vessel and lipid pool analysis (Chapters 3 and 4) in the assessment of new methods of treatment of heart diseases. As part of the chapters, innovative algorithms are presented and further the proposed methods are discussed and verified and compared to commercially available solutions.

CHAPTER 3

3. The Optical Coherence Tomography image processing

3.1. The OCT images processing based on perception parameters

To provide a proper image interpretation, while detecting and diagnosing the development of coronary artery disease (CAD), the image analysts and cardiologists mostly rely on their own visual ability in medical imaging studies. Visual ability is a complex notion depending on a variety of interrelated visual and non-visual factors, such as visual acuity, mobility, physical ability, depression measures, and cognition (thinking, understanding, learning, and remembering).

Since the 1970s a significant progress was made in development of coronary diagnostic techniques, starting from the angiography, through intracoronary imaging, which brought a breakthrough in diagnostic possibilities and treatment options for coronary artery disease, especially atherosclerosis. The progress concerns not only imaging technologies but also methodology of analysis. A development is significantly noticeable in methods that contribute to more accurate assessment of progression or regression of vessel disease and optimization of coronary procedures.

While the effectiveness of image analyses in searching lesions depends on accurate image interpretation, there is a paucity of investigations focused on assessing and improving the image analyst's effectiveness in finding lesions in intracoronary images.

As it was presented in the previous chapter, intracoronary imaging plays an important role in daily clinical practice, by providing an improved imaging quality of the view of vessel wall and lumen interface. It helps to better understand the pathophysiology of atherosclerosis, plaque vulnerability, and vascular biology. Consequently, we found very important to better understand the process of visual image interpretation by the human, and the process of lesion detection. There are a lot of studies using an eye-tracker to investigate cognitive processes during interpretation of various medical images [79] [80] [81] [82] [83] [84] [85] [86] [87], but there are few applications of eye-tracker in cardiology area[83] [84] [86] [88].

Medical images are not self-explanatory and need to be correctly evaluated in order to make the proper diagnosis. Anatomical structures can camouflage features of clinical interest. Lesion can have very low prevalence, affecting the decision-making process. This makes image perception the most prominent source of mistakes during the diagnostic process [89] [90].

What makes the intravascular OCT images one of the most interpretation-challenging medical images?

The qualitative analysis of the vessel wall depends on optical characteristics (as homogeneity, reflectivity and demarcation) of vessel wall structures [91]. Furthermore the distribution of diagnostic information in the OCT images is not only related to optical characteristics of tissues but also to the anatomy of the coronary vessels as bifurcations, vessel tortuosity, vessel angle, the size of the plaque affect the shape of the vessel as well. All these factors contribute to the complexity of OCT image assessment. Consequently this time-consuming task is challenging for the human expert, especially for a less experienced analyst/cardiologist, who is theoretically more likely to misinterpret the particular patterns in the OCT image.

Most of the lesions leading to myocardial infraction have at least 50% of diameter stenosis and are located in the coronary segment with a high movement compression [92]. Drawing the lumen contour is a first step to assess whether the vessel is narrowing. The accurancy of lumen contour determine the correct risk assement and selection of the appropriate treatment device: type and size of stent or balloon. Automated lumen detection, could speed a cardiologist's analysis, but still we do not have a knowledge how cardiologist, expert interpret the received image?

This part of the study was addressed to better understand the process of image interpretation using available perception-cognition tracking technologies. The specific aim is to facilitate the interpretation process, to achieve safer and better quality care for patients, and to increase the efficiency and effectiveness of experts-cardiologist work. To achieve this goal, we attempt to estimate the relation between the eye focuss duration time and amount of visual information picked up from the image [93] [94] [95] [96]. A second objective of our study was to check if the order of object identification has been determined by their characteristic features (shape, intenisity, apearance).

Software based on expert perception parameters analyzing intravascular images could enable to effective automatic detection of basic cardiovascular pathologies.

The sections below are based and reffered to my publications [97] [98] and results presented during PCBBE Conference 2017 in Krakow [99].

Materials

All OCT images used in this part of study were acquired by commercial Fourier Domain OCT systems (C7-XR OCT Intravascular Imaging System, St Jude Medical Inc. St Paul Minnesota) and were analyzed on dedicated software LightLab Imaging (the same manufacturer) run on a certified OCT workstation.

Eye movement signals were collected during OCT analyses using the eye-tracker JAZZ-novo multisensory system (Ober Consulting Poland) with a sampling frequency of 1000 Hz. The system is based on infrared oculography and tracks the eyes motion by measuring the intensity of reflected infrared light. The difference between the amounts of IR reflected back from the eye surfaces carries the information about the change in eye position, allowing to measure eye movements in horizontal and vertical axis.

Eye tracker device's Measurements with the eye tracker device are based on visual scanning of the human eye movements, especially Fixational Eye Movements (FEM), which are defined as involuntary, small-magnitude eye movements continuously produced during the fixation.

The eye movements data was recorded using the dediacted application JazzRecorder 2.5 in the binary format, simultaneously with audio signal recording with the microphone placed on the eye-tracker device. The original Jazz-novo data can be also exported to a text file for use in any commercially available analysis software. In this part of study JazzManager 2.21 was used.

To record head movements, the Camera Titanium TC101 ONYX, 800x600; FreeWebcamRecorder AMCAP version 1.00, was used. The image recording resolution was 640 x 480, and the frame rate was 25 fps.

CamStudio Portable version 2.00 was used to record all on screen display and audio activity while using the OCT workstation and save them to a video file.

All medical content to analyse were displayed on the monitor EIZO - Eizo EV2333W; 1920X1080, 32 Bit – screen being part of the OCT workstation and dedicated to medical images.

The eye signal was acquired simultaneously with video-registration of analyst's head movements and screen recording. The camera was placed on the head of the analyst sitting in the front of the OCT workstation, so that the wole computer screen was in camera's field of view. The screen recording mode allowed to register every analyst's move during the OCT

analysis. The data recorded from the eye-tracker, the head camera and the workstation display were synchronized by a voice command.

To correctly visualize the eye movements on the OCT image the calibration and measurements procedures were developed (Table 3-1 and Table 3-2):

Table 3-1 The calibration procedure

1	The study subject sits at least 50 cm from the monitor.
2	The monitor is placed in front of study subject face, so that the study subject is able to look at the center of monitor.
3	Set the camera in a position to register the entire screen monitor.
4	Make sure that the camera is in the right position.
5	Set the screen in the recording mode.
6	Set the camera in the recording mode.
7	Recording starts after the voice command "start".
8	The study subject looks to the center of the screen, and then directs the gaze from corner to corner clockwise. Starting from the upper left. Moving gaze from one corner to another should be fast. Focus gaze at each corner - 3 seconds. Repeat the process three times.
9	The calibration is finished after study subject verbal command 'stop'.
10	Inform the study subject that he must not change the position of the Eye-Tracker and the camera. Study subject is allowed to change his body position, but eyes still should be along the axis to the screen center.

Table 3-2 The study methodology

1	The calibration is performed before each measurement.
2	Load the visual content (an OCT image) to analysis.
3	Before the analysis, the study subject should say “start” and move his gaze from corner to corner clockwise, starting from left-upper corner.
4	Measurements are finished after study subject voice command “stop”.
5	Save files (camera and the eye-tracker records).
6	Make sure that files are in right location and in correct format.

Calibration

A simple linear transformation based on 5 calibration points was used to calibrate the eyetracking data[100]. The calibration rectangle of known dimensions and the coordinates of the rectangle corners were displayed on the workstation screen (Figure 3-1).

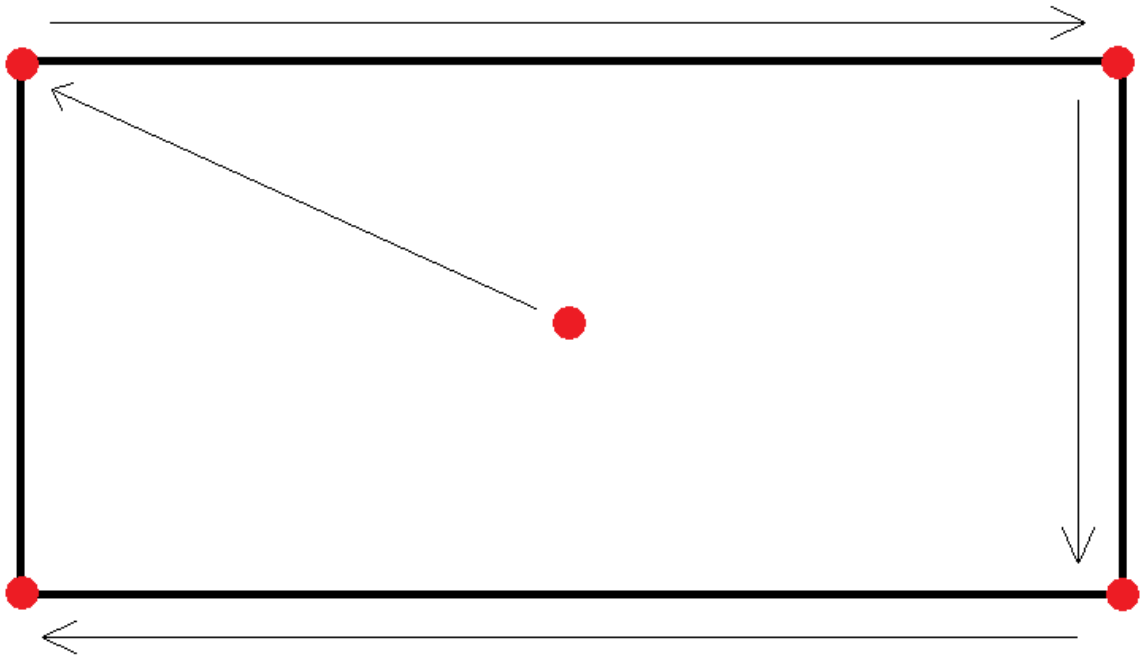

Figure 3-1 Calibration rectangle with marked focus points

During the calibration process the analyst had to focus on the rectangle corners (red markers) as well as on the point at the rectangle center by 3 seconds. The process was repeated three times. The sitting position of each analyst was set individually so that the center of the rectangle was located along the analyst's axis view. The calibration results were presented as a plot of eye position in *x* and *y* directions. The transformation between the coordinate system of the screen and camera was given by the following equations:

$$x_s = a_0 + a_1 * x \qquad (3\text{-}1)$$

$$y_s = b_0 + b_1 * y \qquad (3\text{-}2)$$

Where:

(x_s, y_s) – coordinates of the points on screen,

(x, y) – coordinates of eyes position,

(a_0, a_1) and (b_0, b_1) – coefficients calculated by the method of least squares.

The indicator of properly performed calibration was a rectangle-shaped plot. The received plot had a tendency to lean to the right site and usually the values in the Y axis are much more lower than values on the X axis, making plot flatten (Figure 3-2).

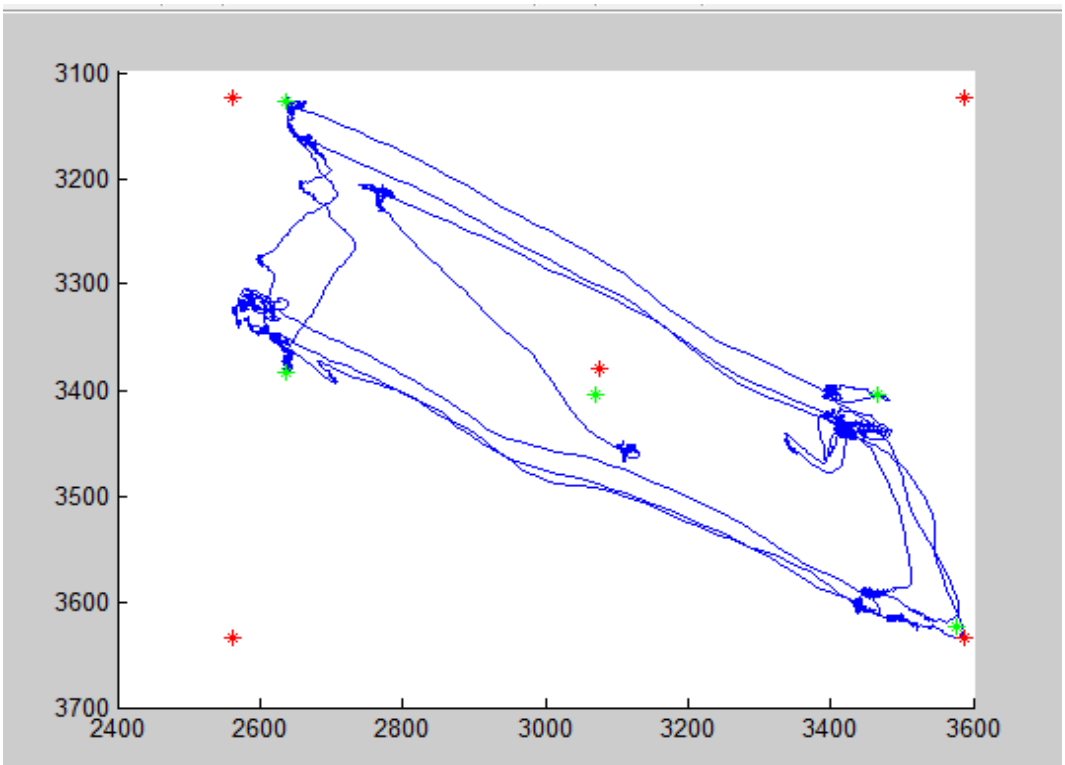

Figure 3-2 Rectangle-shaped plot before calibration

The script for calibration requires knowledge of the coordinates of the calibration rectangle. The red asterisks represent the expected points of rectangle. There are the minimum and maximum values of obtained data along the X and Y axes. The center of the rectangle was calculated as the average value of the two extreme points. Green asterisks were the focus points, calculated as an average of 200 values near the extremes and at the center of the rectangle.

To obtain a rotation of the measurement, the algorithm calculated the difference in Y values on the right and left sites of the rectangle. This difference is then subtracted proportionally from each point. The linear relationship is achieved by determining the position of each point based on X value depending on the extreme (maximum) values of the axis. Translations are obtained by shifting each point by a value equal to the difference between the center of the calibration rectangle and the center of the acquired rectangle-shaped plot. To finish the translation process the data must be properly scaled. The distances to the centers of the both calibration rectangle's sides are calculated for each point. Afterwards, depending on the calculated distance, each point is approximated to the nearest side with the appropriate ratio. Example of a transformed eyetrack data plot is presented in Figure 3-3.

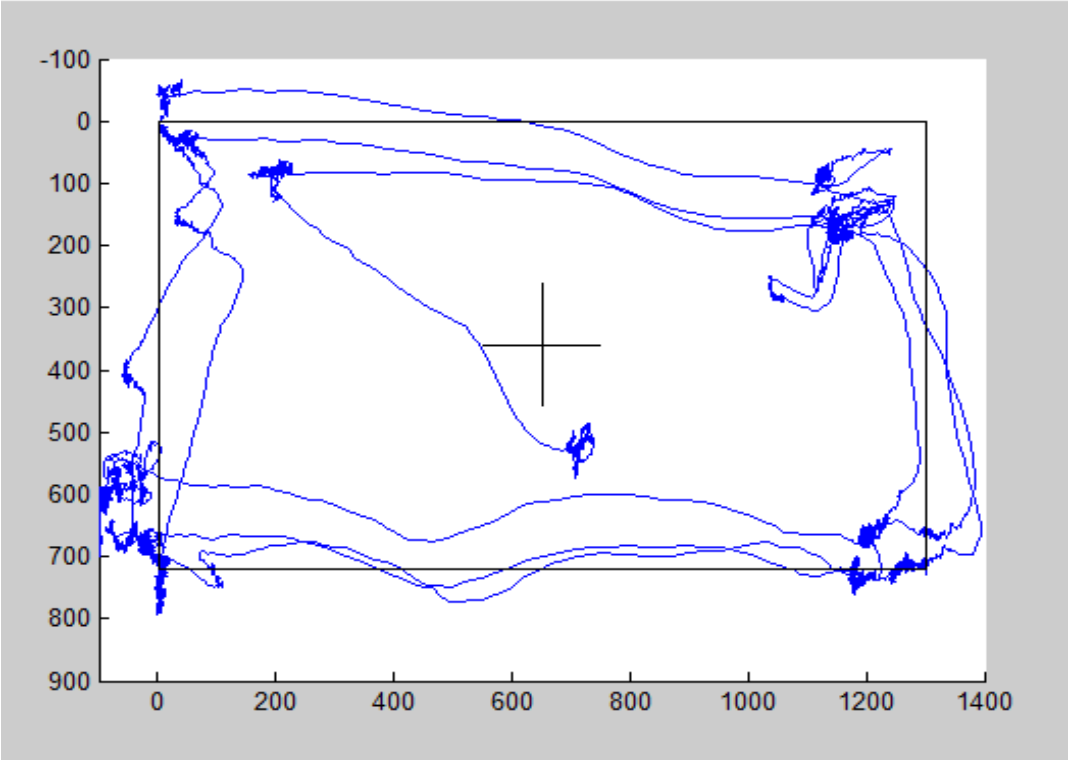

Figure 3-3 Final results of calibration procedure.

The calibration process determined the coefficients used to transform the data collected during the OCT analysis. Calibration results were saved to the text files for later data processing. Further eye-movement data processing was performed with an algorithm originally developed at AGH-UST [101] in which I made corrections and adaptations where it was necessary.

Data acquisition

Calibrated data were used to generate the analysts' eye-path which was afterward overlaid on a medical content presented the workstation screen. Synchronization of both, the film and the acquired data was performed by the audio signal. Additionally, it was observed that a characteristic analysts' oculomotor response is related to the eye fixation on a drop-down list of prepared parameters' names. (Figure 3-4).

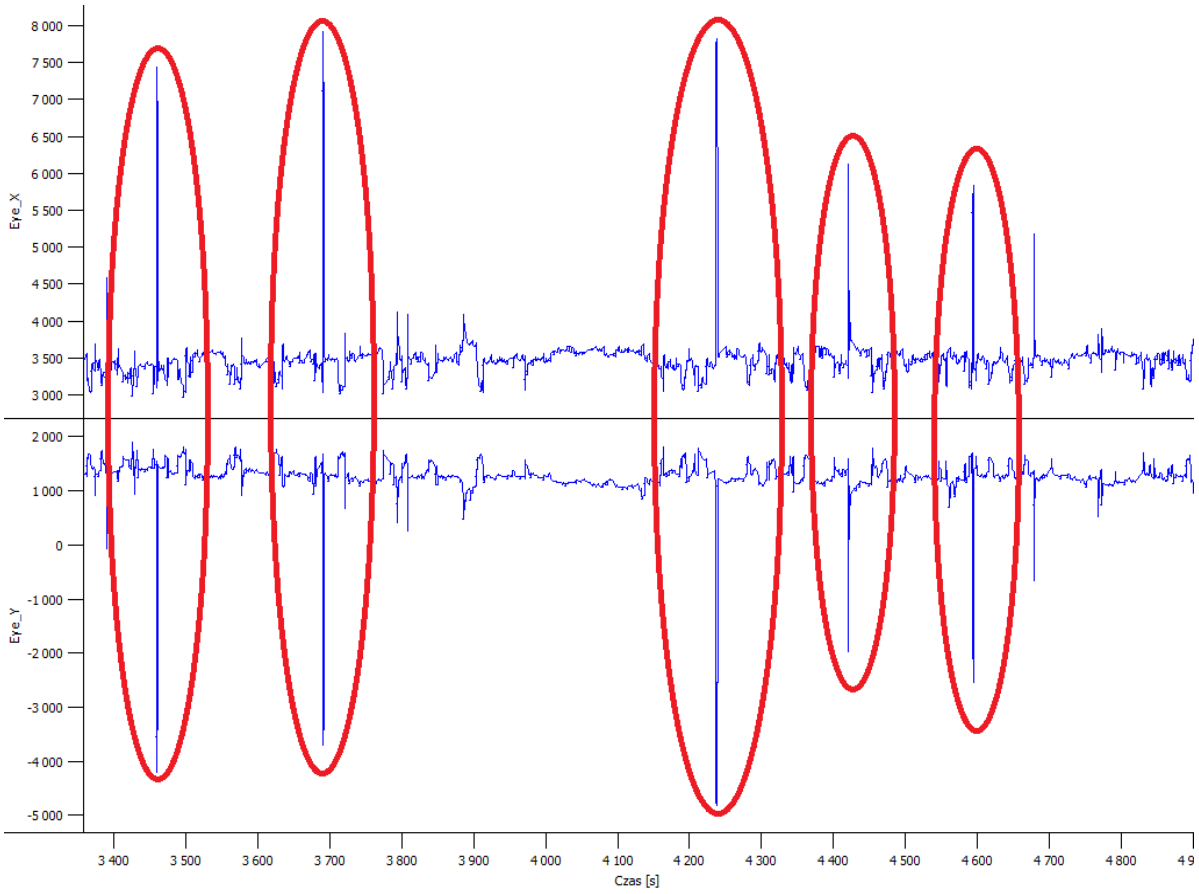

Figure 3-4 Red circles show analysts' coulomotor response for the drop-down list.

In order to be able to synchronize the eye-movement signal and the video recording with the analyzed OCT frames, the information of the time intervals between the displays of the drop-down list was essential. The acquired eye-movement data was analyzed in the context of the fixation area, fixation duration and areas on which the analysts' were concentrating multiple times on each analyzed OCT frame. The algorithm analyzed successive vectors of eye movement over time. This data was processed in order to reveal the speed of eye movements on the workstation screen. The script detected parts of the screen where the observer's eye movement was slower and considered them as fixations areas. Fixation duration was defined as the longest time of eye-focus on each analysed OCT cross-section. Then the script was detecting regions of the screen which was the most often observed and counting the returns of the observer's gaze to these regions. The eyetracking parameters were estimated twice. The first time, during the quantitative OCT analysis, which continues from the moment of displaying the current OCT frame to the lumen contour acceptance. The second time during the qualitative OCT analysis which started from the lumen contour acceptance and ends with displaying the drop-down list of the menu in order to choose the right name for the marked pathological structure.

Results

The results of analyses were compared between an analyst in training (Analyst A) and an experienced analyst (Analyst B). Both analysts assessed the same vessel, the same region of interest. The quantitative analysis was performed correctly in case of each analyst. The lumen contour was traced correctly along the entire OCT pullback and accepted by a supervisor – cardiologist. In contrast, the qualitative analysis, was performed differently by both analysts. The region of interest contained several potentially pathological patterns, bifurcations and artifacts which could influence the correctness of image interpretation. Analyst B performed the qualitative analysis properly, all patterns were detected and interpreted correctly. Analyst A classified plaques accurately only in 72%.

Another notable difference was the duration of analysis. Analyst B needed less time for performing the overall analysis than Analyst A. The average fixation duration was longer in the case of Analyst B compared to Analyst A (Table 3-3). However, the average number of the areas of fixations as well as the average number of the areas on which the analyst was concentrating multiple times were lower. Therefore, the analysis time was shorter for Analyst B than for Analyst A.

Table 3-3 Colleted calculated parameters (modified from [98]).

	Experienced analyst Analyst B	Analyst in training Analyst A
Average fixation time in quantitative analysis [s]	3685,7	2572,2
Average fixation time in qualitative analysis [s]	2773,6	1654,8
Average returns count in quantitative analysis	19,5	30
Average returns count in qualitative analysis	4,78	7,1

Both analysts had different scenarios of the vessel assessment. Analyst A, before beginning of the analysis, overviewed the whole region of interest frame by frame. Looking not only for a cross-sectional views but also in longitudinal view Figure 3-5 during the whole analysis process. It allowed for the familiarization with the vessel structure, the placement of the

characteristic features such as bifurcations (branching of the vessel), probe artifacts in the entire fragment to be analyzed. On the contrary, Analyst B immediately started the analysis of the vessel, frame by frame.

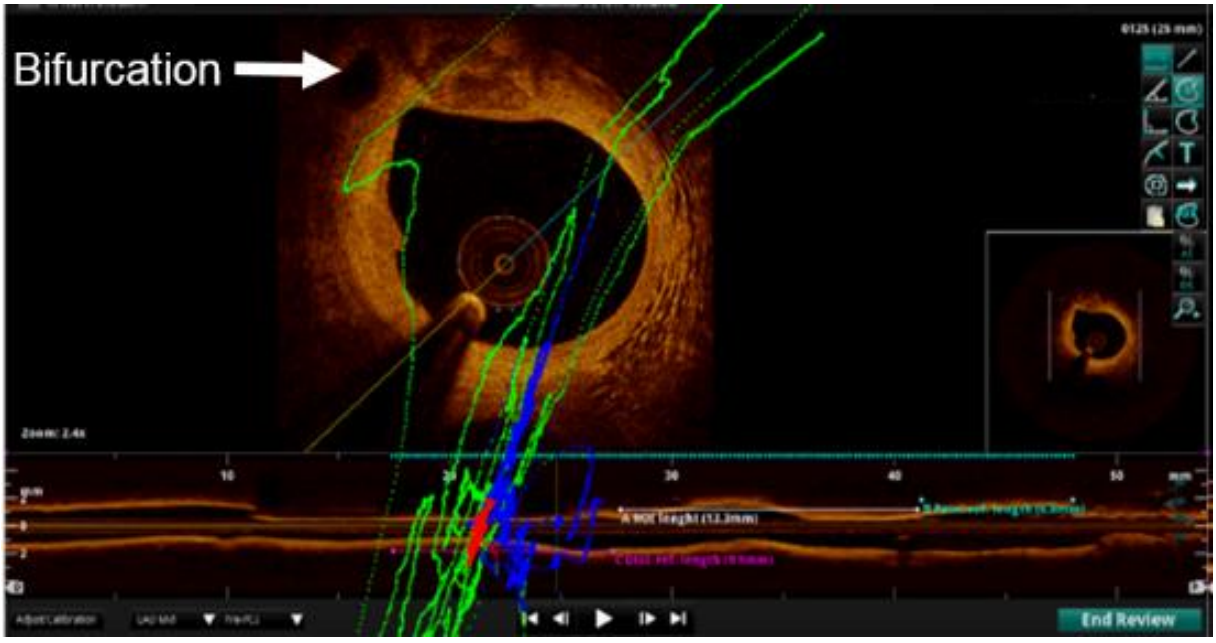

Figure 3-5 Analyst A oberved the longitudinal view (modified from [97]) .

The perception analysis of the single frames indicated the differences of the eye trajectory between the analysts. Analyst B scanned a greater area of the vessel compared to Analyst A (Figure 3-6,Figure 3-7,Figure 3-8).

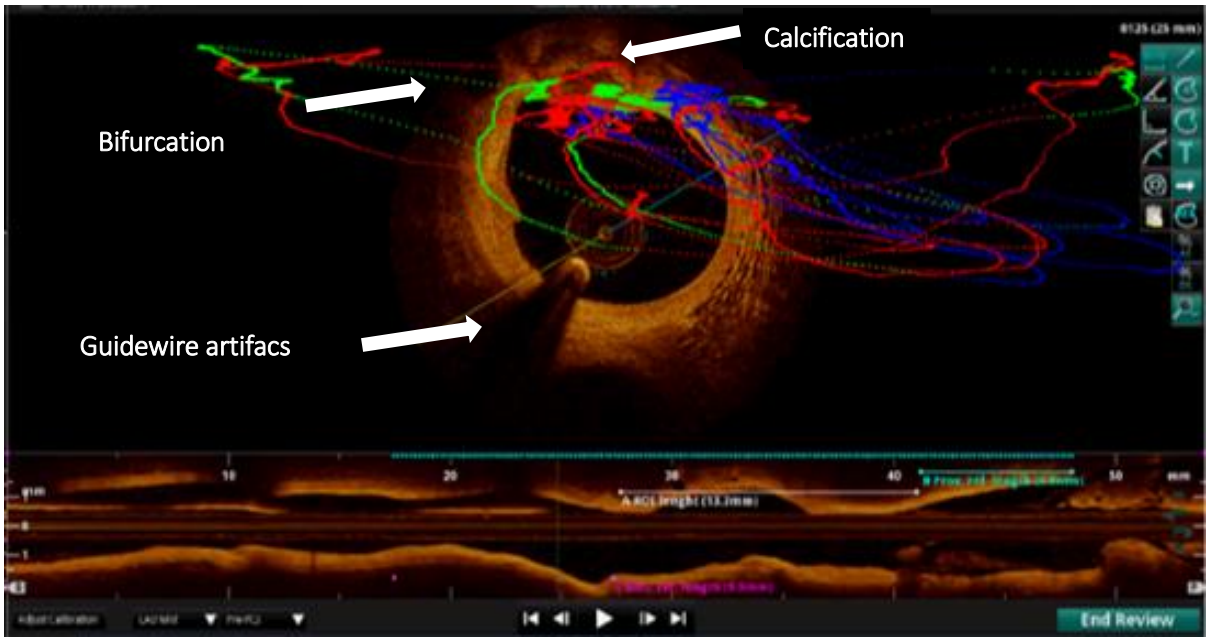

Figure 3-6 Analyst B observed small bifurcation, calcifications. And scanned extensive area. Green trace presents eye path, red trace - the fixation area and blue trace - the eye returns areas (modified from [97])

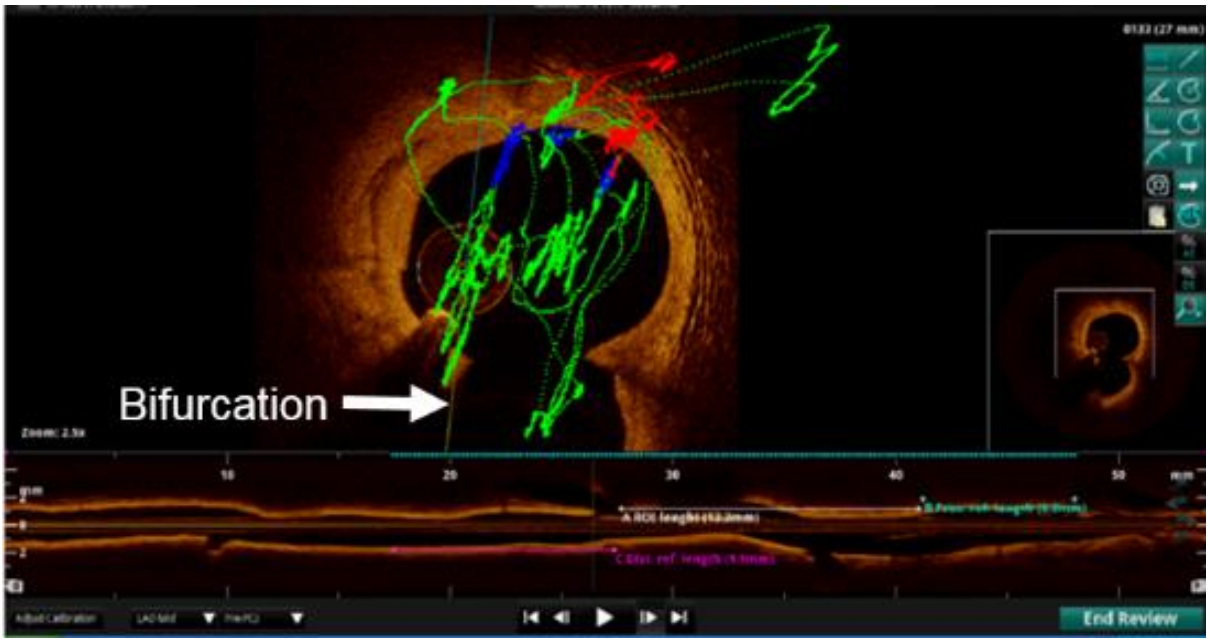

Figure 3-7 Analyst A focus in small area.. Green trace presents eye path, red trace - the fixation area and blue trace - the eye returns areas (modified from [97])

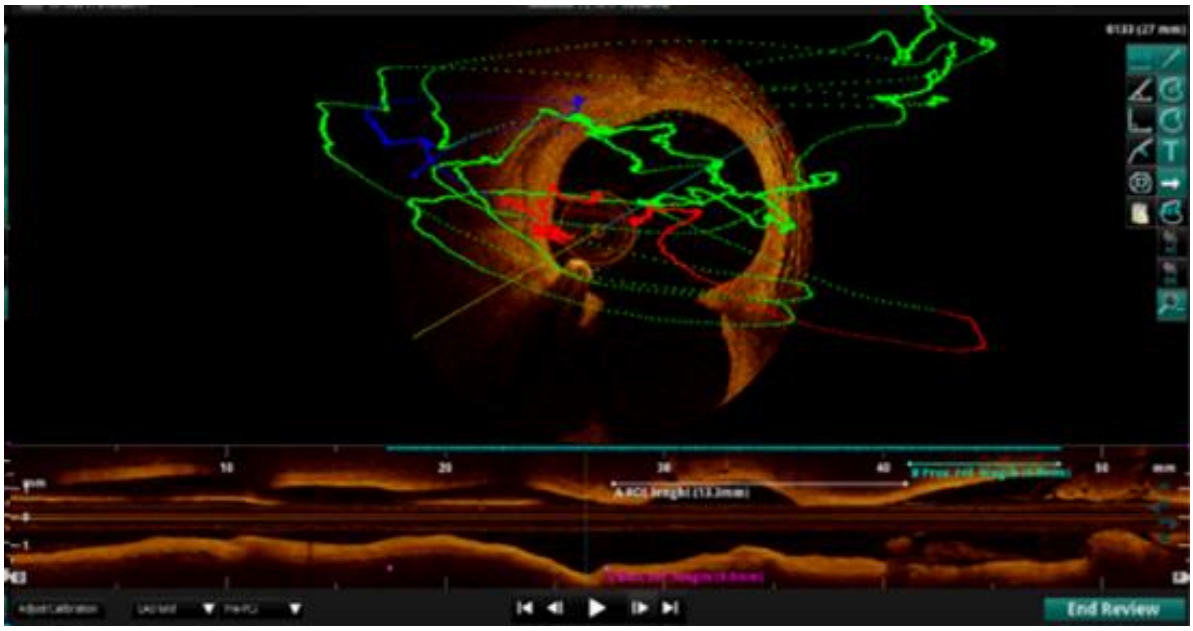

Figure 3-8 Analyst B observed small bifurcation, calcifications. And scanned extensive area. Green trace presents eye path, red trace - the fixation area and blue trace - the eye returns areas (modified from [97])

Similarly, in the case of both analysts, a lower number of fixations on the image areas indicating pathological features after drawing the lumen contour (after quantitative analysis) was observed. It probably shows that during drawing the contours, analysts simultaneously try to analyze the image qualitatively. They interpret the whole image, and at the same time classify the observed structures. However, Analyst A made eye fixations on certain characteristic image

elements, such as the guidewire which causes the artifacts and the catheter (presented as the shadow on every cross-section).

In the presence of the bifurcations further differences can be noted. Analyst B made eye fixations directly on the bifurcations, on every frame where this feature appeared. Whereas Analyst A focused on bifurcation only the first frame where it was visible however on the next frames he/she observed the longitudinal view, where the branching is also apparent.

Summary

Using experts' eye-path to obtain objective visual information to identify region of interests durig analysis procedure is getting increasingly popular recently. The main goal of eye-tracking analysis was an attempt to define the amount of information acquired from the perceived zone.

This part of study showed that the following parameters: the fixation duration, the fixation areas and the eye returns count could be used to assess the perception patterns of the important structures on the OCT cross-sectional images of vessels. The analysis of eye globe trajectories indicated that the differences in the image interpretation highly depend on analysts' level of experience. Not all pathological features were detected and labeled by the less experienced analyst. Achieved results present different strategies of OCT pullback analysis between the analysts. Unlike Analyst B, Analyst A payed attention to the bifurcations, guidewires and artifacts.

In the future projects the study groups should be extended and further differentiated in terms of experience level to investigate the individual visual assessment strategy. The reliable identification and description of visual search strategy can contribute to the better understanding of human perception and image interpretation. The attempt of defining characteristic regions of OCT images based on the eye-path analysis has been used as a background for creating automatic algorithms for detection of interesting structures and their automated, initial interpretation. This solution is expected to speed up the OCT analysis, which is still a time-consuming process. Another direction of further studies could be based on investigating how the strategy of analysis changes in different time points during the learning process. This information could be used to create an individual learning pathway and make the training process faster for radiologist, technicians and physicians.

Based on the first ourcomes presented above, I tried to develop the algorithms to automatic lumen detection, validated mainly in a poor quality OCT images with bifurcations and artifacts

from blood not diluted sufficiently. The proposed algorithms was described in details in Section 3.2.

3.2. OCT image pre-processing

Next sections are based on our paper, published in 2018 [1]

Lumen segmentation is the first but crucial step in the intravascular OCT image analysis process as it allows for detection of stenosis and plaques of high risk. The proposed algorithm for automated lumen detection in intracoronary optical coherence tomography images has been implemented in Matlab software using the Image Processing Toolbox and showed in flowchart in Figure 3-9.

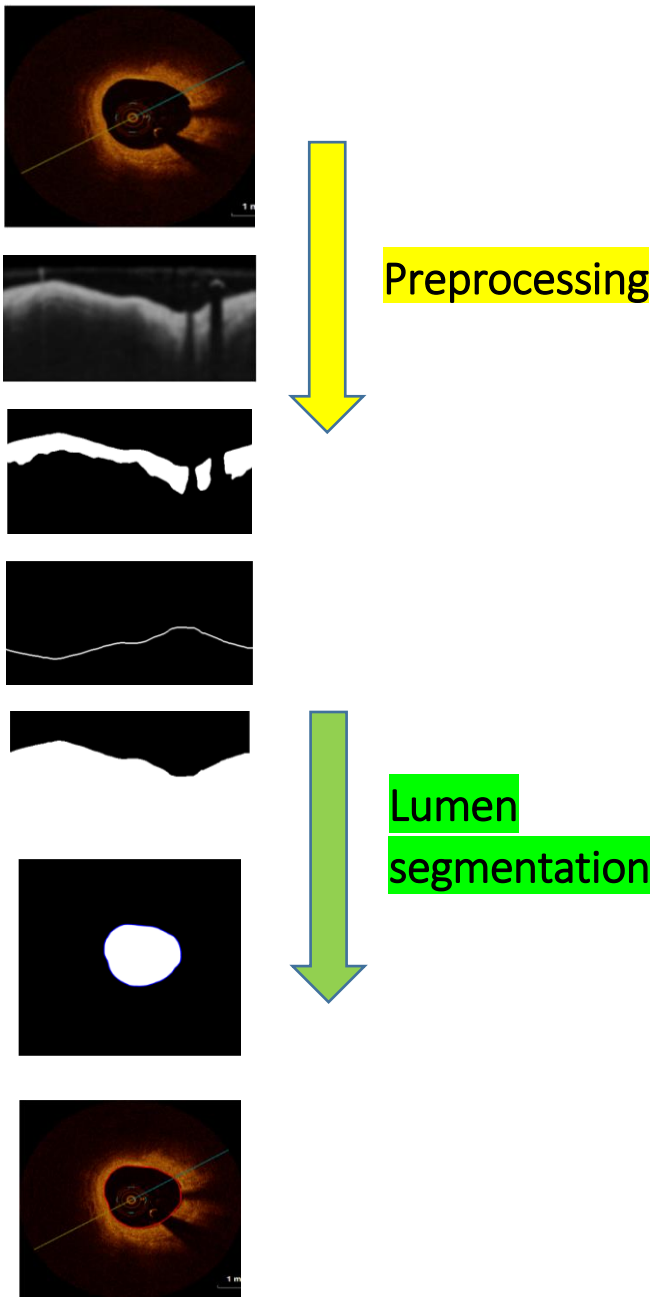

Figure 3-9 Proposed methodology for lumen contour detection

Materials

The analyzed material was composed of 667 frames of different patients, from the Medical University of Silesia. Images used in this study were acquired by the FD-OCT system (C7-XR system OCT Intravascular Imaging System, Westford, MA) and two kinds of imaging catheters: the C7 Dragonfly and Dragonfly OPTIS catheter both with automatic pullback, drive motor optical controller. The analyzed data was obtained with a pullback speed 20 mm/s and 18 mm/s, respectively.

Intravascular OCT images on the one hand clearly depict the boundaries between lumen and vessel but on the other hand are inhomogeneous.

The images are acquired during a pull-back OCT probe along the coronary artery. The tortuosity of the vessel, type of plaque (especially calcified plaque – hard plaque) are very important factors which determined the quality of the obtained signal. In some rare circumstances the OCT probe may get stuck even though it is flexible. Moreover, due to high probe's flexibility, its position is not in the center of the vessel (Figure 3-10). All these aspects influence the acquired image, consequently the structures, are presented in different way, with different degree of intensity, shape and orietntation. Furthermore the OCT images contain extraneous artifacts, such as bright concentric circular rings, and a bright structure from the guide wire with a characteristic shadow behind it. These types of artifacts appear in almost every frame which makes the advanced image analysis steps impossible.

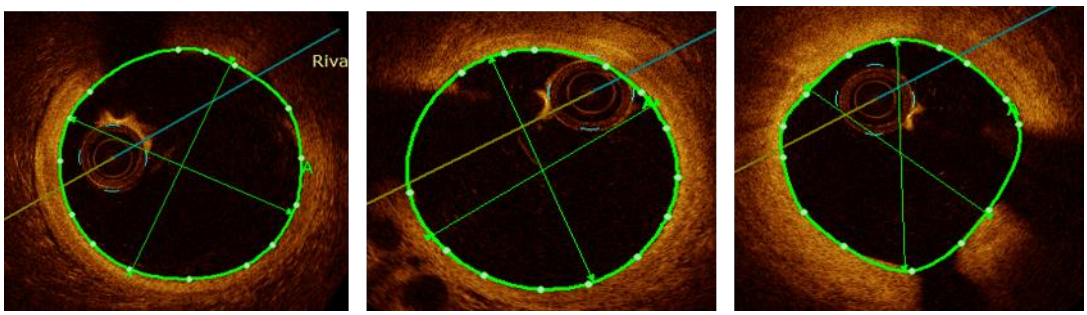

Figure 3-10 Probe position along the OCT pullback.

Therefore, the preprocessing stage was necessary to obtain a binary image of intimal layer (the most inner layer of three layers building the vessel wall) without artifacts from diagnostic catheter and improve the quality of the image for further analysis.

The proposed algorithm receives as an input each consecutive frame from the whole OCT image dataset. Multi-frame images have been saved in DICOM format (pullback run) and each frame is a 2D RGB image in the Cartesian coordinate system.

Firstly, all calibration markers and text remarks are removed from the image using a mask of the pixels that are colored (Figure 3-11). The analyzed RGB image is converted into grayscale with the NTSC 1953 standard, which converts RGB values to grayscale values by forming a weighted sum of the R, G, and B components:

$$I\_grayscale = 0.2989 * R + 0.5870 * G + 0.1140 * B \qquad (3\text{-}3)$$

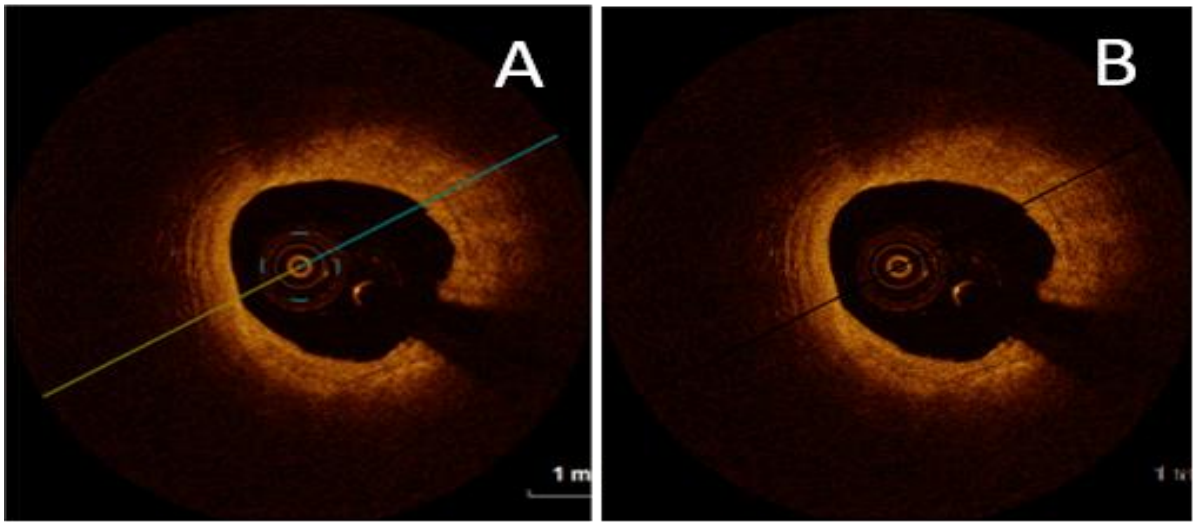

Figure 3-11 Removed calibration markers

After converting the RGB image to grayscale image, the polar transform was applied and further preprocessing stages were being performed in polar coordinates. The center of the OCT image was chosen as a center of polar transformation .This transformation allowed to convert the circular shape of the coronary artery visible in a cross sectional view to a straightened structure (Figure 3-12) .

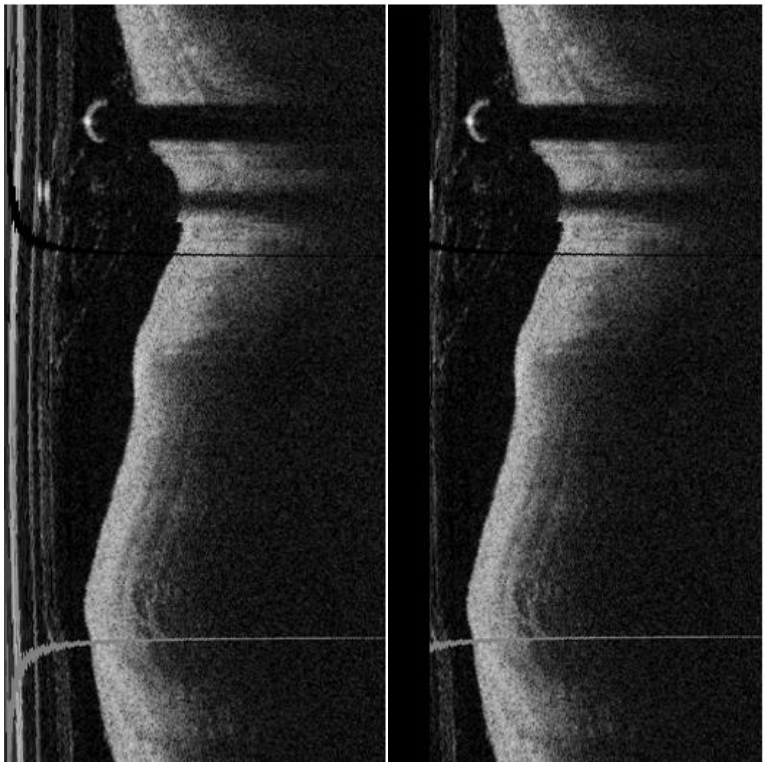

Figure 3-12 OCT image in polar coordinates. On the left side before catheter removal, on the right masked catheter

The polar coordinate system is a two-dimensional coordinate system in which each point on a plane is determined by a distance from a reference point and an angle from a reference direction. The Cartesian coordinates *x* and *y* are converted to polar coordinates *r* and θ with r ≥ 0 and θ is in the interval (−π, π] using following equations[38]

$$theta = atan2(y, x) \tag{3-4}$$

$$rho = sqrt(x^2 + y^2) \tag{3-5}$$

where the atan2 operator is defined as:

$$atan2(y,x)\begin{cases} arctan\left(\frac{y}{x}\right) & if\ x > 0 \\ arctan\left(\frac{y}{x}\right) + \pi & if\ x < 0\ and\ y \geq 0 \\ arctan\left(\frac{y}{x}\right) - \pi & if\ x < 0\ and\ y < 0 \\ +\frac{\pi}{2} & if\ \ x = 0\ and\ y > 0 \\ -\frac{\pi}{2} & if\ x = 0\ and\ y < 0 \\ undefined & if\ x = 0\ and\ y = 0 \end{cases} \tag{3-6}$$

The ring shape distortion from imaging catheter in polar space are shown as the straightened structure on the left side of the image (Figure 3-12) with the known size - Dragonfly catheter diameter is 2.7 French which gives 0.91 mm. Using the knowledge about spatial resolution of

the image and catheter diameter, the region of structure was calculated and next removed from the image (Figure 3.2-4). Another significant artifact, which may limit the segmentation process was a speckle noise from blood not diluted sufficiently. Speckle noise may affect the lumen segmentation outcome by misclassifying it as a tissue, what results in underestimated value of real lumen area.

In order to remove any destructive speckle effects without damaging the borders a median filter with a 5×5 window [102] was used. After median filtering the Gaussian smoothing operator was used to 'blur' the image, to remove unnecessary details, to reduce noise from the background (Figure 3-13), to provide gentler smoothing and to preserve the sharper edges.

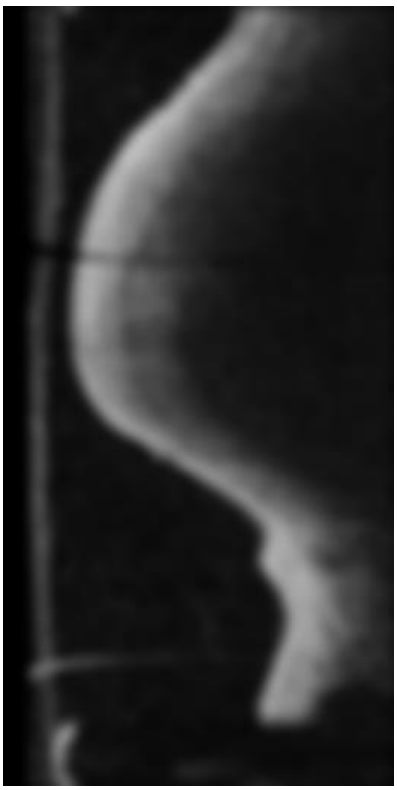

Figure 3-13 Results after Gaussian filtering

An automatic thresholding in the polar space was used to generate a new binary image with clearly separated region with high gradient –corresponding to the intimal layer (Figure 3-14) .

Figure 3-14 Binary Image with clearly delineated intimal layer

3.3. Lumen segmentation in OCT image

Because of image complexity there is no perfect method to segment all of the medical structures with high efficiency. However, the success of the lumen segmentation step is crucial for the further analysis of OCT images and correct diagnosis.

The outcome of the preprocessing stage was a binary image with the primary segmented area that still contains small artifacts like insufficiently diluted blood close to imaging catheter (Figure 3-14). The morphological opening and closing operations were applied to minimize the effect of artifacts. While erosion and dilation have the major disadvantage of changing the size of the region of interest, opening and closing retain the interesting area. Based on the lumen shape a disk-shaped structuring element was used.. The disk-shape element is a flat, structuring element, where R specifies the radius (Figure 3-15).

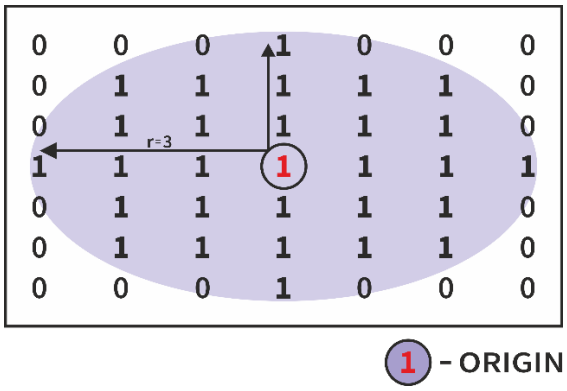

Figure 3-15 Illustration of a flat structuring element [45]

The radius was determined experimentally and set to 5. Figure 3-16 shows examples of the results of morphological opening and closing operations.

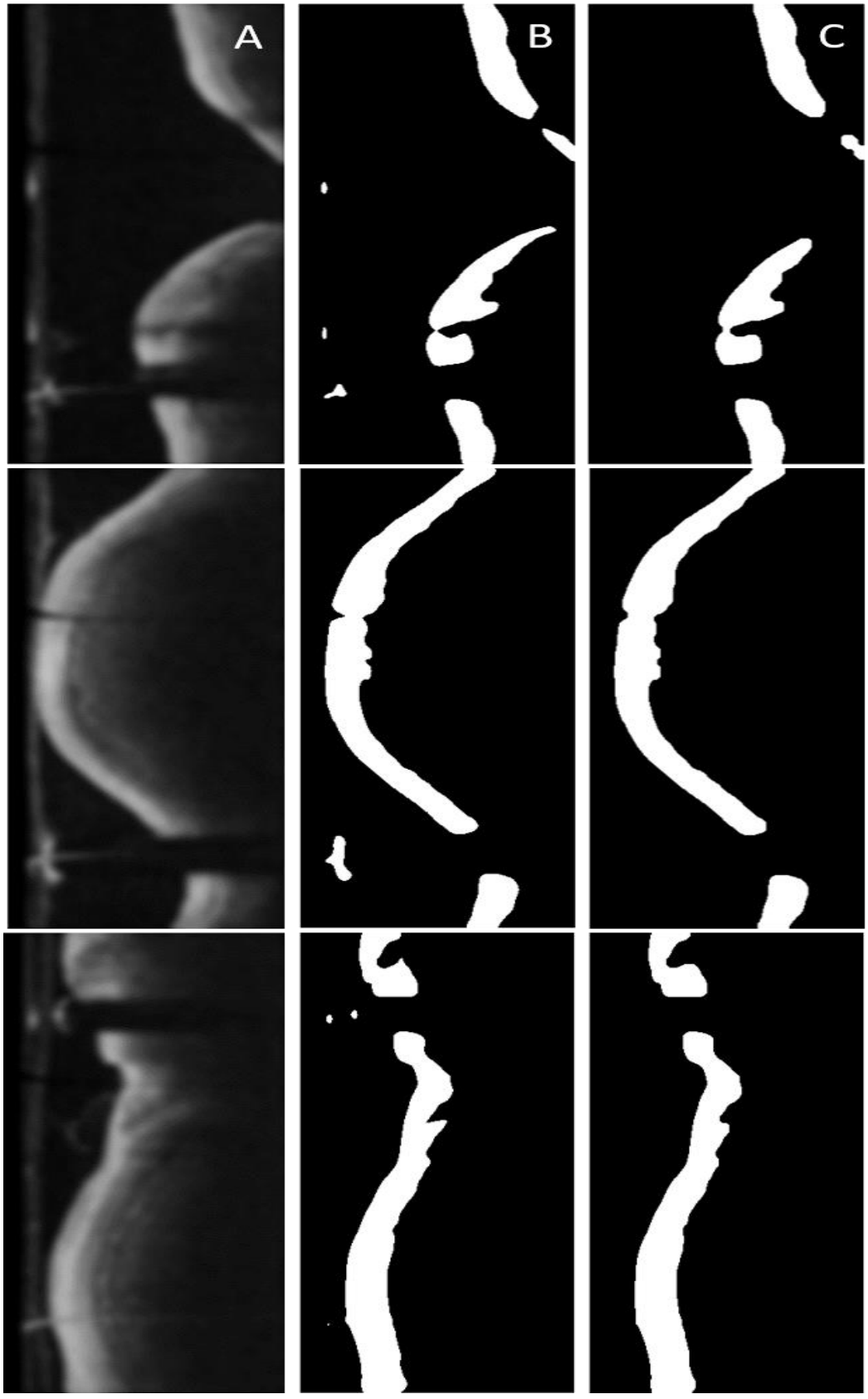

Figure 3-16 Examples of results after morphological opening and closing operations on OCT images in polar coordinates: a) images after Gaussian filtering, b) images after binarization, and c)images after morphological opening and closing operations. (modyfied from [1]).

Artifacts from the imaging catheter and the guide wire were removed in preprocessing stage. However, the shadow from guide wire makes the intimal layer discontinuities what can be observed in Figure 3-16 C. A similar effect was caused by bifurcations. The gap from guide wire shadow was usually of the same size, regular and easily to be found and filled. More problematic were gaps caused by bifurcations which can vary in size and additionally, the remaining objects of the segmented lumen may have irregular shapes. Bifurcation results in lumen area distortion which can be observed in Figure 3-19 D.

The interpolation of remaining regions was necessary to draw the final lumen contour which should be as close as possible to the expected values. To solve this problem modified version of linear interpolation was applied. This operation is needed to measure lumen diameter in place where in the place where the vessel is branching.

In order to connect the parts of lumen the boundary information as location and coordinates of every disconnected part of intima layer (traces of the exterior boundaries of the object) were analyzed. A cell array of boundary pixels coordinates of all of the objects in the binary image [49] was created. To perform the linear interpolation extreme points were calculated as presented in Figure Figure 3-17

Figure 3-17 Illustration of marked extremes for two different regions[45] [1].

Few of the extrema points were candidates to the contour points including bottom-left, top-left and top-right. The objects were analyzed started from the top to the bottom.

There were several scenarios to choose the interpolation points (Figure 3-18):

1) the left – bottom point from the first, upper object and the top-left from the second object which was located below

2) the right – bottom point from the first, upper object and the top-left from the second object which was located below

3) the left – bottom point from the first, upper object and the top-right from the second object which was located below

4) the right – bottom point from the first, upper object and the top-right from the second object which was located below

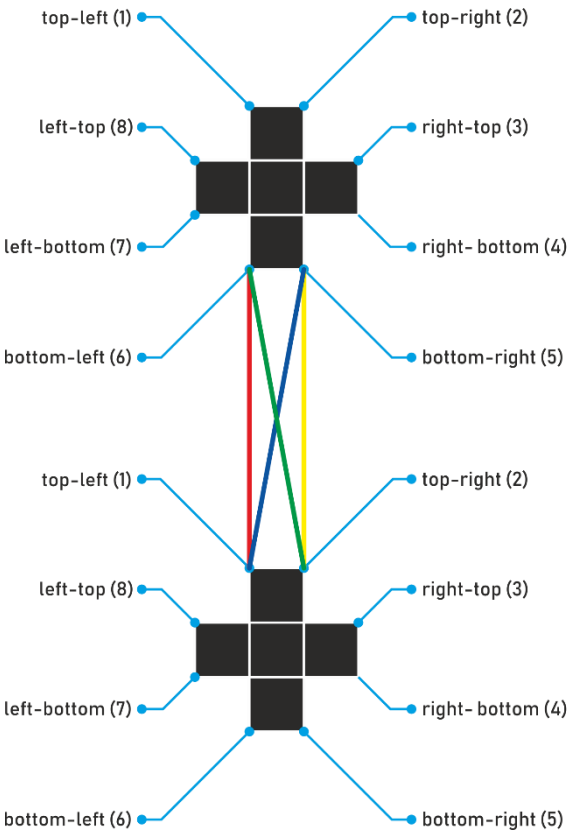

Figure 3-18 Proposition of candidates to the contour points. Red – first scenario, Green – third scenario, Blue – second scenario, orange the fourth scenario.

The final choice was determined by the value of Euclidean distance between extremes. The bigger the bifurcation is, the longer will be the distance. The individual extremes coordinates were taken to calculate the distance and perform linear interpolation. Bifurcations with diameter > 2 mm are a big vessels, clinically important and causing a long gap in the lumen contour. Therefore the cut off point for bifurcation was set 2 mm size. Figure 3-19 presents some examples of chosen contour points. To avoid sharp contour reconstructions additional points have been chosen by moving up and down from extreme points and finding the first white pixel in the current row.

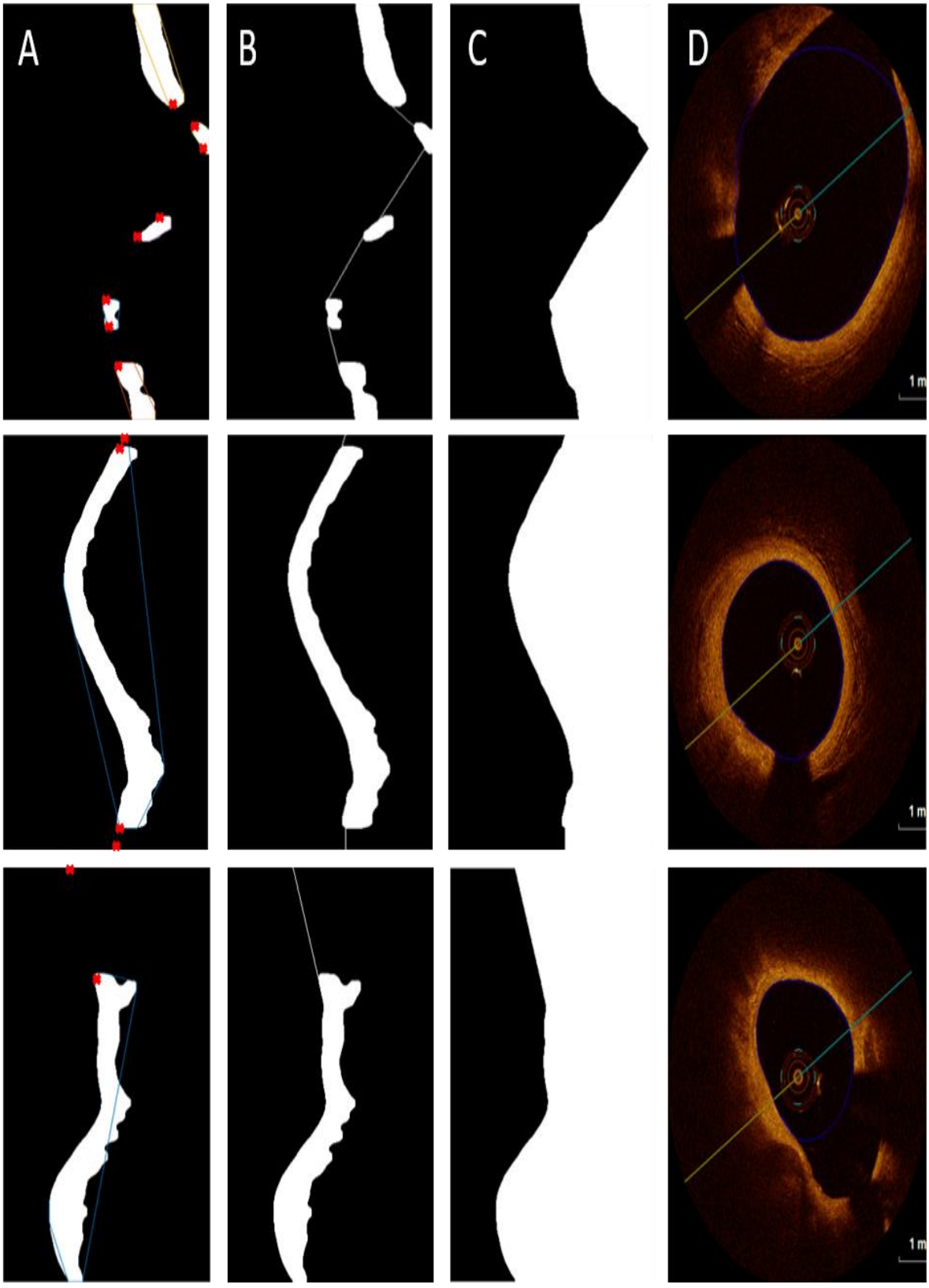

Figure 3-19 Examples of chosen extrema points needded to perform linear interpolation: a) binary image after preprocessing and artifact removal with marked extremas, b) extrema point connection (linear interpolation), c) lumen segmentation outcome d) input OCT image with lumen contour tracing. Images a-c are in polar coordinates, image d is after transformation to Cartesian coordinates.(Modyfied from[1]).

After setting the contour points, a linear interpolation was used. In that way all discontinuities coming from bifurcations, the guide wire and from artifacts were filled. With use of this method, the lumen border line in the polar image was obtained (Figure 3.3-6). Finally, the lumen border points were detected by the Sobel edge detection algorithm [103]. The Sobel operator performs a 2-D spatial gradient measurement and emphasizes regions of high spatial frequency that correspond to edges.

3.4. Image post-processing and outcomes

The resulting polar image was transformed back to Cartesian coordinates. The polar coordinates *r* and ϕ are converted to the Cartesian coordinates *x* and *y* by using the trigonometric functions sine and cosine:

$$x = r * cos(\theta) \qquad (3\text{-}7)$$

$$y = r * sin(\theta) \qquad (3\text{-}8)$$

As the segmentation outcome, the resulting contour did not have the smoothness that the vessel is expected to have. The Savitzky-Golay sliding polynomial filter with window width 35 and polynomial order 2 [104] was being applied.

Savitzky and Golay showed that a set of integers $(A_{-n}, A_{-(n-1)} \ldots, A_{n-1}, A_n)$ could be derived and used as weighting coefficients to carry out the smoothing operation [105]. The use of these weighting coefficients, known as convolution integers, are exactly equivalent to fitting the data to a polynomial. Therefore, the smoothed data point $(y_k)_s$ by the Savitzky-Golay algorithm is given by the following equation:

$$(y_k)_s = \frac{\sum_{i=-n}^{n} A_i y_{k+1}}{\sum_{i=-n}^{n} A_i} \qquad (3\text{-}9)$$

where A_i are weighting coefficients to perform the smoothing operation

Figure 3-20 shows each step of lumen segmentation.

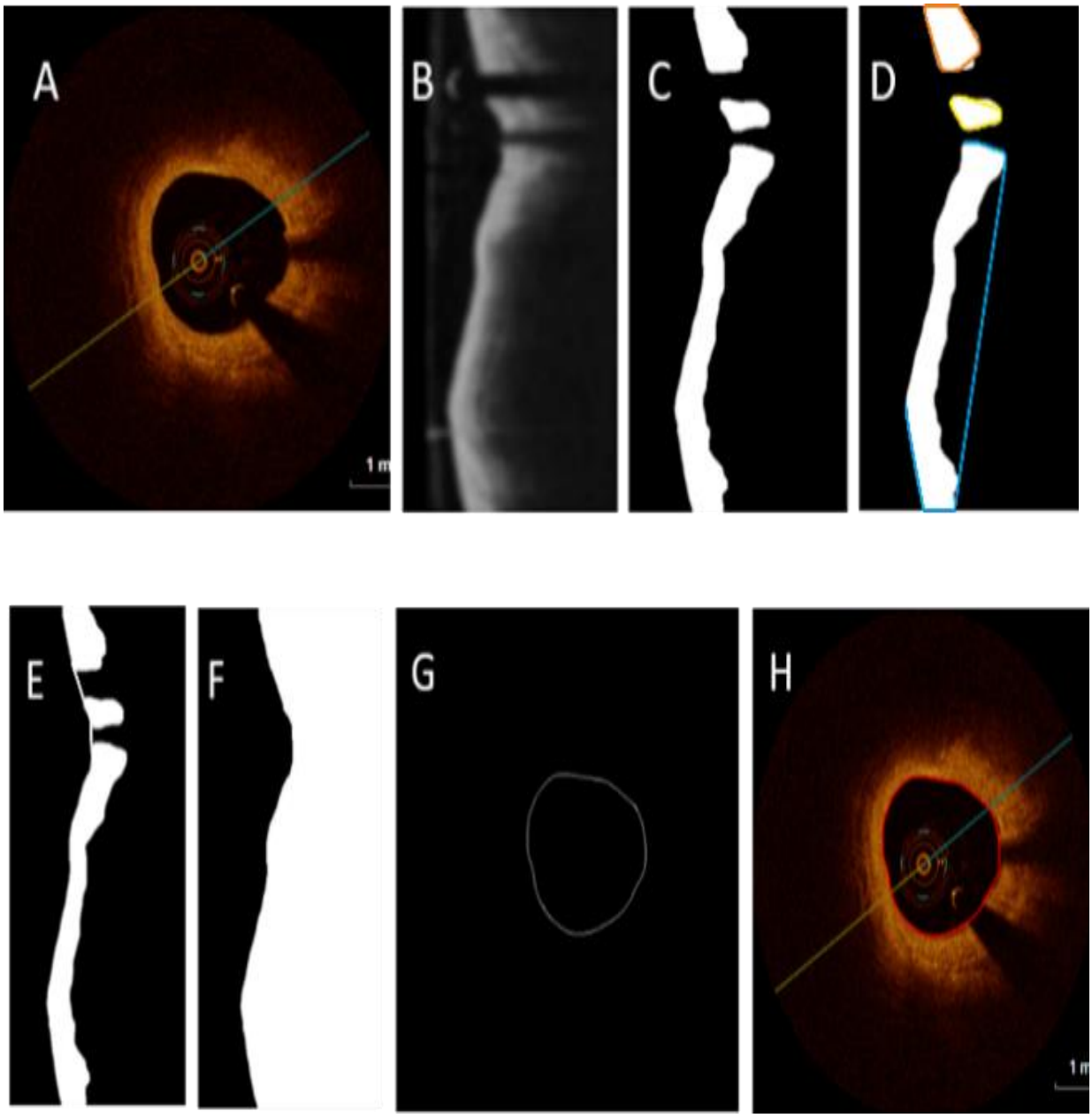

Figure 3-20 Lumen segmentation steps: a) original image in Cartesian coordinates, b) image after transformation to polar coordinates and after catheter removal applying Gaussian filtering, c) image in polar coordinates after binarization and morphological operations. Small artifacts are removed and small gaps filled, d) Image in polar coordinates with marked extremas, e) based on extrema, connection points are chosen and linear interpolation is applied to fill all gaps, f) lumen segmentation outcomes g) segmented contour transformed back to Cartesian coordinates and after smoothing filter, h) final image, cross-sectional view with marked contour (Modyfied from. [1])

3.5. Results and statistics

The validation of the described fully automated lumen segmentation method has been performed on 667 intravascular optical coherence tomography frames from different patients. Figure 3-21presents the achieved results.

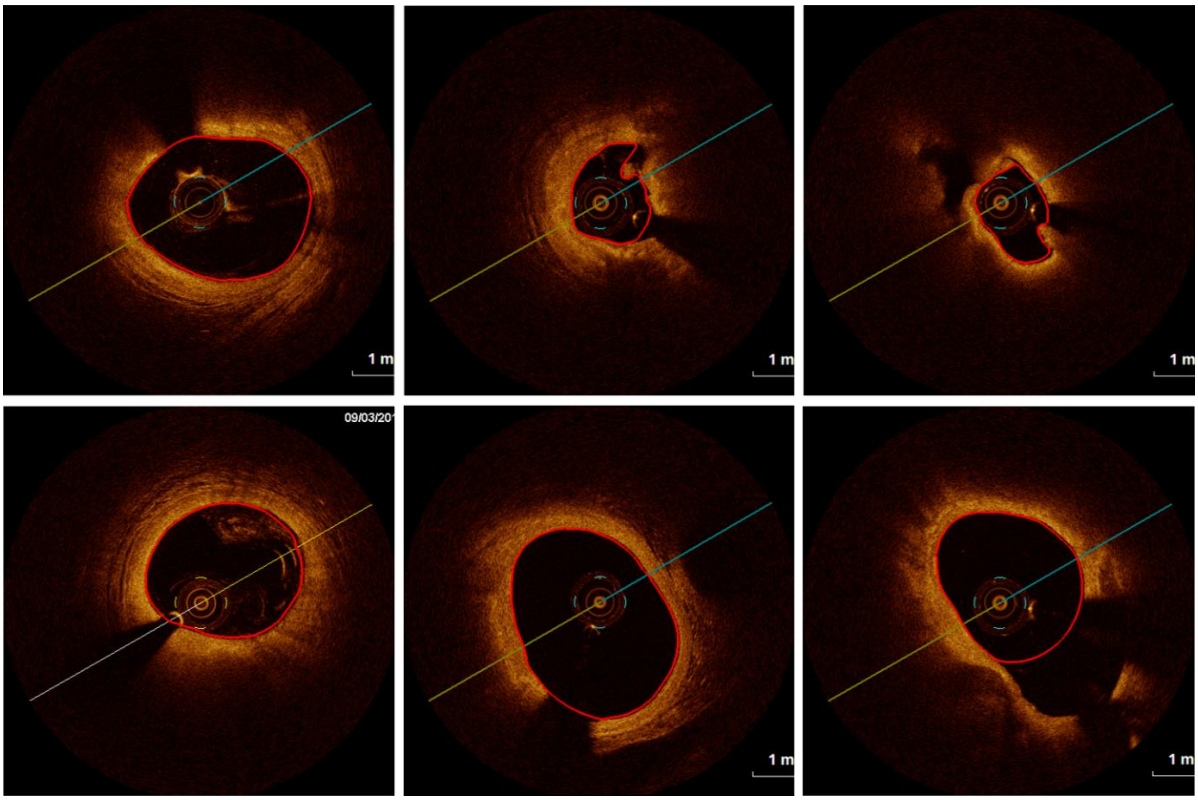

Figure 3-21 Results of the described lumen segmentation algorithm dedicated for OCT images. Presented images show six different cases including various artifacts and difficulties (modified from[1]) .

Statistical analysis includes data obtained from four methods:

1) the proposed algorithm,
2) two commercially available systems (St. Jude Medical system and Medis medical imaging systems),
3) a manual analysis (ground-truth mask).

Continuous parameters were reported as the mean and median values with the first and the third quartiles (Q1 – 25%, Q3 – 75%). The Bland – Altman analysis was used to assess the agreement between two measurement methods. It is a comparison technique proposed by Altman and Bland [106] based on the quantification of the agreement between two quantitative measurements by studying the mean difference and constructing limits of agreement.

Results for the particular measurements were presented as the mean value with 95% confidence interval (CI) and as the median with the first and the third quartiles. Discrepancies between the first and the second analysis were calculated as absolute and relative differences and presented as mean values with 95% CIs. Intraclass correlations (ICC) were calculated as the main measure of agreement along with the graphical representation as Bland-Altman plots. Analyses for statistical computing were performed in R language (R Core Team 2017, Vienna, Austria).

Validation of automated lumen segmentation

In order to validate the described algorithm, I compared four lumen detection methods: the proposed solution, the ground-truth mask, and two commercially available systems including St. Jude Medical system (system 1) and Medis medical imaging systems (system 2). Manual segmentation was performed by independent observers - interventional cardiologists with reference-grade clinical experience.

Following parameters have been analyzed for each of the described methods: the lumen area, the mean lumen diameter, the minimal lumen diameter and the maximal lumen diameter. Results are collected in Table 3-4.

Table 3-4 Calculated parameters for each of the analyzed methods. (Modyfied from [1])

	Proposed method mean	System 1 mean	System 2 mean	Ground -truth mean
Lumen area [mm^2]	5.99	6.04	5.76	5.89
Mean lumen diameter [mm]	2.72	2.72	2.66	2.68
Minimal lumen diameter [mm]	2.52	2.52	2.42	2.49
Maximal lumen diameter [mm]	2.91	2.93	2.87	2.88

The results of assessed parameters were collected in Table 3-5, Table 3-6, Table 3-7 and presented in Bland-Altman plots, where the solid line denotes the mean difference between the first and the second measurement, while the dashed line indicates ±1.96 standard deviation.

To enable the analysis of statistical data, following parameters have been collected additionally:

The relative difference is calculated using the following equation:

$$RD = \frac{\sum_{i=1}^{N} \frac{I_i - O_i}{max(O_i, I_i)}}{N} * 100\% \qquad (3\text{-}10)$$

The absolute relative difference is calculated using:

$$ARD = \frac{\sum_{i=1}^{N} \frac{|I_i - O_i|}{max(O_i, I_i)}}{N} * 100\% \qquad (3\text{-}11)$$

where

$$N - total\ number\ of\ frames$$
$$i - number\ of\ current\ frame$$
$$O_i - value\ for\ 1st\ measurement$$
$$I_i - value\ for\ 2nd\ measurement$$

Table 3-5 Statistical comparison of parameters between proposed methodology and manual analyses by Analyst (ground-truth). (Modyfied from [1])

	Our method (First measure) mean (CI)	Ground - truth (Second measure) mean (CI)	Our method (First measure) median (IQR)	Ground-truth (Second measure) median (IQR)	Difference	Relative difference [%]	ICC (95% CI)	ICC p-value
Lumen area [mm^2]	5.99 (5.83 - 6.14)	5.89 (5.74 - 6.04)	6.45 (4.72 - 7.67)	6.29 (4.67 - 7.50)	0.10 (0.06 - 0.13)	-1.12 (-1.55 - -0.68)	0,97 (0.97 – 0.98)	< 0.0001
Mean lumen diameter [mm]	2.72 (2.68 - 2.76)	2.68 (2.64 - 2.72)	2.88 (2.41 - 3.13)	2.82 (2.43 - 3.09)	0.03 (0.02 - 0.04)	-1.15 (-1.48 - -0.83)	0,96 (0.95 – 0.97)	< 0.0001
Minimal lumen diameter [mm]	2.52 (2.48 - 2.56)	2.49 (2.45 - 2.53)	2.64 (2.18 - 2.96)	2.61 (2.10 - 2.93)	0.03 (0.02 - 0.03)	-1.11 (-1.44 - -0.78)	0,98 (0.98 – 0.98)	< 0.0001
Maximal lumen diameter [mm]	2.91 (2.87 - 2.96)	2.88 (2.84 - 2.92)	3.07 (2.54 - 3.30)	3.01 (2.58 - 3.25)	0.04 (0.02 - 0.05)	-0.81 (-1.23 - -0.39)	0,91 (0.89– 0.92)	< 0.0001

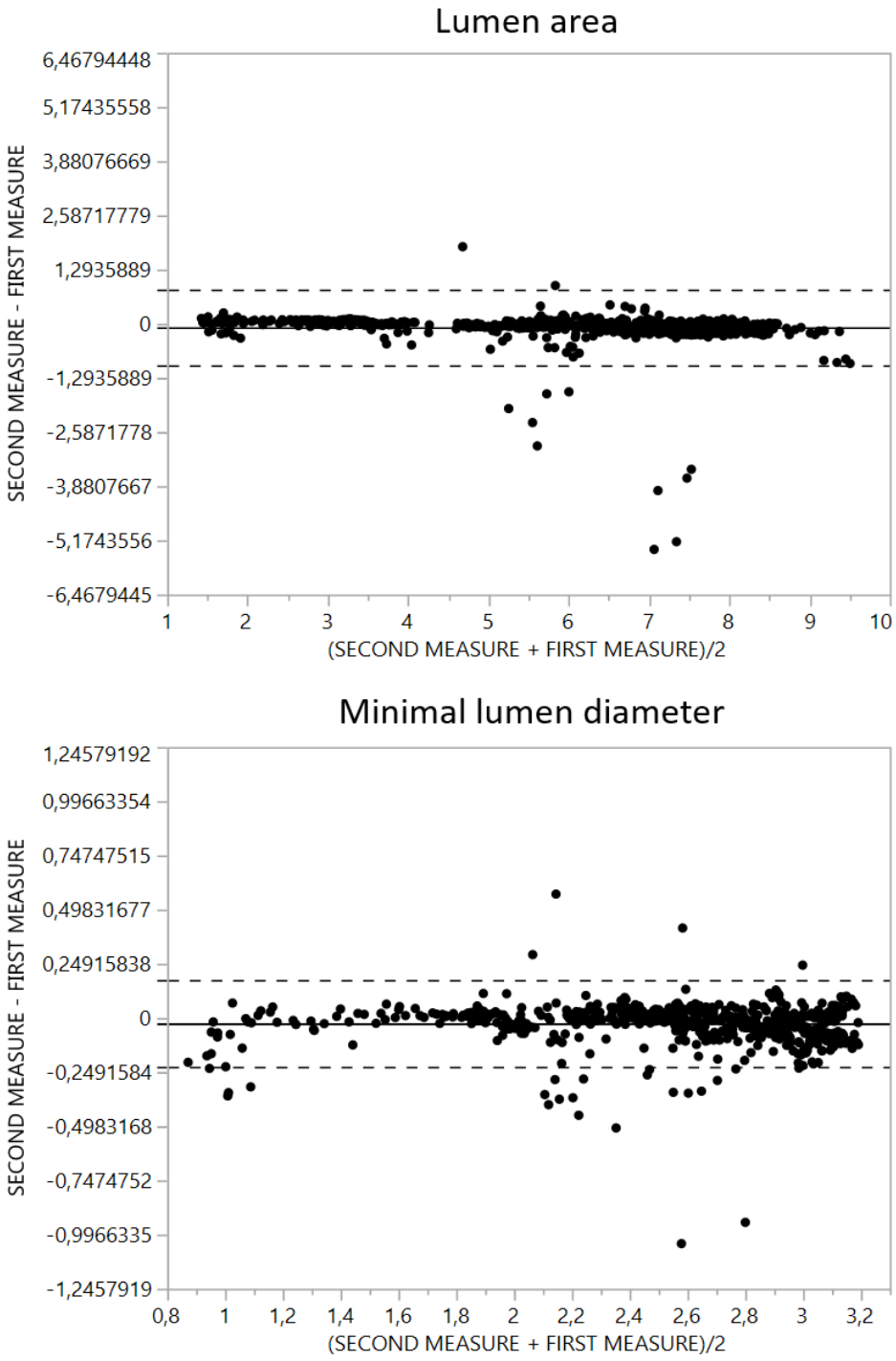

Figure 3-22 Bland-Altman plot for lumen area, minimal lumen proposed method and ground-truth method.

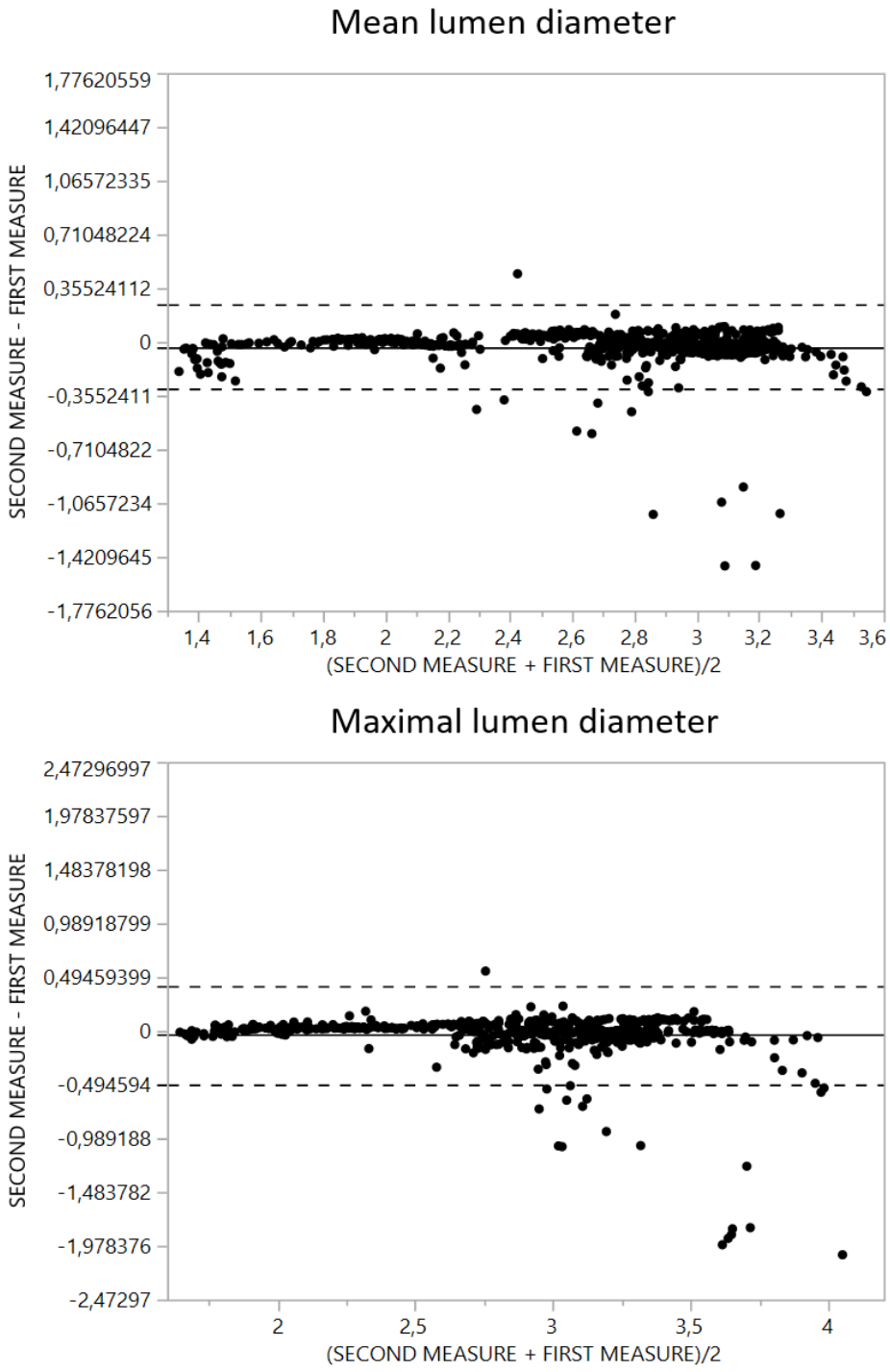

Figure 3-23 Bland-Altman plot minimal lumen diameter and maximal lumen diameter between proposed method and ground-truth method.

Table 3-6 Statistical comparison of parameters between proposed methodology and commercially available System 1 . (Modyfied from [1])

	Our method (First measure) mean (CI)	System 1 (Second measure) mean (CI)	Our method (First measure) median (IQR)	System 1 (Second measure) median (IQR)	Difference	Relative difference [%]	ICC (95% CI)	ICC p-value
Lumen area [mm^2]	5.99 (5.83 - 6.14)	6.04 (5.90 - 6.19)	6.45 (4.72 - 7.67)	6.50 (5.01 - 7.56)	-0.06 (-0.08 – -0.03)	1.67 (1.25 - 2.10)	0,99 (0,98-0,99)	< 0.0001
Mean lumen diameter [mm]	2.72 (2.68 - 2.76)	2.72 (2.68 - 2.76)	2.88 (2.41 - 3.13)	2.87 (2.52 - 3.10)	-0.00 (-0.01 - 0.00)	0.34 (0.06 - 0.63)	0,98 (0.97– 0.98)	< 0.0001
Minimal lumen diameter [mm]	2.52 (2.48 - 2.56)	2.52 (2.48 - 2.56)	2.64 (2.18 - 2.96)	2.52 (2.48 - 2.56)	0.00 (-0.01 - 0.01)	0.16 (-0.16 - 0.49)	0,98 (0.97– 0.98)	< 0.0001
Maximal lumen diameter [mm]	2.91 (2.87 - 2.96)	2.93 (2.89 - 2.97)	3.07 (2.54 - 3.30)	3.08 (2.66 - 3.28)	-0.02 (-0.03 - -0.00)	0.82 (0.43 - 1.21)	0,94 (0.93– 0.95)	< 0.0001

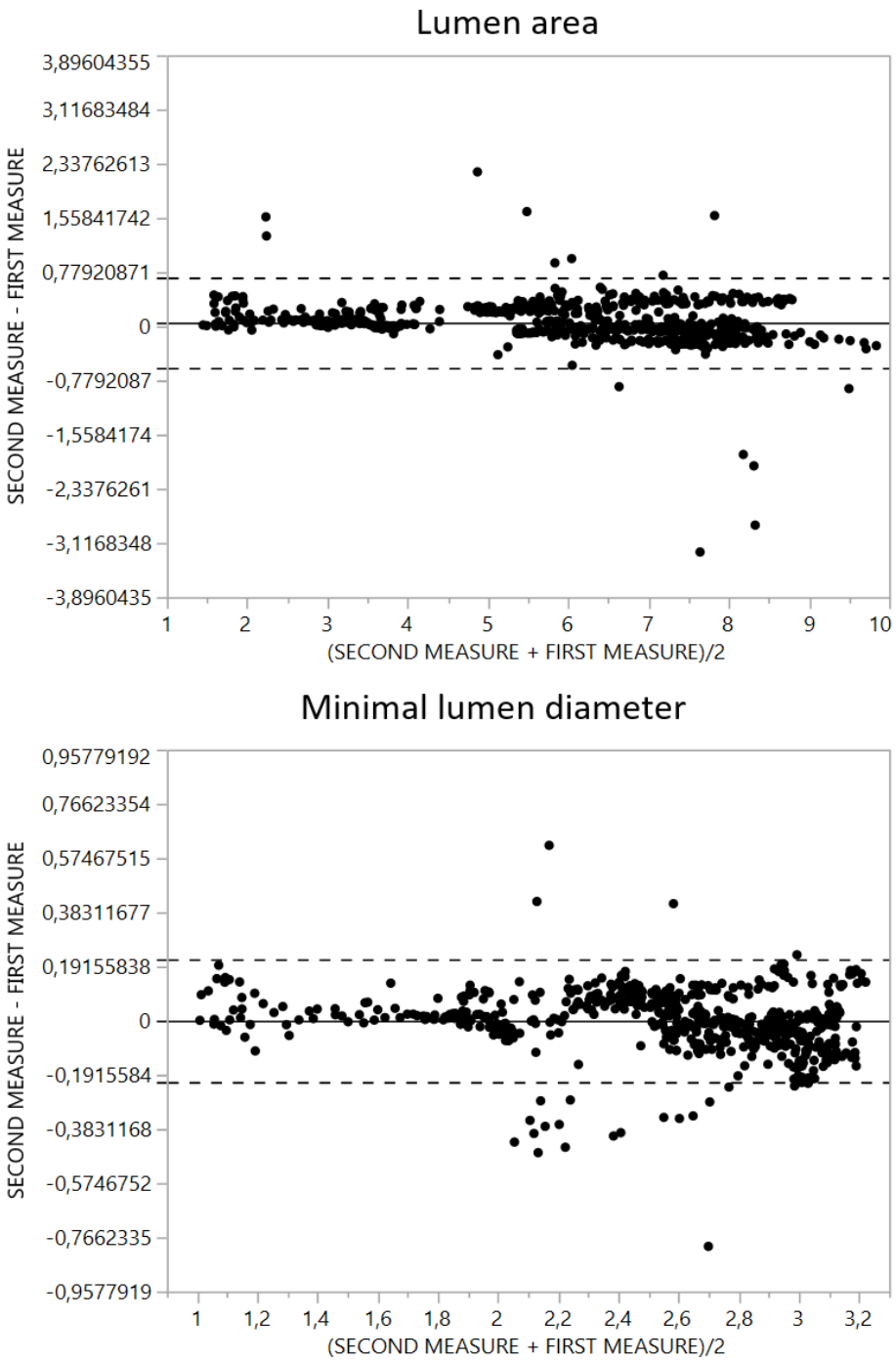

Figure3-24 Bland-Altman plot for lumen area, , minimal lumen diameter, between proposed method and automated lumen detection proposed by commercially available System 1 (Modyfied from [1]).

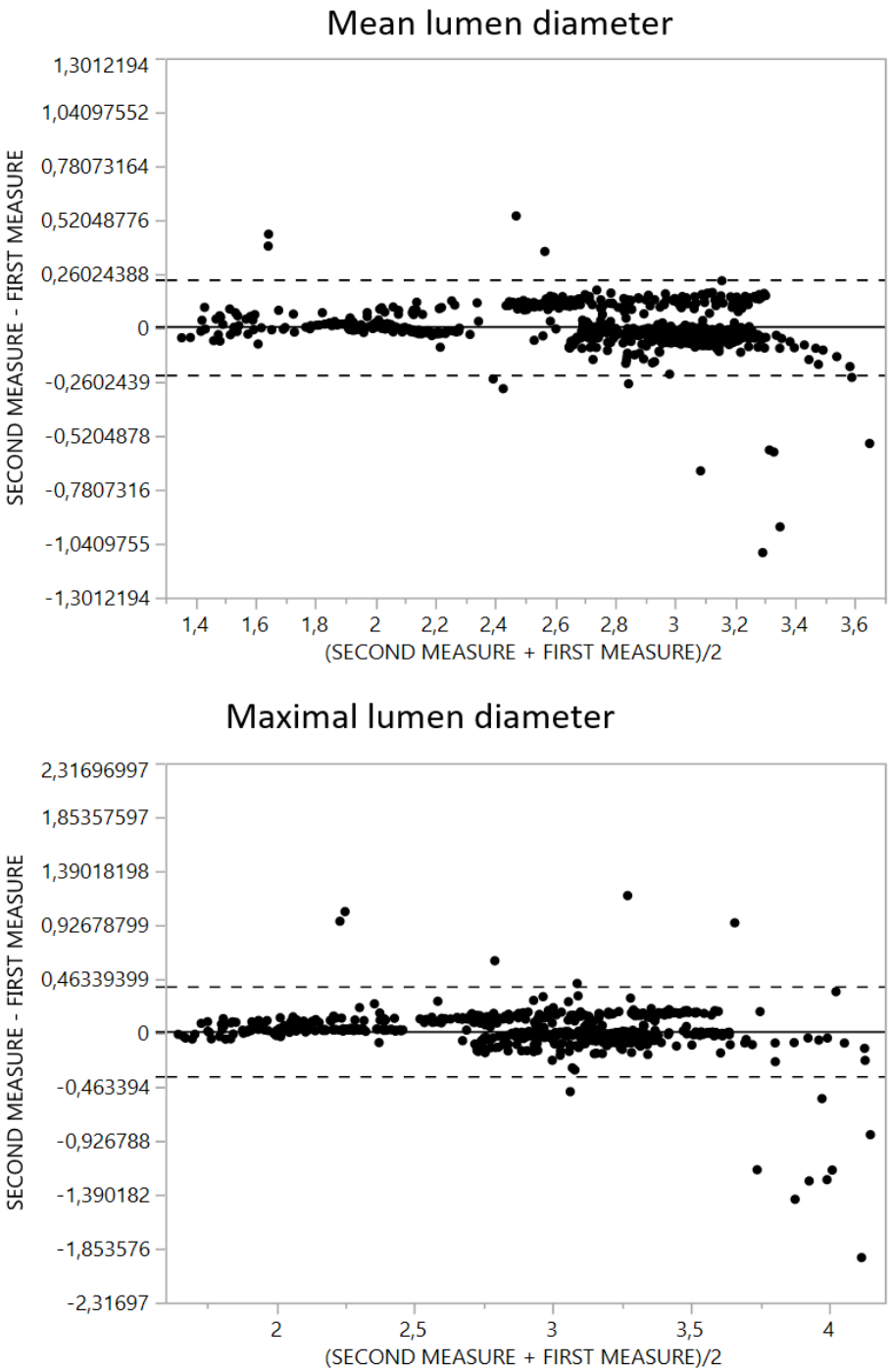

Figure 3-25 Bland-Altman plot for maximal lumen area, mean lumen diameter between proposed method and automated lumen detection proposed by commercially available System(Modyfied from [1]).

Table 3-7 Statistical comparison of parameters between proposed methodology and another commercially available System 2 (Modyfied from [1])

	Our method (First measure) mean (CI)	System 2 (Second measure) mean (CI)	Our method (First measure) median (IQR)	System 2 (Second measure) median (IQR)	Difference	Relative difference [%]	ICC (95% CI)	ICC p-value
Lumen area [mm^2]	5.99 (5.83 - 6.14)	5.76 (5.61 - 5.92)	6.45 (4.72 - 7.67)	6.13 (3.98 - 7.48)	0.22 (0.18 - 0.27)	-4.23 (-4.88 - -3.57)	0,95 (0.93 – 0.97)	< 0.0001
Mean lumen diameter [mm]	2.72 (2.68 - 2.76)	2.66 (2.61 - 2.70)	2.88 (2.41 - 3.13)	2.79 (2.25 - 3.09)	0.06 (0.05 - 0.07)	-2.42 (-2.85 - -1.99)	0,94 (0.92 – 0.96)	< 0.0001
Minimal lumen diameter [mm]	2.52 (2.48 - 2.56)	2.42 (2.37 - 2.46)	2.64 (2.18 - 2.96)	2.56 (2.01 - 2.91)	0.10 (0.09 - 0.12)	-4.96 (-5.53 - -4.39)	0,95 (0.85 – 0.97)	< 0.0001
Maximal lumen diameter [mm]	2.91 (2.87 - 2.96)	2.87 (2.83 - 2.91)	3.07 (2.54 - 3.30)	3.00 (2.50 - 3.26)	0.04 (0.02 - 0.06)	-1.11 (-1.58 - -0.63)	0,89 (0.88 -0.91)	< 0.0001

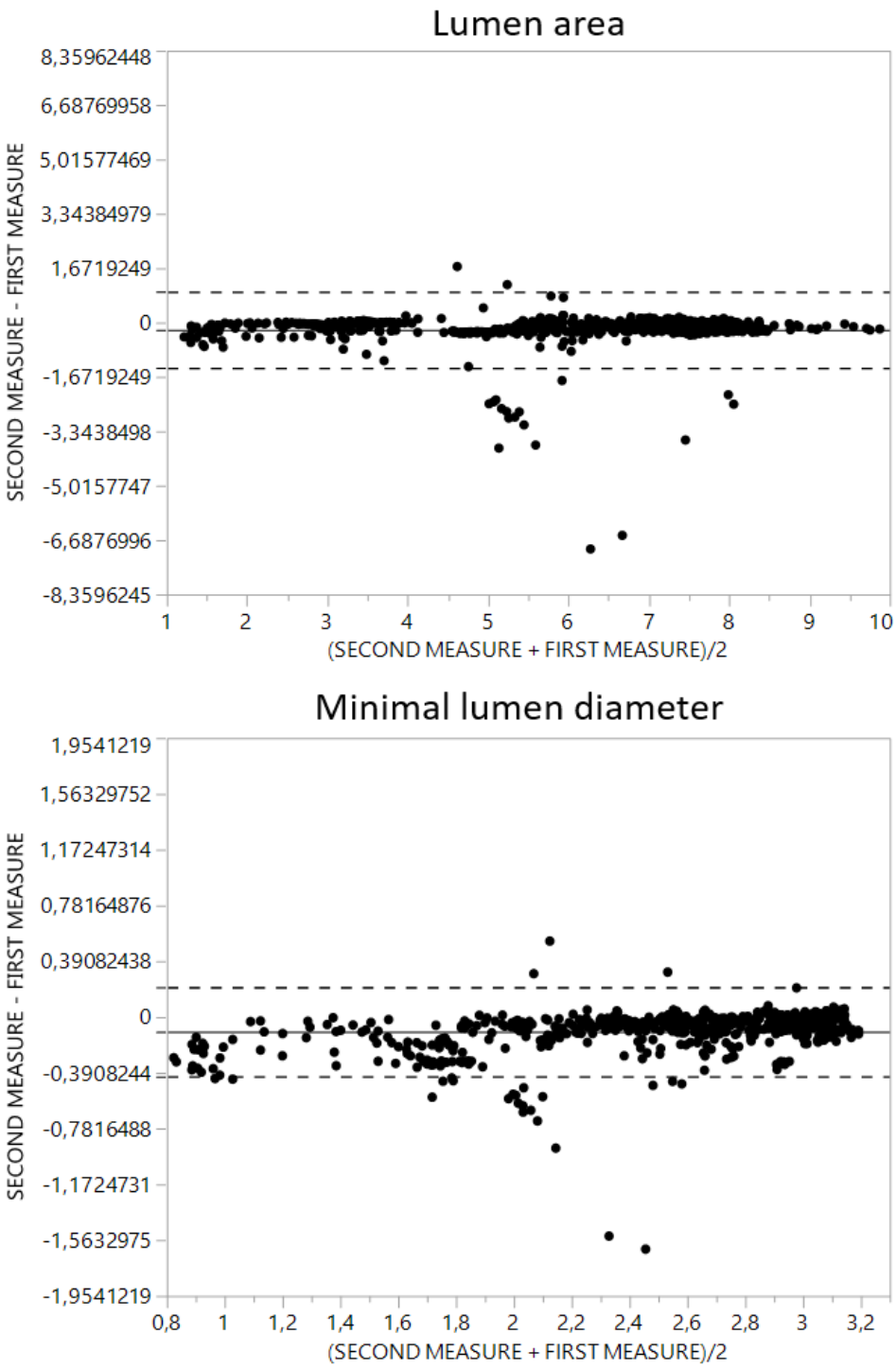

Figure 3-26 Bland-Altman plot for lumen area, minimal lumen diameter between proposed method and automated lumen detection proposed by commercially available System 2 (Modyfied from [1]).

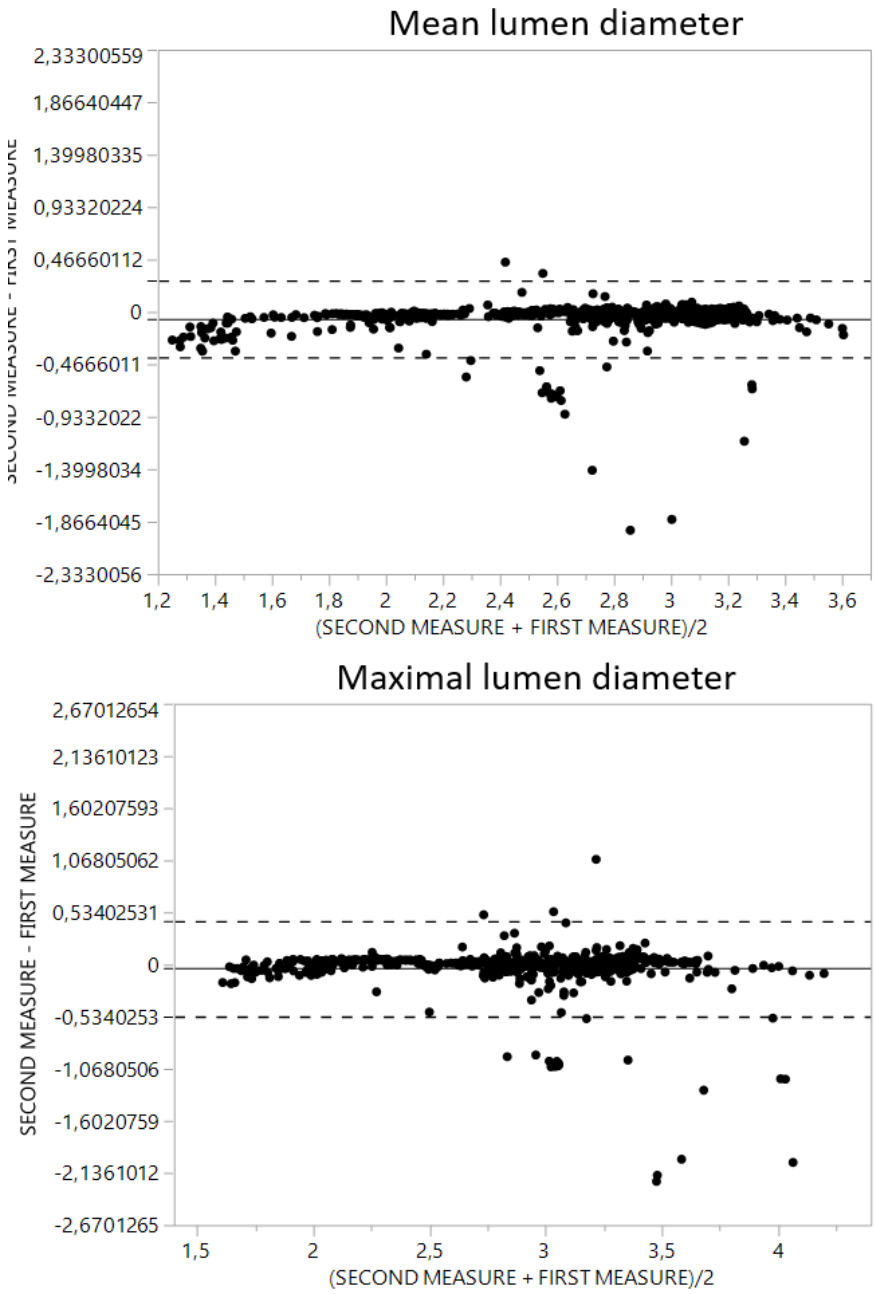

Figure 3-27 Bland-Altman plot for mean lumen area, maximal lumen diameter between proposed method and automated lumen detection proposed by commercially available System 2 (Modyfied from [1])

Summary

The lumen detection was performed on a desktop computer with an Intel Core i5-4200, 1.60 GHz processor, 8 GB RAM, Windows 10 64 bit OS, and Matlab (R2016b). The average time of the lumen contour detection was 1.099 s. The average time of manual segmentation of a slice was approximately 60 seconds (estimated during eye-tracking study – section 3.1) . The

computer-aided segmentation systems was much faster than the manual segmentation, furthermore it was objective to the same cases and also very accurate. To validate the proposed method, the same dataset was tested with the results from manual analyses and two commercially available tools for automatic lumen detection.

We achieved high correlation of automatically determined lumen area with a gold standard – ground–truth method (manual analyses performed by a human expert) – 0.97 ICC. Results in the literature [3] [70] [74] reported an absolute difference of mean lumen area of 0.1 mm^2. De Macedo et al [70] obtained absolute difference of mean lumen area of 0.17 mm^2. Results achieved with the developed method may appear similar to those presented previously published methods (the absolute differences of mean lumen are of 0.1 mm^2) but what is worth to highlight, in our validation process all frames were included to analyses, even frames containing complex plaque, artifacts from residual blood or bifurcations with diameters of over 2 mm. Furthermore, the parameters calculated by the developed method were similar to obtained results from both commercially available systems (System 1 and System 2), however no details on these systems have ever been described in any paper.

The Bland-Altman plots indicate a good agreement between the used methods. Most points plotted are between the solid line (the mean difference) and the dashed line (the mean value ± double standard deviation).

The absolute difference of mean lumen area calculated between the developed method and automated lumen detection proposed by System 1 is of 0.06 mm^2,while in case of System 2, the absolute difference of mean lumen area was equal 0.22 mm^2, Although the lumen areas were similar in all methods and there is a high ICC between the developed method and its competitors (0.95 – 0.99), the lumen diameters were shown with lower ICC, especially between the developed method and System 2.

Conclusion

Proposed fully automated methodology is able to detect and correctly draw lumen contours in OCT images including frames with bifurcations and artifacts from blood. The automated method has been engineered with use of results of eyetracking studies and inherits human-derived interpretation rules. It was validated using the manual analyses performed by an expert as a gold standard as well as commercially available tools. The results suggest that this method

can be a useful tool for vessel segmentation and further analysis. Achieved results indicate that the proposed algorithm fulfills the requirements of clinical use.

The main limitations of the study was that our algorithm was not tested on images with the presence of stents which could have a negative impact on the results. This limitation may be solved in the future by developing methods to extract the struts and fill the artifacts from strut shadows.

CHAPTER 4

4. The NIRS image processing

The purpose of this part of study was to develop a new fully automated method for estimation of lipid burden using the analysis of data from Near Infrared Spectroscopy (NIRS). This new tool should be enriched with new functions regardingNIRS data analysis to solve the problem of lipid core plaque detection on NIRS images. The commercial available systems do not detect lipid pools if there are covered by artifacts - dark areas. This limitation has an impact in assessing the lipid core burden index, which indicate the high risk plaque. The studies has been published in our paper [107].

The proposed method was divided into four processing stages: preprocessing (image enhancement), segmentation of artifacts, detection of lipid areas and calculation of medically important features.

4.1. Pre-processing

Images used in this study were acquired via TVC Imaging SystemTM and TVC InsightTM Catheters, from 31 patients in the Medical Univeristy of Silesia .

The main goal of the preprocessing step was to improve the image quality by reducing, or even removing the unrelated or surplus parts from the NIRS images. In figure Figure 4-1an exemplary chemogram is presented, where red pixels indicate the arterial wall, yellow pixels the presence of lipid regions and black regions (artifacts), the presence of calcifications or the guide-wire. If a pixel does not contain enough data, it appears black [108], where a contiguous black region could be caused by guide-wire shadowing. Also the ability of near-infrared light to penetrate through the calcium could cause “shadowing” on lipid pools, which were covered by calcium [109]. In cases where most of chemograms include black regions, it could be easily suggested that there was a problem with NIRS-IVUS probe during signal acquisition.

Figure 4-1 Chemogram of a stented area with visible artifacts (dark areas) and lipid core plaque (yellow areas (Modyfied from [107]).

At the request of cardiologists from the Medical Univeristy of Silesia we proposed, engineered and tested an algorithm to detect not only the lipid regions, which are clearly visible but also these hidden under artifacts. To achieve this it was proposed to preprocess and analyze each of the RGB image channels. A 24-bit RGB image consists of three 8-bit channels: red, green, and blue. Figure 4-2presents particular channels after converting them to grayscale for the chemogram presented in Figure 4-1.

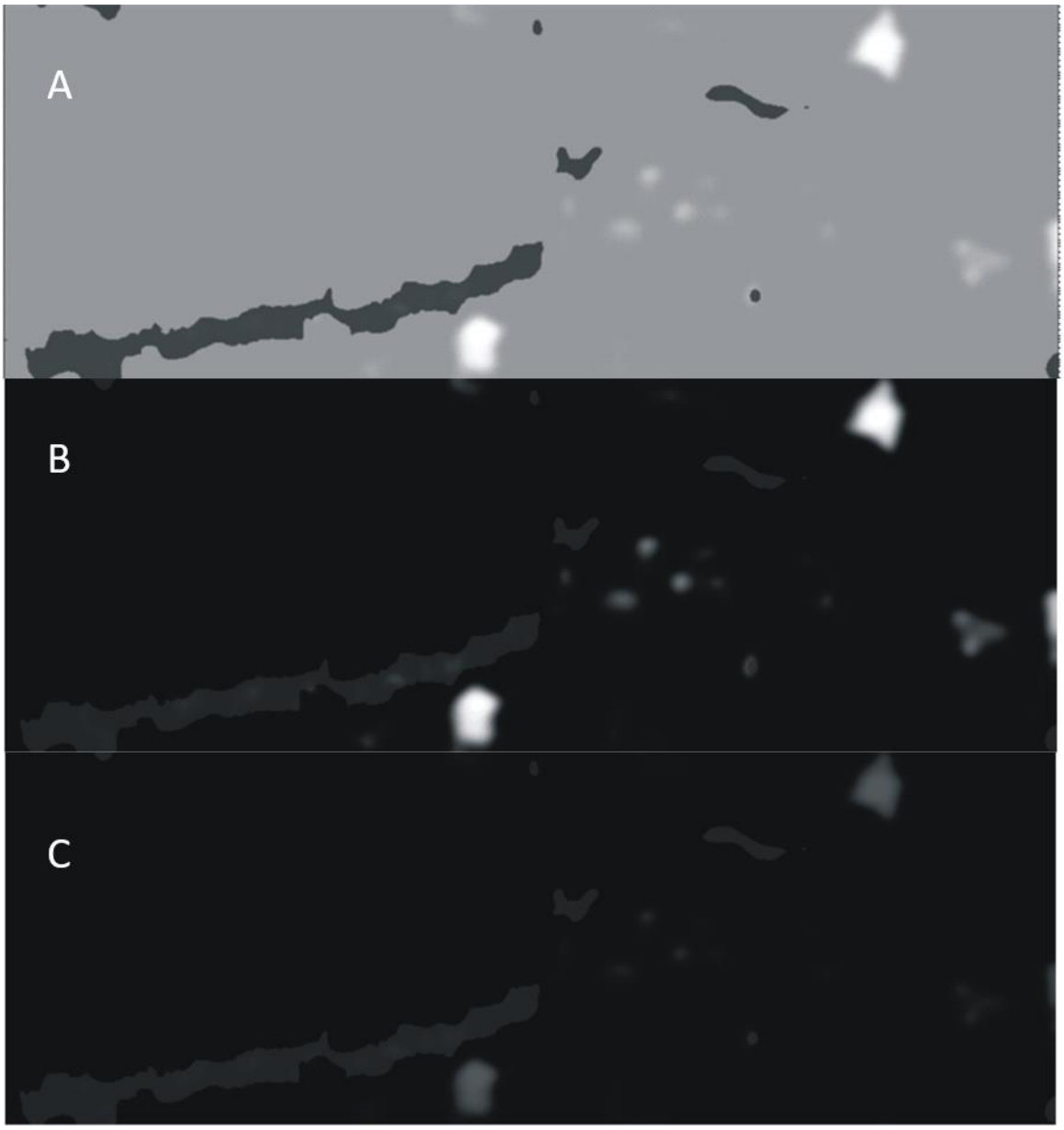

Figure 4-2 RGB channels converted to grayscale for a NIRS image A- red channel - artifacts become clear and visible, B- green channel - lipid areas are more perceptible, C- blue channel. (Modyfied from [107]).

The analysis of the Red channel gives the opportunity to detect the artifacts very precisely, while the processing of the Green channel allows detecting lipid structures, which were not covered by the artifacts. The preprocessing step for each of the channels includes a image intensity adjustment. This step maps the intensity values in grayscale image I to new values in J, such that 1% of data is saturated at low and high intensities of I. This increased the contrast of the output image J.

4.2. Segmentation of artifacts

The segmentation of artifacts was the next step of the proposed algorithm. The detection of these regions was important in terms of segmenting lipid regions that lie under the artifacts. Segmentation of specific regions within an image involves separating an image into regions (or their contours) corresponding to different objects. The regions were segmented by identifying common properties or contours by distinguishing differences between regions (edges).The simplest property that pixels in a region can share is the intensity. Therefore, a natural way to segment such regions was through thresholding, the separation of bright and dark regions. Seeing that the intensity difference between the artifacts and the background as well as lipid regions is high enough, the Otsu thresholding method was proposed. Otsu's method, named after Nobuyuki Otsu, was used to automatically perform clustering-based image thresholding, which means the reduction of a graylevel image to a binary image. Thresholding is one of the widely used methods for image segmentation. It is useful in discriminating the foreground from the background. By selecting an adequate threshold value T, the gray level image can be converted to a binary image. The algorithm assumes that the image contains two classes of pixels following bimodal histogram (foreground pixels and background pixels), then it calculates the optimum threshold separating the two classes, so that their combined spread (intra-class variance) is minimal, or equivalently (because the sum of pair-wise squared distances is constant), so that their inter-class variance is maximal [110]. This step was performed on images gained from the Red channel after the intensity adjustment step. Figure 4-3 shows an exemplary histogram and Figure 4-4 several results of the segmented areas.

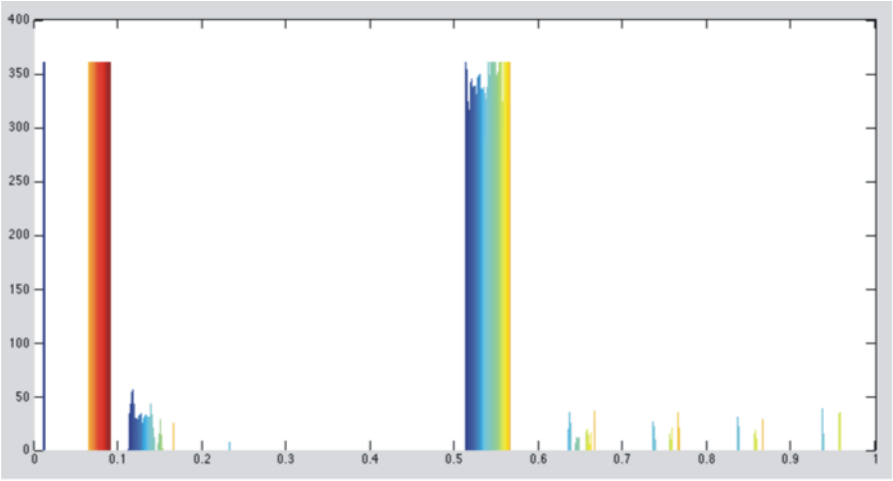

Figure 4-3 Histogram serves to show the idea of applying the Otsu algorithm (Modyfied from [107]).

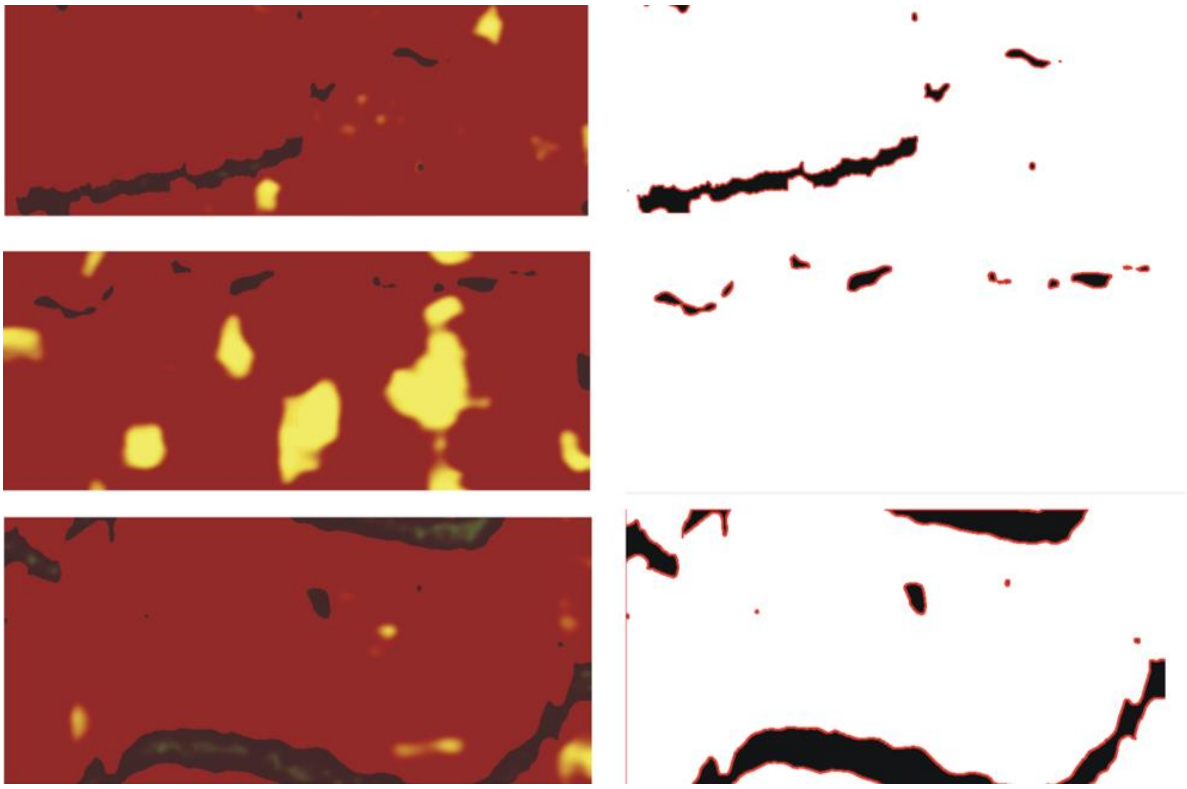

Figure 4-4 Detection of artifacts in the NIRS images on the left - original NIRS images, on the right - marked artifacts' areas (Modyfied from [107]).

4.3. Detection of lipid pool

The detection of lipid regions consists of two steps including, segmentation of visible regions, and those lying under the artifacts. For the detection of clearly visible regions, Otsu algorithm was applied. The outcome of this step can be seen in figure 4.3-1. The detection of lipid regions hidden under artifacts was performed by the analysis of the intensity changes in these regions. Firstly, a histogram for the segmented regions was computed. The highest peak informed about the intensity of the analyzed region (background of the artifact region). Secondly, based on the value of the background the whole region was investigated for intensity changes. If the difference between the background intensity was higher than the experimental threshold, the region is marked as a lipid area (Figure 4-4).

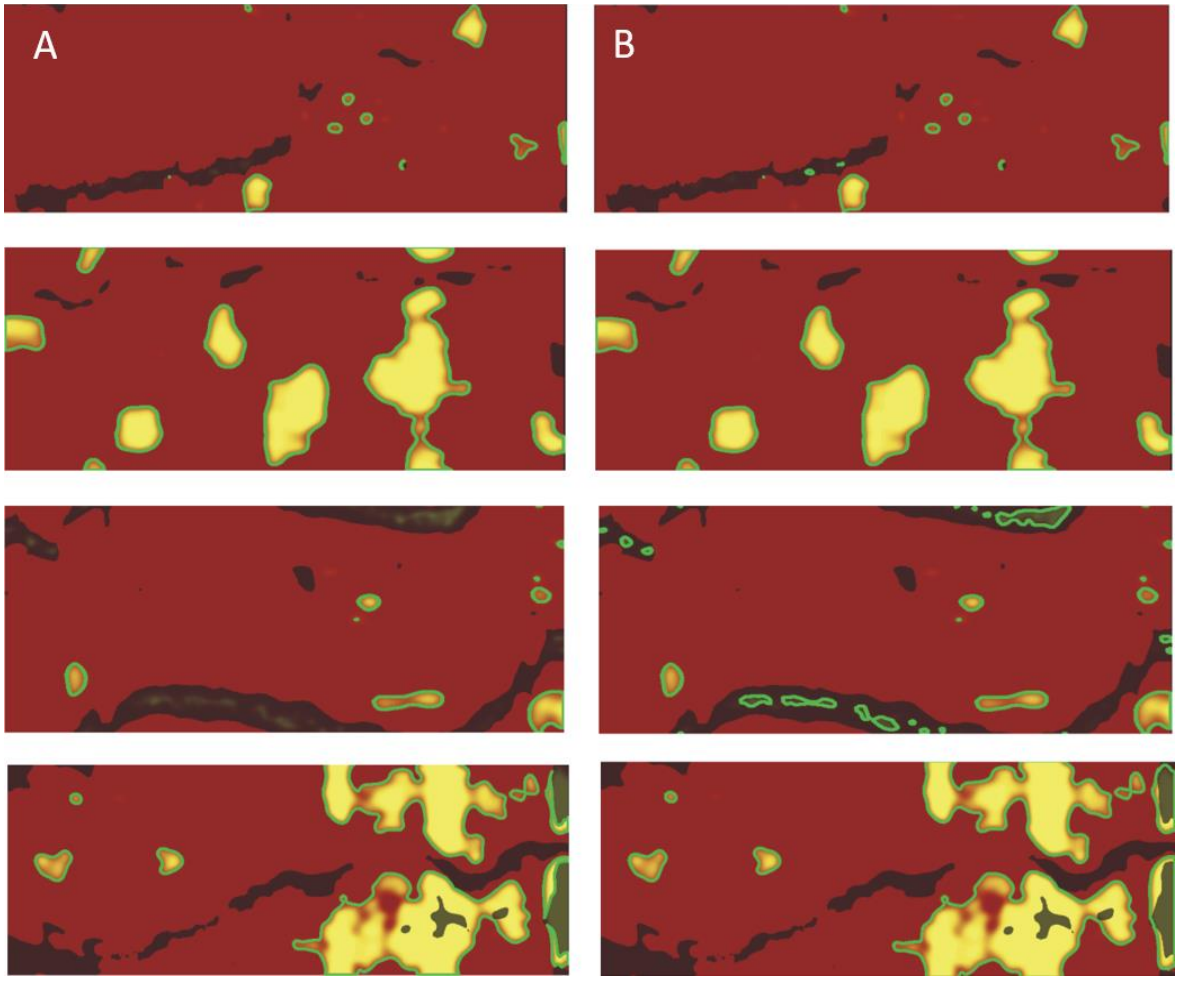

Figure 4-5 Figure 4-6 Segmentation of the lipid core plaque areas: a) detection of the visible regions, b) detection of lipid regions covered with artifacts (Modyfied from [107]).

Calculation of medically important features

From the clinical point of view, the most important parts of the chemogram are those that lie in the stented segment. During the automatic analysis of the NIRS image, the physician can determine the region of interest. LCBI (Lipid Core Burden Index) is helpful in assessing the risk of plaque rupture and the use of preventative strategies during PCI (Percutaneous Coronary Intervention) . Plaque with large LCP (Lipid Core Plaque) and identified by NIRS maxLCBI4mm of ≥ 500 suggested high risk plaque [67, 111, 112].

Within the region, following parameters were calculated:

- LCBI total: Pixels assigned to the lipid plaque regions were divided by all viable pixels to generate the lipid core burden index:

$$LCBI_{total} = \frac{Area(Lipid\ Core\ Plaque)}{Area\ (Stented/Selected)} * 1000 \qquad (4\text{-}1)$$

- $maxLCBI_{2mm}$: is the maximal LCBI in any 2mm-long segment.
- $maxLCBI_{4mm}$: is the maximal LCBI in any 4mm-long segment.

4.4. Results and statistics

Validation

In order to validate the proposed method, the two methods: Method 1 – commercially available system CAAS IntraVascular 2.0 (Pie Medical Imaging), and Method 2 – our algorithm were compared. The collection of 31 chemograms were analyzed in terms of lipid pool detection and automated calculations of LCBI total (maximum LCBI in 4mm blocks and maximum LCBI in 2 mm blocks) in stented segments.

The obtained results were collected in Table 4-1. For all measured parameters - total LCBI, $maxLCBI_{2mm}$, $maxLCBI_{4mm,}$ the ICC was very close to value 1. Showing that the parameters calculated by the developed method (Method 2) are similar to results obtained from the commercially available system (Method 1). Also the Bland-Altman plots (Figure 4-7 Figure 4-8 Figure 4-9) indicate a good agreement between used methods. Most points plotted are between the solid line (mean difference) and the dashed line (mean value ± double standard deviation).

Continuous parameters were reported as a median value with the first and the third quartiles (Q1 – 25%, Q3 – 75%). The Wilcoxon signed-rank test (paired Wilcoxon test) were used for comparison between two related parameters. In cases where the *p*-value was greater than 0.05, the test show that there is no reason to treat measurements as significantly different, but it is still not enough to prove that outcomes from our method are similar to the second method. To check if the measurements from both methods are similar the intraclass correlation (ICC) was computed. The higher the ICC the higher the relation between lipid detection methods. Additionally Bland-Altman plots were presented. Analyses were performed in R: language and environment for statistical computing (R Core Team 2014, Vienna, Austria).

Table 4-1 Table 1. Statistical comparison of parameters(Modyfied from [107]).

	Method1	Method2	Difference	Relative difference [%]	Paired Wilcoxon p-value	ICC (95% CI)	ICC p-value
total LCBI	23.00 (9.00 - 97.00)	22.60 (8.40 - 96.50)	0.00 (-0.80 - 1.00)	-0.61 (-6.17 - 2.83)	0.8822	1 (1 – 1)	< 0.0001
maxLCBI$_{4mm}$	95.00 (20.00 - 245.00)	94.20 (23.00 - 242.00)	-1.50 (-16.00 - 1.20)	-1.55 (-16.19 - 2.81)	0.1265	0.97 (0.93– 0.98)	< 0.0001
maxLCBI$_{2mm}$	162.00 (43.00 - 385.00)	163.10 (45.00 - 384.00)	0.00 (-5.00 - 1.20)	-0.28 (-2.46 - 1.62)	0.4645	1 (0.99 – 1)	< 0.0001

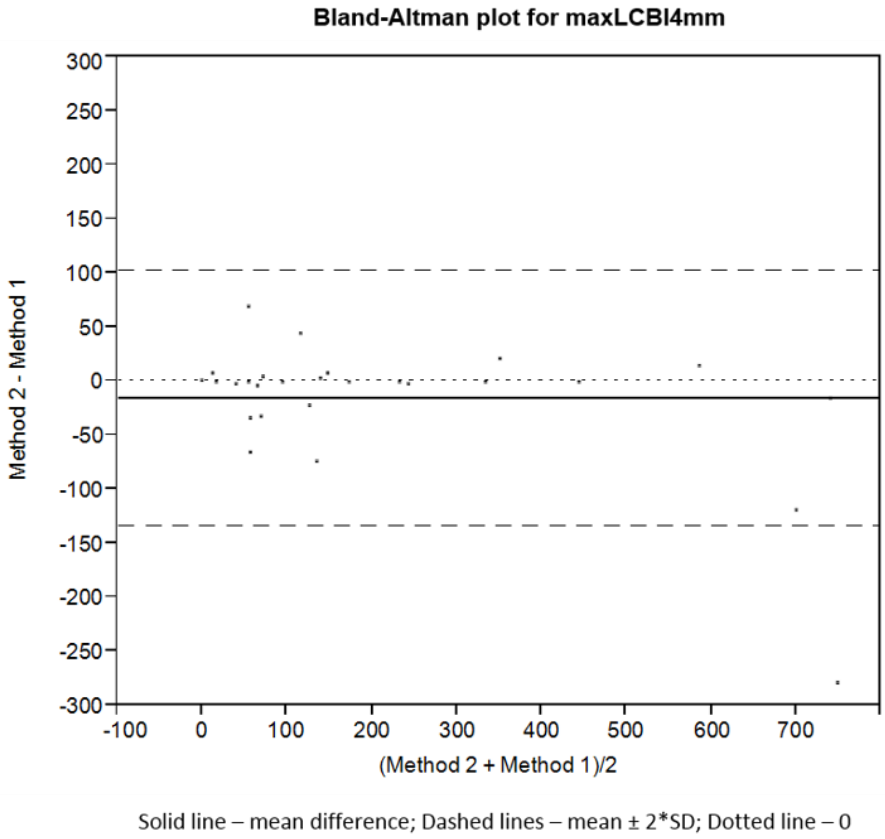

Figure 4-7 Bland-Altman plot for maxLCBI4mmand by two methods (Modyfied from [107]).

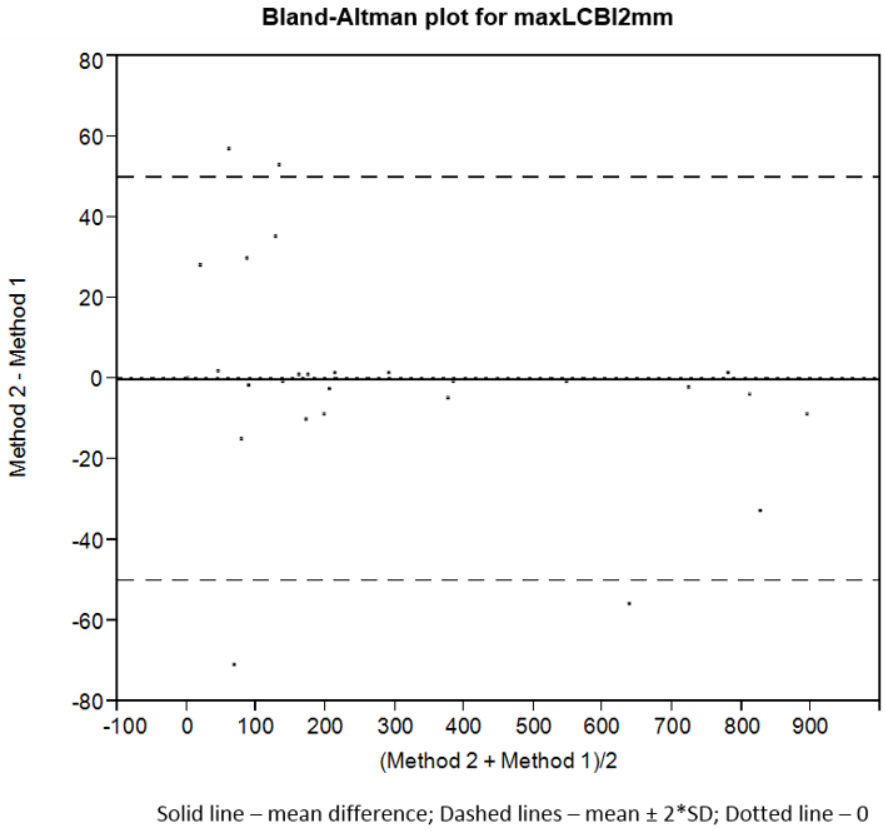

Figure 4-8 Bland-Altman plot maxLCBI2mm calculated by two methods (Modyfied from [107]).

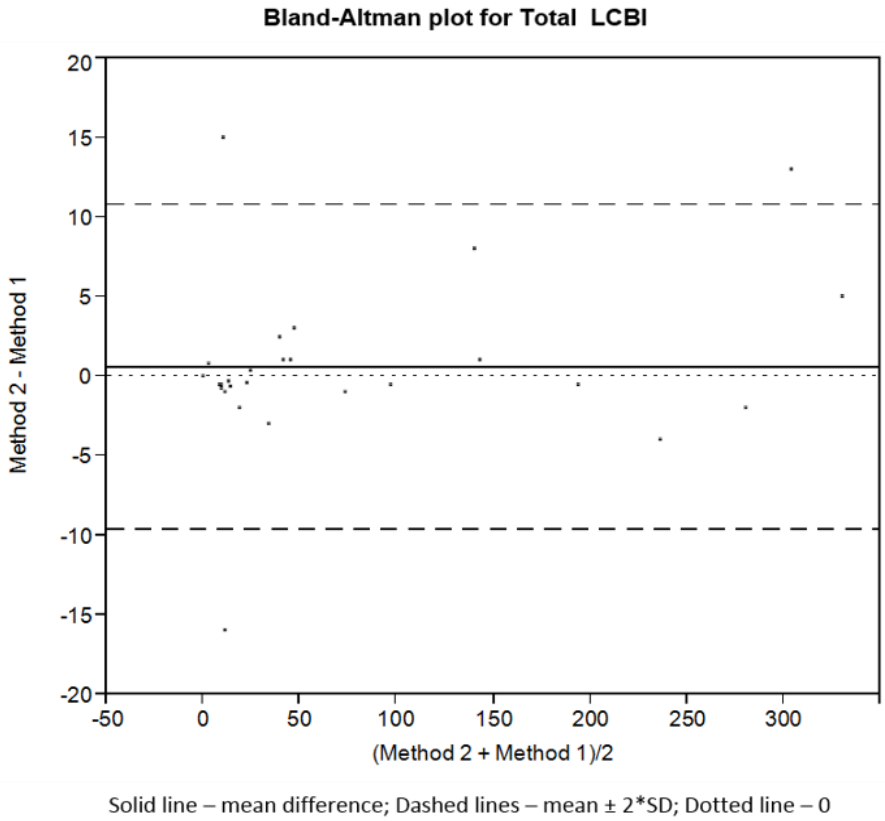

Figure 4-9 Bland-Altman plot for total LCBI, by two methods (Modyfied from [107]).

Summary

A fully automated method, for detecting lipid pools and calculation of LCBI in NIRS images was developed. The method automatically detects the lipid region borders even if they are covered by an overlapping artifact. Moreover, it offers a possibility to calculate the LCBI value in a preselected region, and the maximal value of LCBI in different size of blocks to better match the assessed region with the IVUS data. Additionally, the proposed algorithm provides a tool to automated detection of maximal lipid arc in the assessed block.

Developed algorithms shows a 100% lipid detection accuracy, the results of maximum LCBI values in 4 mm and in 2 mm blocks were different between the proposed method and the unknown method implemented in commercially available system. Taking into account the *p*- value calculated by the Wilcoxon signed-rank test, results are insignificantly different, but the *p*-value itself is not as high as in case of total LCBI. These discrepancy could be a result of different methods dividing region of interest into specific dimension of block. There are not any publications about algorithms used in commercially systems to compare scheme of this procedure.

5. Summarize

5.1. Proof of thesis

The aim of the doctoral dissertation was to prove the thesis presented in Chapter 1:

Using the developed image processing algorithms, enables to computer-assisted quantitative and qualitative evaluation of arteries' lumen and lipid plaque by different Intracoronary Imaging Methods, aiding experts in detection and interpretation of atherosclerosis patterns and cardiac diagnostics.

In order to demonstrate the thesis, complete algorithms for the automated lumen detection on OCT images and for the automated lipid pool detection on NIRS images were designed, implemented, and verified with particular consideration of the vulnerable plaque detection. Distinct research tasks presented in Chapters 2- 4 were carried out to achieve the goal. In the initial phase of the research, it was necessary to review the literature related to the subject of the project and the diagnostic methods, which yields the content of Chapters 2.1 – 2.4. A more detailed analysis of the state of knowledge and literature review are included in Chapter 2.5. Then we developed our own methodology for the processing of both the OCT and the NIRS images, presented in Chapter 3 and in Chapter 4 respectively. The obtained results were elaborated and discussed, and the final effectiveness of each application was found satisfactory.

Recently a novel intravascular imaging modality has been introduced, which makes us closer to receive the universal imaging tool [67, 109, 111, 113-115].

With the advent of such a new intravascular imaging modality, there is still a need for new methodologies to evaluate and interpret the acquired data. Such tools are expected to help in the real time data acquisition and assessment, which may only be achieved by their integration with the IT systems of catherization laboratories. In addition, such tools should also help in off-line data analysis and should allow for more demanding analysis. Proposed algoritmhs for OCT and NIRS images meet most of these requirements.

5.2. Original contributions of this work

The most important result of this work is to develop, implement and validate algorithms to detect and analyse of vessel stenosis and lipid core plaque, which allow automatic assessment of atherosclerosis plaques. In the course of analysis and implementation of selected existing image processing algorithms, we performed a lot of modifications to improve their efficiency

and accuracy, to meet the requirements of the studied medical images in different modalities. The presented algorithms are focused on simple but very effective solutions which greatly impact on intravascular image interpretation and final medical diagnosis. Developed algorithms achieved competitive results to commercially available systems and could be used in core laboratories for research and diagnostics.

The principal novelty of this study was to use the eye-tracking methods to study the distribution of medically crucial information in the OCT images and identify the most important elements to determine their hierarchy during a visual interpretation by the human. Further, the obtained information was used to formulate processing rules for the algorithms.

6. References

1. Pociask, E., et al., *Fully Automated Lumen Segmentation Method for Intracoronary Optical Coherence Tomography.* J Healthc Eng, 2018. **2018**: p. 1414076.
2. OpenStax. *Heart Anatomy*. Available from: https://opentextbc.ca/anatomyandphysiology/chapter/19-1-heart-anatomy/.
3. Tsantis, S., et al., *Automatic vessel lumen segmentation and stent strut detection in intravascular optical coherence tomography.* Med Phys, 2012. **39**(1): p. 503-13.
4. GUS-Report, *GUS - Raport.* 2016.
5. Szczeklik, A.T., M., *Kardiologia podręcznik oparty na zasadach EBM*. 2009.
6. Edition, T.E., *Anatomy and Physiology*. Vol. 2. Textbook Equity.
7. Lusis, A.J., *Atherosclerosis.* Nature, 2000. **407**(6801): p. 233-41.
8. Virmani, R., et al., *Vulnerable plaque: the pathology of unstable coronary lesions.* J Interv Cardiol, 2002. **15**(6): p. 439-46.
9. Virmani, R., et al., *Pathology of the thin-cap fibroatheroma: a type of vulnerable plaque.* J Interv Cardiol, 2003. **16**(3): p. 267-72.
10. Virmani, R., et al., *Pathology of the vulnerable plaque.* J Am Coll Cardiol, 2006. **47**(8 Suppl): p. C13-8.
11. Schaar, J.A., et al., *Terminology for high-risk and vulnerable coronary artery plaques. Report of a meeting on the vulnerable plaque, June 17 and 18, 2003, Santorini, Greece.* Eur Heart J, 2004. **25**(12): p. 1077-82.
12. Schaar, J.A., et al., *Incidence of high-strain patterns in human coronary arteries: assessment with three-dimensional intravascular palpography and correlation with clinical presentation.* Circulation, 2004. **109**(22): p. 2716-9.
13. Falk, E., P.K. Shah, and V. Fuster, *Coronary plaque disruption.* Circulation, 1995. **92**(3): p. 657-71.
14. Braunwald, E., *Epilogue: what do clinicians expect from imagers?* J Am Coll Cardiol, 2006. **47**(8 Suppl): p. C101-3.
15. Serruys, P.W., et al., *Percutaneous coronary intervention versus coronary-artery bypass grafting for severe coronary artery disease.* N Engl J Med, 2009. **360**(10): p. 961-72.
16. Stroupe, K.T., et al., *Cost-effectiveness of coronary artery bypass grafts versus percutaneous coronary intervention for revascularization of high-risk patients.* Circulation, 2006. **114**(12): p. 1251-7.
17. PCI. Available from: http://www.heartviews.org/viewimage.asp?img=HeartViews_2011_12_4_169_90906_u3.jpg .
18. Waller, B.F., C.A. Pinkerton, and J.D. Slack, *Intravascular ultrasound: a histological study of vessels during life. The new 'gold standard' for vascular imaging.* Circulation, 1992. **85**(6): p. 2305-10.
19. Suh, W.M., et al., *Intravascular detection of the vulnerable plaque.* Circ Cardiovasc Imaging, 2011. **4**(2): p. 169-78.
20. Cheneau, E., et al., *Predictors of subacute stent thrombosis: results of a systematic intravascular ultrasound study.* Circulation, 2003. **108**(1): p. 43-7.
21. Alfonso, F., et al., *Findings of intravascular ultrasound during acute stent thrombosis.* Heart, 2004. **90**(12): p. 1455-9.
22. Fujii, K., et al., *Stent underexpansion and residual reference segment stenosis are related to stent thrombosis after sirolimus-eluting stent implantation: an intravascular ultrasound study.* J Am Coll Cardiol, 2005. **45**(7): p. 995-8.
23. Gutierrez-Chico, J.L., et al., *Delayed coverage in malapposed and side-branch struts with respect to well-apposed struts in drug-eluting stents: in vivo assessment with optical coherence tomography.* Circulation, 2011. **124**(5): p. 612-23.

24. Stone, G.W., et al., *A prospective natural-history study of coronary atherosclerosis.* N Engl J Med, 2011. **364**(3): p. 226-35.
25. Sharif, F. and R.T. Murphy, *Current status of vulnerable plaque detection.* Catheter Cardiovasc Interv, 2010. **75**(1): p. 135-44.
26. Kume, T., et al., *Assessment of coronary arterial thrombus by optical coherence tomography.* Am J Cardiol, 2006. **97**(12): p. 1713-7.
27. Kume, T., et al., *Assessment of coronary arterial plaque by optical coherence tomography.* Am J Cardiol, 2006. **97**(8): p. 1172-5.
28. Prati, F., et al., *Does optical coherence tomography identify arterial healing after stenting? An in vivo comparison with histology, in a rabbit carotid model.* Heart, 2008. **94**(2): p. 217-21.
29. Pociask, E., N. Bruining, and K. Proniewska, *The potential role of intracoronary imaging at the dawn of the fourth revolution in Interventional Cardiology.* Revista Argentina de Cardioangiología Intervencionista, 2016. **7(1)**.
30. A, S., *NIRS-IVUS characterization of plaque structure and composition: Implication for optimal stenting and detection of vulnerable plaque.* The Journal of Invasive Cardiology, 2013. **25**
31. Roger, L.E.J., *Fundamentals of Digital Image Processing*. 2010.
32. Domański, M., *Obraz cyfrowy*. 2010.
33. Pratt, W.K., *Digital Image Processing*. 2001.
34. Gonzalez, R.C.W., R.E.;, *Digital Image Processing 2/E*.
35. Bovik, *Handbook of Image and Video Processing (Communications, Networking and Multimedia)*, ed. N.a.M. Communications. 2005.
36. Jahne, B., *Digital Image Processing*. 5 ed. 1997: Springer-Verlag Berlin Heidelberg.
37. Castleman, *Digital Image Processing*. 1979: Pearson; 1 edition (
38. Gonzalez, R.C.W., R.E.;, *Digital Image Processing 3rd Edition.* 2008.
39. Tadeusiewicz, R. and J. Śmietański, *Acquisition of medical images and their processing, analysis, automatic recognition and diagnostic,*. 2011: Wydawnictwo STN, Kraków.
40. Choraś, R., *Komputerowa Wizja. Metody interpretacji i identyfikacji obiektów*. 2005: Komputerowa Wizja. Metody interpretacji i identyfikacji bestow.
41. J., C., G. J., and G. A., *Cyfrowe przetwarzanie obrazów medycznych. Algorytmy. Technologie. Zastosowania*. 2008: Wydawnictwo EXIT, Warszawa,.
42. Tadeusiewicz, R. and J. Śmietański, *Pozyskiwanie obrazów medycznych oraz ich przetwarzanie, analiza, automatyczne rozpoznawanie i diagnostyczna interpretacja*. 2011: Wydawnictwo STN, Kraków 2011.
43. Mattioli, J., *Minkowski operations and vector spaces.* Set-Valued Analysis,, 1995. **3**.
44. Matheron, G., *Random Sets and Integral Geometry*. 1975: New York: Wiley.
45. Serra, J. and P. Soille, *Mathematical Morphology and Its Applications to Image Processing*. 1994: Springer-Science+Business Media, B.V.
46. Sternberg, S.R., *Grayscale morphology, Computer Vision, Graphics, and Image Processing*

Vol. 35. 1986. 333-355.
47. Tadeusiewicz, R. and P. Krohoda, *Komputerowa analiza i przetwarzanie obrazów*. 1997: Społeczeństwo Globalnej Informacji, Kraków,.
48. Malina, W. and M. Smiatacz, *Rozpoznawanie obrazów*. 2010: Wydawnictwo EXIT, Warszawa.
49. Gonzalez, R.C.W., R.E.; Eddins, S.L., *Digital Image Processing Using MATLAB.* 2004.
50. Infrared. Available from: http://elte.prompt.hu/sites/default/files/tananyagok/InfraredAstronomy/ch01.html.
51. Kanovsky, J., et al., *Optical coherence tomography in interventional cardiology—Research field or future daily routine?* Elsevier, 2012. **54**(3).
52. Pettersen, O., et al., *Reproducibility of optical coherence tomography in vein grafts used for coronary revascularization.* Cardiol J, 2018.
53. Roleder, T., et al., *Optical Coherence Tomography of De Novo Lesions and In-Stent Restenosis in Coronary Saphenous Vein Grafts (OCTOPUS Study).* Circ J, 2016. **80**(8): p. 1804-11.

54. Kubiak, G.M., et al., *Prediction models for different plaque morphology in non-significantly stenosed regions of saphenous vein grafts assessed with optical coherence tomography.* Postepy Kardiol Interwencyjnej, 2018. **14**(4): p. 363-372.
55. Kubiak, G.M., et al., *Saphenous graft atherosclerosis as assessed by optical coherence tomography data for stenotic and non-stenotic lesions from the OCTOPUS registry.* Postepy Kardiol Interwencyjnej, 2018. **14**(2): p. 157-166.
56. Yabushita, H., et al., *Characterization of human atherosclerosis by optical coherence tomography.* Circulation, 2002. **106**(13): p. 1640-5.
57. Prati, F., et al., *Clinical Impact of Suboptimal Stenting and Residual Intrastent Plaque/Thrombus Protrusion in Patients With Acute Coronary Syndrome: The CLI-OPCI ACS Substudy (Centro per la Lotta Contro L'Infarto-Optimization of Percutaneous Coronary Intervention in Acute Coronary Syndrome).* Circ Cardiovasc Interv, 2016. **9**(12).
58. Barlis, P., et al., *The use of intra-coronary optical coherence tomography for the assessment of sirolimus-eluting stent fracture.* Int J Cardiol, 2009. **136**(1): p. e16-20.
59. Prati, F., et al., *Expert review document on methodology, terminology, and clinical applications of optical coherence tomography: physical principles, methodology of image acquisition, and clinical application for assessment of coronary arteries and atherosclerosis.* Eur Heart J, 2010. **31**(4): p. 401-15.
60. Prati, F., et al., *Clinical Impact of OCT Findings During PCI: The CLI-OPCI II Study.* JACC Cardiovasc Imaging, 2015. **8**(11): p. 1297-305.
61. Imola, F., et al., *Safety and feasibility of frequency domain optical coherence tomography to guide decision making in percutaneous coronary intervention.* EuroIntervention, 2010. **6**(5): p. 575-81.
62. Yamaguchi T, T.M., Akasaka T, et al, *Safety and feasibility of an intravascular optical coherence tomography image wire system in the clinical setting.* Am J Cardiol, 2008. **101**: p. 562-567.
63. Stefano, G.T., et al., *Utilization of frequency domain optical coherence tomography and fractional flow reserve to assess intermediate coronary artery stenoses: conciliating anatomic and physiologic information.* Int J Cardiovasc Imaging, 2011. **27**(2): p. 299-308.
64. Sigwart, U., et al., *Intravascular stents to prevent occlusion and restenosis after transluminal angioplasty.* N Engl J Med, 1987. **316**(12): p. 701-6.
65. Zhang, P.F. and Y. Zhang, *[Current status on the progress in detection of arteriosclerotic vulnerable plaque with imaging technic].* Zhonghua Yi Xue Za Zhi, 2004. **84**(13): p. 1140-2.
66. Chan, K.H. and M.K. Ng, *Is there a role for coronary angiography in the early detection of the vulnerable plaque?* Int J Cardiol, 2013. **164**(3): p. 262-6.
67. Roleder, T., et al., *Combined NIRS and IVUS imaging detects vulnerable plaque using a single catheter system: a head-to-head comparison with OCT.* EuroIntervention, 2014. **10**(3): p. 303-11.
68. Cassis, L.A. and R.A. Lodder, *Near-IR imaging of atheromas in living arterial tissue.* Anal Chem, 1993. **65**(9): p. 1247-56.
69. Cheimariotis, G.A., et al., *ARCOCT: Automatic detection of lumen border in intravascular OCT images.* Comput Methods Programs Biomed, 2017. **151**: p. 21-32.
70. Macedo, M.M.T., C. K.; Lemos, P.A.; Gutierrez, M.A., *A robust fully automatic lumen segmentation method for in vivo intracoronary optical coherence tomography.* Research on Biomedical Engineering, 2016. **vol.32 no.1**.
71. Macedo, M.M., et al., *A bifurcation identifier for IV-OCT using orthogonal least squares and supervised machine learning.* Comput Med Imaging Graph, 2015. **46 Pt 2**: p. 237-48.
72. Moraes, M.C., D.A. Cardenas, and S.S. Furuie, *Automatic lumen segmentation in IVOCT images using binary morphological reconstruction.* Biomed Eng Online, 2013. **12**: p. 78.
73. Moraes, M.C. and S.S. Furuie, *Automatic coronary wall segmentation in intravascular ultrasound images using binary morphological reconstruction.* Ultrasound Med Biol, 2011. **37**(9): p. 1486-99.

74. Sihan, K. et al., *A novel approach to quantitative analysis of intravascular optical coherence tomography imaging*, in *35th Annual Computers in Cardiology Conference*. 2008, IEEE: Bologna, Italia.
75. Ughi, G.J., et al., *Fully automatic three-dimensional visualization of intravascular optical coherence tomography images: methods and feasibility in vivo.* Biomed Opt Express, 2012. **3**(12): p. 3291-303.
76. Kim, H.M., et al., *Automatic lumen contour detection in intravascular OCT images using Otsu binarization and intensity curve.* Conf Proc IEEE Eng Med Biol Soc, 2014. **2014**: p. 178-81.
77. Gao, Z., et al., *Automated detection framework of the calcified plaque with acoustic shadowing in IVUS images.* PLoS One, 2014. **9**(11): p. e109997.
78. Sihan, K., et al., *Fully automatic three-dimensional quantitative analysis of intracoronary optical coherence tomography: method and Validation.* Catheter Cardiovasc Interv, 2009. **74**(7): p. 1058-65.
79. Drew, T.V., M.L-H; Olwal, A.; Jacobson, F.;Seltzer, S.E.; Wolfe, J.M. , *Scanners and drillers: Characterizing expert visual search through volumetric images.* Journal of Vision, 2013. **13(10):3**: p. 1-13.
80. Rayner, K., *Eye movements and attention in reading, scene perception, and visual search.* The Quarterly Journal of Experimental Psychology, 2009. **62:8**: p. 1457-1506.
81. Kundel, H.L.L.F., P.S. Jr, *Visual search patterns and experience with radiological images.* Radiology, 1972. **103**: p. 523–528.
82. Kundel, H.L.N., C.F.;Conant, E.F.; Weinstein, S.P., *Holistic component of image perception in mammogram interpretation: gaze-tracking study.* Radiology, 2007. **242**: p. 396–402.
83. Augustyniak, P., *Ocena gęstości informacyjnej elektrokardiogramu metodą eliminacji współczynników falkowych, w materiałach II Sympozjum Modelowanie i Pomiary w Medycynie*. 2000: Krynica Górska. p. 221-230.
84. Augustyniak, P., *How a Human Perceives the Electrocardiogram*, in *Computers in Cardiology*. 2003. p. 601-604.
85. Augustyniak P., M.Z., *Detection of Object Salient Features Based on the Observer Scanpath Analysis*, in *IFMBE Proceedings*. 2005.
86. Augustyniak P., T.R., *Assessment of electrocardiogram visual interpretation strategy based on scanpath analysis*, in *Physiol. Meas.* 2006. p. 597-608.
87. Rao, R., et al., *Eye movement in visual cognition: a computational study.* 1997.
88. Augustyniak , P., *Przetwarzanie sygnałów elektrodiagnostycznych*. 2001, Uczelniane Wydawnictwo Naukowo-Dydaktyczne - AGH: Kraków.
89. E, K., *Current perspectives in medical image perception.* Attention, Perception & Psychophysics, 2010. **72(5)**: p. 1205-1217.
90. Saber-Tehrani AS, L.H., Matthews SC, et al, *20-year summary of US malpractice claims for diagnostic errors from 1985–2005*, in *Proceedings of the fourth Annual Diagnostic Error in Medicine Conference*. 2011.
91. Tearney GJ, R.E., Akasaka T, et al., *Consensus standards for acquisition, measurement, and reporting of intravascular optical coherence tomography studies: a report from the International Working Group for Intravascular Optical Coherence Tomography Standardization and Validation.* J Am Coll Cardiol, 2012. **59**: p. 1058-1072.
92. Ghaffari, S., et al., *The Relationship between Coronary Artery Movement Type andStenosis Severity with Acute Myocardial Infarction.* J Cardiovasc Thorac Res, 2013. **5**(2): p. 41-4.
93. Augustyniak, P. and Z. Mikrut, *Task-Dependent Parameters of Attention Measured by Two Eyetrackers.* Journal of Medical Informatics and Technologies, 2001. **2**: p. 59-66.
94. Augustyniak , P. and Z. Mikrut, *Lokalizacja istotnych cechobrazu metodą śledzenia ścieżki wzrokowej.*, in *XIII Krajowa Konferencja Biocybernetyka i Inżynieria Biomedyczna*. 2003: Gdańsk. p. 931-936.

95. Mikrut, Z. and P. Augustyniak *Estimation of Execution Time for Tasks of Objects Couting and Localization Using the Ober2 Device.*, in *IFMBE - 12th Nordic-Baltic Conference Engineering and Medical Physics*. 2002: Reykjavik. p. 394-395.
96. Tadeusiewicz, R. and P. Augustyniak *Analysis of human eye movements during the plot inspection as a tool of assessment of local informative value of the 12-lead ECG.* Biocybernetics and Biomedical Engineering, 2007. **27**: p. 169-176.
97. Pociask, E., *Badanie topologii rozkłądu informacji diagnostycznej na obrazie OCT*, in *Metody pozyskiwania i przykłady wykorzystania sygnału okoruchowego*. 2016, Akademicka Oficyna Wydawnicza EXIT: Warszawa. p. 100-107.
98. Pociask, E., *Ocena doświadczenia analityka obrazów medycznych*, in *Metody pozyskiwania i przykłady wykorzystania sygnału okoruchowego*. 2016, Akademicka Oficyna Wydawnicza EXIT: Warszawa. p. 122-126.
99. Pociask, E., et al., *Image Analysts, Eye Movement Patterns During Intravascular OCT Interpretation*, in *The 20th Polish Conference on Biocybernetics and Biomedical Engineering,*. 2017, Springer: Kraków.
100. Durlak, D., *Analysis of the impact of advertising on human attention during various activities*. 2014, AGH.
101. Augustyniak , P. and Z. Mikrut, *Complete Scanpaths Analysis Toolbox*, in *the 28th IEEE EMBS Annual International Conference* 2006: New York City, USA. p. 5137-5140.
102. Arias-Castro, E.D., D.L., *Does median filtering truly preserve edges better than linear filtering?* The Annals of Statistics, 2009. **37, No. 3, 1172-1206**.
103. Sobel, I., *An isotropic 3x3 image gradient operator. Machine Vision for Three-Dimensional Scenes.* 1990.
104. Press, W.H.T., S.A., *Savitzky-Golay Smoothing Filters.* Computer in Physics 1990. **4**(6).
105. Orfanidis, S.J., *Introduction to Signal Processing*, ed. N.P.-H. Englewood Cliffs. 1996.
106. Giavarina, D., *Understanding Bland Altman analysis.* Biochem Med (Zagreb), 2015. **25**(2): p. 141-51.
107. Pociask, E., et al., *Fully Automated Lipid Pool Detection Using Near Infrared Spectroscopy.* Comput Math Methods Med, 2016. **2016**: p. 1487859.
108. Pu, J., et al., *In vivo characterization of coronary plaques: novel findings from comparing greyscale and virtual histology intravascular ultrasound and near-infrared spectroscopy.* Eur Heart J, 2012. **33**(3): p. 372-83.
109. Gardner, C.M., et al., *Detection of lipid core coronary plaques in autopsy specimens with a novel catheter-based near-infrared spectroscopy system.* JACC Cardiovasc Imaging, 2008. **1**(5): p. 638-48.
110. Otsu, N., *A Threshold Selection Method from Gray-Level Histograms*, M. IEEE Trans. Sys., Cyber. , Editor. 1979. p. 62–66.
111. Goldstein, J.A., et al., *Detection of lipid-core plaques by intracoronary near-infrared spectroscopy identifies high risk of periprocedural myocardial infarction.* Circ Cardiovasc Interv, 2011. **4**(5): p. 429-37.
112. Brugaletta S, G.-G.H., Serruys PW, *Perspective on the Use of True Vessel Characterization Imaging in Interventional Cardiology Clinical Practice.* Interventional Cardiology, 2012. **7(1)**: p. 17-20.
113. Madder, R.D., et al., *Detection by near-infrared spectroscopy of large lipid core plaques at culprit sites in patients with acute ST-segment elevation myocardial infarction.* JACC Cardiovasc Interv, 2013. **6**(8): p. 838-46.
114. Kang, S.J., et al., *Combined IVUS and NIRS detection of fibroatheromas: histopathological validation in human coronary arteries.* JACC Cardiovasc Imaging, 2015. **8**(2): p. 184-94.
115. Kilic, I.D., et al., *Near-infrared spectroscopy-intravascular ultrasound: scientific basis and clinical applications.* Eur Heart J Cardiovasc Imaging, 2015. **16**(12): p. 1299-306.

Tables

Figures